The Effect of Cortical and Pallidal Inputs on Striatal Microcircuit Activity and Behavioral Output

by

Victoria Louise Corbit

Bachelor's of Science, Lafayette College, 2013

Submitted to the Graduate Faculty of

School of Medicine in partial fulfillment

of the requirements for the degree of

Doctor of Philosophy

University of Pittsburgh

2019

UNIVERSITY OF PITTSBURGH

SCHOOL OF MEDICINE

This dissertation was presented
by

Victoria Louise Corbit

It was defended on

June 17, 2019

and approved by

Robert S. Turner, Ph.D, Professor, Department of Neurobiology

Susan R. Sesack, Ph.D, Professor, Department of Neuroscience

Peter L. Strick, Ph.D, Distinguished Professor and Chair, Department of Neurobiology

Patrick Rothwell, Ph.D, Assistant Professor, Department of Neuroscience, University of Minnesota

Dissertation Director: Susanne E. Ahmari, M.D., Ph.D, Assistant Professor, Department of Psychiatry

Dissertation Director: Aryn H. Gittis, Ph.D, Associate Professor, Department of Biological Sciences, Carnegie Mellon University

The Effect of Cortical and Pallidal Inputs on Striatal Microcircuit Activity and Behavioral Output

Victoria Louise Corbit, PhD

University of Pittsburgh, 2019

This dissertation focuses on the role of striatal microcircuits and how afferents from cortex and globus pallidus externa (GPe) play a role in striatal activity and behavioral output. In the first chapter I summarize the role of striatal subregions in behavioral selection and initiation and elaborate on how striatal activity in output neurons (SPNs) and fast-spiking interneurons (FSIs) has been associated with behavioral initiations.

Chapter 2 highlights the capacity of an FSI-specific pallidostriatal projection for controlling the activity of SPNs, particularly under dopamine depletion conditions. These data suggest that GPe may provide bursts of inhibition to FSIs, allowing SPNs a disinhibition window of time in which to fire without strong regulation from FSIs.

In Chapter 3 I investigate abnormalities in cortical input to central striatum (CS) of *Sapap3*-KO mice. I demonstrate that LOFC inputs to CS are reduced onto SPNs in *Sapap3*-KOs. In contrast, M2 inputs, which are weak in WTs, are strengthened in KOs. These data suggest a potential increase in motor control over CS in KOs, possibly contributing to the repetitive behavior observed in these mice.

Chapter 4 presents work investigating the role of the M2-CS circuit in grooming behavior. I first describe data from the lab showing that CS is hyperactive at the start of a grooming bout in *Sapap3*-KOs. I then show that there is grooming-related activity in both M2 and terminals in CS, but that this activity doesn't differ by genotype; this suggests that *ex vivo* post-synaptic strengthening may lead to a post-synaptic potentiation of M2 signals in CS. I then demonstrate the

sufficiency of this circuit in grooming behavior by stimulating CS or M2 terminals in CS and showing evoked grooming behavior.

In the final chapter I discuss what my data may suggest about the role of corticostriatal circuits in behavioral initiations. Based on data that cortical terminal stimulation doesn't cause immediate evoked behavior but CS stimulation does, I propose that the site of grooming initiation signals is in striatum. I describe a model in which CS integrates inputs from cortex and GPe to overcome hyperpolarized membrane potentials and generate activity to initiate grooming.

Table of Contents

List of Tables

List of Figures

Preface

In publishing this dissertation I would like to acknowledge the countless mentors, labmates, friends, and family members who supported me throughout this process. There are too many to name everyone, but I specifically want to highlight the training by my co-mentors, Dr. Susanne Ahmari and Dr. Aryn Gittis. These two inspiring scientists taught me how to think about science, and, importantly, how to communicate science. As additional mentors and members of my committee who have trained and guided me in various ways, I want to thank Dr. Rob Turner, Dr. Peter Strick, Dr. Susan Sesack, Dr. Jon Rubin, Dr. Jill Glausier, and my dissertation outside examiner, Dr. Patrick Rothwell. I hope to continue these relationships throughout my career.

I want to thank labmates and friends, Dr. Kevin Mastro, Dr. Sean Piantadosi, and Dr. Jesse Wood. As the people that I talked to, laughed with, and did science with every day, these three supported me endlessly, and I have learned so much about being a scientist from each of them. Other lab members of the Ahmari Lab and Gittis Labs frequently helped me be in two places at once, and for that I am very grateful.

Lastly I want to acknowledge my family. While they don't always fully understand what I did daily or long-term, they, especially my dad, Charles Corbit, and my mom, Kim Miller, were unconditionally supportive, loving, and excited for me. And to my rock, my husband, Ryan Rathman, who saw me through celebrations and disappointments, I am forever grateful to have you in my life and with me as I journey through my career in science.

1.0 Introduction

Behavioral selection broadly involves understanding the context and potential outcome of different behavioral responses, selecting a behavioral response, and initiating that action. Striatal circuits have long been broadly implicated in behavioral selection and initiation at both the macrocircuitry and microcircuitry levels. Following a sensorimotor-motivational topography, different striatal subregions subserve different aspects and types of behavior. Concordantly, a closer look at the specific cell types and synapses involved in these processes reveals that striatal microcircuits are key regulators of behavioral output. While a substantial amount of work has been done looking at behavioral selection and initiation in healthy conditions, we have also learned about these processes stems from studying disease conditions. In the following sections I will summarize striatal involvement in behavioral selection and initiation at the level of striatal subregions and microcircuitry, and discuss how striatal activity and behavioral output can become abnormal in disease states of akinesia and compulsivity.

1.1 Distinct Regions of Striatum Mediate Different Aspects of Behavioral Selection

The striatum is a large subcortical structure that receives a diverse set of inputs. Excitatory drive is mediated by a wide range of cortical and thalamic inputs, and dopaminergic modulation is provided by a strong projection from ventral tegmental area (VTA)/substantia nigra pars compacta (SNc) (Björklund and Dunnett, 2007). The striatum is known to have distinct territories that mediate different types and aspects of behavior across species, such as decision making,

movement initiation, and reward prediction (Balleine et al., 2007). While it is likely that all regions of striatum play some role in all behaviors, distinct regions have been clearly associated with certain functions.

The striatum is known to have a general motor-limbic topography that, in rodents, extends from dorsolateral striatum (sensorimotor), to central/dorsomedial (associative), and down to ventral striatum (limbic/motivational) (McGeorge and Faull, 1989; Voorn et al., 2004). Anatomical studies suggest a similar motor-limbic topography in the primate striatum, and microstimulation studies demonstrate an even more fine grain somatotopic map in the motor regions of striatum (Alexander and DeLong, 1985; Haber et al., 2006; Kunishio and Haber, 1994; Lynd-Balta and Haber, 1994). More recent anatomical and functional data provides support that these topographies are also present in humans (Marquand et al., 2017; Wiesendanger et al., 2004). These findings suggest that the investigations into striatal topography and function in rodents likely has parallels to relevant phenomena in humans and non-human primates. For the purpose of this dissertation, the following sections will focus on the large body of research in rodents investigating the relationship between spatial territories of striatal function and goal-directed and habitual behavior selection.

1.1.1 Dorsolateral Striatum Mediates Stimulus-Response Behavior

Dorsolateral striatum (DLS) is thought to be the sensorimotor region of striatum. It receives its main cortical input from primary motor cortex and sensory cortices, and cells in DLS show responses to sensorimotor activation of individual body parts (Coffey et al., 2016). Furthermore, in primates, in vivo recordings and microstimulation of lateral striatum shows a somatotopic map

of distinct body parts (Alexander and DeLong, 1985). Functionally, DLS is known to mediate stimulus-response relationships, as evidenced by its involvement in well-trained and habitual behaviors (Ashby et al., 2010; Yin et al., 2004). It has been demonstrated that lesions of DLS prevent the expression of habitual stimulus-response behaviors, which are defined by resistance to outcome devaluation (Gremel and Costa, 2013b; Yin et al., 2004, 2006). In contrast, disengagement of DLS during the beginning stages of operant discrimination learning actually improves learning (Bergstrom et al., 2018), emphasizing the role of DLS in late learning, such as habit learning or skill mastery. To further assess the role of DLS activity in learning, Thorn and colleagues trained rats on a T-maze task that required not only skilled motor performance as usual, but also required flexible responding as sensory cues changed throughout different stages of training (Thorn et al., 2010). In vivo recordings showed that, once an animal is well trained on one version of the task, activity in DLS is highly responsive to that task but not the alternative cue version of the same task (Thorn et al., 2010). This supports the idea of DLS being important for overtraining or late learning of a task. Furthermore, ex vivo physiology in mice that have learned a skilled motor task has shown that corticostriatal post-synaptic responses in DLS are stronger at the late-learning phases relative to early learning stages (Yin et al., 2009). More recent work has demonstrated that motor cortical inputs to DLS disengage by the time a motor skill is mastered (Kupferschmidt et al., 2017), together suggesting a possible transfer of relevant behavioral information from presynaptic motor cortex input to DLS post-synaptically.

In addition to its role in habitual behaviors, DLS is associated with both trained and naturalistic sequences of behaviors. DLS activity is associated with task-bracketing the beginning and end of a sequence of well-trained behaviors (Jin et al., 2014; Thorn et al., 2010), suggesting that trained sequences are encoded here as single actions. Grooming is a naturalistic sequenced

behavior in rodents, which also appear to involve DLS; lesions to DLS reduce the amount of full grooming chains, while not affecting the performance of individual grooming movements (Cromwell and Berridge, 1996). Additionally, activity related to grooming sequences, but not individual grooming movements, has been found in 41% of DLS cells (Aldridge and Berridge, 1998; Aldridge et al., 1993).

Taken together, these data suggest that DLS is important for the automatic sequencing of behaviors that are very well engrained behaviorally. It seems that once a sequence of behaviors is so well-trained that it becomes an automatic response to a given stimulus or context, the DLS is important for performing that response.

1.1.2 Dorsomedial Striatum is Important for Goal-Directed Behavior

The initial training portion of a given behavioral task or sequence of tasks appears to primarily involve the dorsomedial striatum (DMS). The DMS is thought to be a cognitive or associative region of striatum, and receives cortical inputs from areas such as anterior cingulate cortex (Oh et al., 2014). DMS activity has been associated with goal-directed behaviors and early-stages of training (Thorn et al., 2010; Yin et al., 2009; Yin et al., 2005). For example, DMS is most task-responsive when a task has been learned but is not overtrained, whereas activity in DMS disengages when the task becomes overtrained (Kupferschmidt et al., 2017; Thorn et al., 2010). Consistent with this, in contrast to DLS, lesions of DMS impact the expression of goal-directed behavior by causing a shift towards habitual responding that renders rodents insensitive to reward devaluation or contingency degradation (Yin et al., 2005). This role in flexible responding is supported by primate work showing that inactivation of medial striatum leads to perseverative responding on a reversed contingency (Clarke et al., 2008). Furthermore, lesion and *in vivo*

electrophysiological studies in rodents show that DMS plays an important role both in encoding both spatial working memory before a lever press leading to reward and stimulus-response associations, again emphasizing its role in goal-directed behavior (Akhlaghpour et al., 2016). Finally, optogenetic manipulations of opposing cell types in DMS have been able to elicit movement or immobility (Kravitz et al., 2010), and can reinforce particular behaviors (Yttri and Dudman, 2016), suggesting that DMS plays a role in the decision of whether or not to enact a behavior

Consistent with its involvement in the volitional control of behavior based on known outcomes, DMS is thought to be less important for the expression of automatic sequences of behavior. This is supported by the fact that lesions to DMS do not significantly affect grooming sequences or individual grooming behaviors (Cromwell and Berridge, 1996), and activity in DMS and its cortical inputs is relatively low during the performance of a skilled behavior (Kupferschmidt et al., 2017; Thorn et al., 2010).

1.1.3 Ventral Striatum Processes Reward

The ventral striatum (VS) is thought to be even more important then DMS for encoding the reinforcement of behaviors. VS receives excitatory input from prefrontal cortical regions, amygdala, hippocampus, and a strong dopaminergic projection from VTA (Humphries and Prescott, 2010). Because of this convergence of inputs, it is thought to integrate diverse types of information about the rewarding value of a behavior. While stimulation of cortical inputs to this region can lead to movement effects (e.g. hyperactivity) (Ahmari et al., 2013), the primary role of VS is thought to be reward processing. Indeed, VS cells in primates are responsive to reward presence and modulated by reward magnitude (Schultz et al., 1992), and though both dorsal and

ventral striatum show responses to reward in humans, twice as many cells in VS show reward representations relative to dorsal striatum (Delgado, 2007).

The involvement of VS in behavioral sequences is also likely dependent on a known rewarded outcome following a particular action sequence. For example, lesions to VS do not disrupt the performance of naturalistic grooming sequences (Cromwell and Berridge, 1996). In rodents, VS lesions affect performance of a delayed discounting task (Cardinal et al., 2001). This could suggest problems appropriately assigning value to stimuli if there is a delay before the reward delivery. In contrast, this finding may suggest a role for VS in regulating impulsivity, or the ability to withhold a motor response. This is supporting by evidence suggesting interneuron activity in VS is important for withholding motor responses (Pisansky et al., 2019), potentially suggesting a role for VS in regulating motor activity mediated by more motor-related regions of striatum, similar to ideas proposed by Haber and colleagues (Haber et al., 2000).

A need for a learned reward after a sequence to engage VS involvement in sequences of behavior is in line with the VTA's role in reward prediction error and reinforcement (Schultz et al., 1997). Depleting dopamine from the VS has been shown to prevent the performance of learned sequences (Aberman and Salamone, 1999). Furthermore, VTA neurons have been shown to have activity related to the number of actions in a sequence (Wood et al., 2017), which is either conveyed to or from VS (Takahashi et al., 2016). Taken together, these data suggest that the primary role of circuits in VS in behavioral selection is to integrate information about the reward following a behavior.

1.1.4 Central Striatum May Play a Role in Compulsive Behavioral Selection

The central region of striatum (CS) is relatively understudied. It lies in the middle of the motor-limbic topography (Haber et al., 2000) and receives inputs from lateral orbitofrontal cortex (LOFC) and motor regions (Oh et al., 2014). Its location and inputs suggests it may be important for integrating motor and cognitive factors to affect behavioral selection. Pharmacological studies in rodents have shown that disinhibition of CS causes tic-like behaviors (Bronfeld et al., 2013; Pogorelov et al., 2015). Furthermore, it has been shown that the CS is hyperactive at baseline in vivo in the *Sapap3*-KO mouse model which displays compulsive grooming behavior (Burguiere et al., 2013). Optogenetic stimulation of the LOFC inputs to CS reduces both compulsive grooming and this hyperactivity (Burguiere et al., 2013). In contrast, inhibition of LOFC inputs to CS is necessary for the expression of habit behavior (Gremel et al., 2016), suggesting that reduced activity in this circuit may promote increased automatic behaviors. Thus, while there is limited existing data investigating CS, it appears to be involved with the production of automatic, perhaps unintentional, behaviors. Its role in learned sequences of behavior is yet to be determined.

1.2 Striatal Microcircuits In Behavioral Selection And Initiation

The described motor-limbic topography in the striatum is determined largely on the basis of cortical inputs and thought to extend to downstream basal ganglia structures (Alexander et al., 1986). These loops are largely segregated (Alexander et al., 1986) but have recently been shown to have some degree of overlap between territories (Haber, 2003). Activity in these cortical inputs,

and even in canonically downstream basal ganglia regions, plays a large role in shaping striatal microcircuit activity.

1.2.1 Cortical Inputs are a Prominent Driver of Striatal Activity

Striatal spiny projection neurons (SPNs) are the predominant neuron type in the striatum, making up over 90% of the neurons (Gerfen, 1988). SPNs rest at a very hyperpolarized membrane potential and require significant excitatory input to fire action potentials (Gertler et al., 2008; Jiang and North, 1991). This suggests that the prominent drivers of SPN activity may be excitatory cortical inputs. In support of this idea, it has been shown that SPNs discharge with the upstate of slow-wave cortical activity (Mallet et al., 2005). SPNs themselves also exhibit up-states and down-states in excitability, which occur synchronously in vivo between pairs of recorded SPNs (Stern et al., 1998). The synchronous nature of these depolarized states suggests a common input is driving them. Again suggesting a cortical influence, glutamate uncaging at distal dendritic spines, where cortical inputs are known to synapse (Gerfen, 1988), is sufficient to cause SPN up-states (Plotkin et al., 2011). More recent studies show clearly that stimulation of cortical inputs to striatum can drive activity in striatal cells in vivo(Ahmari et al., 2013; Burguiere et al., 2013; Friedman et al., 2015).

1.2.2 Fast-Spiking Interneurons are Positioned to Apply Cortical Feed-Forward Inhibition onto SPNs

Fast-spiking interneurons (FSIs) receive even stronger cortical activation than SPNs. They are more sensitive to cortical input than SPNs (Mallet et al., 2005; Owen et al., 2018; Parthasarathy

and Graybiel, 1997; Ramanathan et al., 2002), and they are monosynaptically responsive to cortical stimulation in the anesthetized state (Mallet et al., 2005). Furthermore, FSIs exhibit strong, fast inhibitory synapses onto the soma of SPNs (Gittis et al., 2010). Taken together, these data suggest that FSIs mediate cortical feed-forward inhibitory regulation onto SPNs. However, some evidence paradoxically shows that, in awake-behaving animals *in vivo*, FSI activation does not correlate with inhibition of SPNs (Bakhurin et al., 2016; Gage et al., 2010). More recent evidence has shown that both activation and inhibition of striatal FSIs can reduce SPN firing *in vivo* (Lee et al., 2017), though this finding was unable to be replicated by another group (Owen et al., 2018). These seemingly disparate findings may be reconciled by recent work showing that FSI activation *in vivo* is correlated with activity decreases in some populations of SPNs, and increases in other SPN populations (Gritton et al., 2019; O'Hare et al., 2017). Thus, FSIs appear to have the capacity for strong feed-forward inhibition onto SPNs, but the specific microcircuitry and *in vivo* context may be critical for predicting the relationship of FSI activity and the activity of nearby SPNs.

1.2.3 Striatal Interactions Within Basal Ganglia

Both SPNs and FSIs have interactions with downstream structures in the basal ganglia. SPNs, which release GABA, can be divided into two major classes based on the downstream cells onto which they synapse. “Direct pathway” SPNs (dSPNs) express the D1 receptor and project directly to the basal ganglia output nuclei, the substantia nigra pars reticulate (SNr) and globus pallidus interna (GPi) (Gerfen and Young III, 1988). Theoretically, activity in dSPNs will inhibit GABAergic SNr/GPi cells, which project to downstream regions in the thalamus and motor brainstem (Deniau and Chevalier, 1985). Thus, dSPN activation ultimately leads to “activation”

of thalamocortical interactions and of regions that can directly affect motor output. In this way, this pathway is historically thought of as the "go" pathway. Indeed, while optogenetic stimulation of dSPNs showed heterogeneous responses in SNr, activations that elicited movement were associated with a high degree of SNr inhibition (Freeze et al., 2013). These data highlight that dSPN activation can cause movement-permitting inhibition in the SNr, although the effect of dSPN activation on SNr activity is more complicated than previously thought.

In contrast, "indirect pathway" SPNs (iSPNs) express the D2 receptor and first project to the globus pallidus externa (GPe) (Gerfen and Young III, 1988). The GPe then inhibits a glutamatergic structure, subthalamic nucleus (STN), which projects downstream to SNr/GPi. Because of the additional inhibitory step in the pathway, activation of iSPNs thus leads to disinhibition of basal ganglia output nuclei and a resulting inhibition of thalamocortical interactions and motor output regions. For this reason, the indirect pathway has been colloquially termed the "no-go pathway".

The indirect pathway is particularly interesting in the context of the work presented in this thesis because of its non-canonical interactions with striatal FSIs. Specifically, GPe has been shown to send an inhibitory back-projection up to striatal FSIs (Bevan et al., 1998). This suggests that, in addition to cortical input, GPe may play a role in shaping FSI activity and therefore in shaping FSI regulation of SPNs. Indeed, it has been proposed that the precise timing of SPN action potentials in the depolarized up-state are due to inhibitory inputs (Stern et al., 1998) and may be mediated by disinhibition via the GPe-FSI pathway (Wilson, 2009). Given that FSIs inhibit both dSPNs and iSPNs, this suggests that the indirect pathway may have a feedback influence over striatal activity, which emphasizes the importance of thinking about these pathways as interactive rather than separate.

It is tempting to split striatal output into the go and no-go pathways. Indeed, optogenetic stimulation of either dSPNs or iSPNs causes movement and immobility (Kravitz et al., 2010) or reinforcement and punishment (Kravitz et al., 2012), respectively. However, more recent evidence shows that both pathways are active concurrently at movement initiation (Cui et al., 2013; Meng et al., 2018). Furthermore, inhibition or stimulation of dSPNs or iSPNs both cause slowed approach to a lever in a sequence task (Tecuapetla et al., 2016). This suggests that activity in both pathways is essential for movement, although it is also likely that balanced activity in dSPNs and iSPNs is necessary for smooth, natural movements. For this thesis work, the focus will be on the roles of general SPN and FSI ensembles rather than parsing effects based on direct or indirect pathway cell-types.

1.2.4 Striatal Cells Play a Role in Several Aspects of Behavioral Selection and Initiation

Striatal SPNs and FSIs have both been implicated in various aspects of behavioral selection. As briefly described earlier, many SPNs are active before or during the beginning of a movement (Apicella et al., 1991; Cui et al., 2013; Montgomery Jr and Buchholz, 1991; Tecuapetla et al., 2016). In addition, FSIs have been found to be active prior to a movement (Gritton et al., 2019; Marche and Apicella, 2016). These data suggest that striatal cells may be important for movement preparation and initiation. Furthermore, similar to findings with optogenetic stimulation of SPNs, optogenetic stimulation of FSIs when a mouse is at rest can trigger a movement bout (Gritton et al., 2019). These data support a model in which activity in SPNs and/or FSIs is sufficient for movement bouts.

Once a movement is initiated, animals typically perform a sequence of movements, either learned or spontaneous. It has been shown that once an animal learns a sequence of movements,

SPNs tend to show activity at the beginning and end of the sequence (Smith and Graybiel, 2013). Another study showed that a well-learned sequence of movement was encoded by SPNs as a single movement, showing either sustained activation, sustained inhibition, or beginning/end activity for the entire movement sequence (Jin et al., 2014). In contrast to SPN task-bracketing, FSIs tend to be active during the middle of a sequence (Martiros et al., 2018). In addition, ablation of FSIs in the dorsal striatum causes an increase in stress-induced grooming sequences (Xu et al., 2016), suggesting that proper FSI activity may be critical for appropriate initiations and cessations of grooming sequences. These data indicate that both SPNs and FSIs play a role in the appropriate initiations, performance, and cessations of movement sequences.

The final step in a behavioral sequence, particularly those that are learned, is a reward delivery. Again, both SPNs and FSIs have been shown to have activity related to reward or outcome value. SPNs show a representation of action value in primates (Seo et al., 2012) and of reward in mice (Gage et al., 2010), and SPNs and FSIs both show activity that discriminates between reward cues (Bakhurin et al., 2016). More specifically, FSIs, which rarely fire synchronously in striatum (Berke, 2008), have been shown to have a population increase in activity at the choice point in a T-maze task (Gage et al., 2010). Interestingly, this increase in activity is coincident with a decrease in GPe activity (Gage et al., 2010), possibly signaling a role for pauses in GPe activity being important in controlling FSIs. These data suggest that SPNs and FSIs code for reward and/or outcome value, which may play a role in shaping their activity related to movement sequences as well.

1.2.5 SPNs and FSIs Participate in Ensembles

As was suggested earlier, both dSPNs and iSPNs participate in ensemble activity as demonstrated by calcium imaging in vivo and ex vivo (Barbera et al., 2016; Parker et al., 2018). It has been shown that SPNs that are nearby each other are more highly correlated than SPNs far away (Gritton et al., 2019), suggesting that these ensembles are relatively compact in nature. The spatial organization of these ensembles has been shown to correlate to the distance in behavioral space between different types of action, suggesting that these ensembles encode action identity (Klaus et al., 2017).

FSIs also play a strong role in refining striatal ensembles. FSIs are connected via gap junctions and GABAergic chemical synapses (Kita et al., 1990), suggesting that FSIs themselves form ensembles together. However, numerous studies suggest that the primary role of FSIs in striatal ensembles is to refine SPN activity. First, single cell calcium imaging has shown that activity in FSIs is correlated with activity in nearby SPNs (Gritton et al., 2019), indicating that FSIs form ensembles with SPNs in a spatially distinct manner, similarly to SPNs themselves. Supporting a role for FSIs in refining SPN ensemble activity, inhibition of FSIs *in vivo* reduces the task-specificity of SPN activity (Owen et al., 2018). Furthermore, evidence suggests that FSIs play a role in refining SPN ensembles specifically at the beginning of learning; in vivo electrophysiology shows that FSIs modulate SPN task-specificity more during early learning than late learning (Lee et al., 2017). Additionally, ablating FSIs before an animal learns a task prevents the learning process, while ablating them when a task is well-learned has no effect on behavior (Owen et al., 2018).

Thus, it seems that both dSPNs and iSPNs form ensembles with other SPNs nearby, which could be due to shared cortical inputs and/or lateral connections between SPNs (Tunstall et al.,

2002). FSIs (and likely other interneurons not discussed here) also participate in these ensembles (Carrillo-Reid et al., 2008), and existing data suggests that the role of FSIs is to refine striatal ensemble activity, particularly at the beginning of learning a behavior. It is during this stage that ensembles are likely to be in the process of being formed, because an animal is learning to select novel behaviors that lead to reward. It is currently unclear whether/how striatal ensembles play a role in naturalistic behaviors. Presumably, naturalistic behaviors are innate or potentially "learned" very early in life, and therefore already have intact ensemble representations in striatum. The role FSIs may play in these innate ensembles is unclear, though some data suggests that FSI activity may be important for initiating (Gritton et al., 2019) and stopping (Xu et al., 2016) naturalistic movements.

1.3 Disease Abnormalities Can Inform the Understanding of Behavioral Selection and Initiation

We have gained significant insights about striatal activity in behavioral selection from the study of disease models. By investigating striatal processing of behavior in diseases which have abnormal behavioral selection, we can begin to understand how different activity profiles may be critical for normal behavioral selection. For instance, we can study Parkinson's Disease and dopamine depletion, in which behaviors are often unable to be initiated, to understand what striatal activity may be necessary for the initiation of movements. In contrast, pathology that is characterized by unwanted behaviors or movements (Obsessive-Compulsive Disorder, Tourette's Syndrome), or animal models that recreate these phenomenon, can be studied to understand how

abnormalities in striatal processing may lead to the inability to prevent behavioral initiations and/or the inability to stop them.

1.3.1 Parkinson's Disease Includes Reduced Computational Power in Striatal Microcircuits

Parkinson's Disease (PD) is characterized by the loss of dopamine input to the striatum. Behaviorally, dopamine loss manifests in the inability to initiate movements (akinesia) or a slowing of movements (bradykinesia) (Johnston et al., 1999; Panigrahi et al., 2015). One possible neural correlate of these symptoms is the emergence of beta frequency (~8-30Hz) oscillations in cortico-basal ganglia circuitry (Stein and Bar-Gad, 2013; Weinberger et al., 2009). Beta oscillations occur in healthy conditions transiently, but are increased in overall power in PD and dopamine depletion conditions (Stein and Bar-Gad, 2013). Beta activity is thought to promote postural stability or the maintenance of a movement (Brittain et al., 2014). Oscillations and synchrony in general, and beta specifically, are thought to have an inverse-U function with circuit computational power such that levels that are too high or too low limit the computational power of a circuit, while mid-range levels of oscillatory activity facilitate information transfer within circuits (Brittain et al., 2014).

With respect to behavioral selection, these data suggest that beta oscillations serve to promote stability in a movement or a posture, and that excessive beta oscillations, as seen in dopamine depletion, are associated with an inability to initiate new movements (Little and Brown, 2014). The reason that excessive beta causes this problem may lie in its ablation of computational power in cortico-basal ganglia circuits. The GPe is a major site of beta activity, and it shares reciprocal connections with STN that are thought to promote pathological oscillatory activity

(Holgado et al., 2010). However, it has also been shown that beta activity can be induced in striatum given the right conditions (McCarthy et al., 2011).

The GPe projections to striatal FSIs present an interesting possible source of beta transfer to the striatum. Because FSIs have numerous inhibitory synapses onto SPNs, and these inhibitory connections increase after dopamine depletion (Gittis et al., 2011a), FSIs are poised to have an even stronger control over SPN ensembles in dopamine depletion. Excessive inhibitory regulation by FSIs may prevent SPN ensembles from being able to initiate movements. In addition, the strong GPe projection to FSIs may propagate abnormal beta synchrony throughout striatum, causing an even stronger dearth of computational power. This is one possibility of how striatal microcircuitry may contribute to akinesia in dopamine depletion conditions.

1.3.2 Compulsive Behaviors are Associated With Greater Activity in Striatum

Hyperactivity in corticostriatal microcircuitry is associated with compulsive or unintentional behavioral selection in several disorders. Human imaging studies have identified abnormalities in cortical and striatal regions in Obsessive Compulsive Disorder (OCD) and Tourette Syndrome (Chamberlain et al., 2008; de Wit et al., 2012a; Harrison et al., 2009; Leckman et al., 2010; Maia et al., 2008; Menzies et al., 2008). More specifically, hyperactivity and hyperconnectivity in corticostriatal circuits has been observed in OCD patients both at baseline and during symptom provocation (Chamberlain et al., 2008; de Wit et al., 2012a; Figee et al., 2013; Harrison et al., 2009; Maia et al., 2008; Menzies et al., 2008). Furthermore, deep brain stimulation treatment (DBS) which reduces OCD symptoms also reduces hyperconnectivity in frontal corticostriatal circuits (Figee et al., 2013). Thus, heightened activity in these circuits seems to play

a role in unwanted behaviors, but the mechanisms behind how increased activity in striatum lead to inappropriate behavioral output are unclear.

In keeping with previous explanations, it follows that heightened activity in striatal ensembles may lead to increased initiations of behaviors. In support of this idea, enhancement of excitatory activity in corticostriatal circuits, via disinhibition, causes tic-like behaviors in rodents (Bronfeld et al., 2013; Pogorelov et al., 2015; Worbe et al., 2012). Similarly, a mouse model of compulsive behavior, the *Sapap3*-KO mouse, displays hyperactivity in striatum both at baseline and during conditioned compulsive grooming (Burguiere et al., 2013).

These effects appears to be mediated in part by FSIs. Stimulation of corticostriatal terminals that disrupts compulsive grooming and corrects striatal hyperactivity also synchronizes FSI firing, suggesting that cortical inputs to FSIs may mediate this physiological effect (Burguiere et al., 2013). Furthermore, deficiencies in striatal FSIs have also been seen in Tourette's patients (Kataoka et al., 2010), and inhibition of FSIs in healthy mice causes spontaneous dyskinetic movements (Gittis et al., 2011b). Interestingly, the literature on Tourette Syndrome and related tic disorders supports a link between striatal hyperactivity and increased behavioral initiations via heightened dopamine activity in striatum (Albin et al., 2003; Saka et al., 2004; Saka and Graybiel, 2003; Singer et al., 1991), an opposite effect from decreased behavioral initiations in states of dopamine depletion. Thus, it is likely that there are several mechanisms contributing to striatal hyperactivity in OCD and Tourette Syndrome, including hyperconnectivity between cortex and striatum, reduced activity in striatal FSIs, and heightened dopamine activity in striatum.

1.4 Summary and Aims of Dissertation

In sum, both historical and recent data suggest that specific striatal subcircuits and more generalized striatal microcircuitry play diverse and complex roles in behavioral selection. The aims of this dissertation were to utilize diverse techniques and animal models for disease states to begin to understand how striatal microcircuitry plays a role in behavioral output. In Chapter 2, I will describe an ex vivo electrophysiological investigation of the non-canonical pallidostriatal connection to FSIs and use a computational model to understand how movement-preventing beta oscillations may emerge in this circuit in dopamine depletion conditions. In Chapter 3, I will detail synaptic corticostriatal microcircuitry abnormalities that may underlie region-specific striatal hyperactivity in a mouse model of compulsive behavior. Finally, in Chapter 4, I will explore the in vivo implications of these specific corticostriatal synaptic abnormalities and probe circuits to begin to understand how this dysfunction leads to increased behavioral output in the form of compulsive grooming. To conclude, I will discuss the implications of these findings and what my current work has taught us about behavioral selection in striatal microcircuits.

2.0 Pallidostriatal Projections Promote β Oscillations in a Dopamine-Depleted Biophysical Network Model

2.1 Introduction

A hallmark of basal ganglia dysfunction in Parkinson's disease (PD) is the amplification of synchronous, rhythmic activity, particularly in the β frequency range (13-30 Hz) (Bergman et al., 1998; Bevan et al., 2002; Gatev et al., 2006; Hutchison et al., 2004). Though some clinical data and results from animal models suggest that β oscillations are not causal to motor symptoms (Leblois et al., 2007; Mallet et al., 2008b), their reduction is correlated with symptomatic improvement (Hammond et al., 2007; Kühn et al., 2006; Kühn et al., 2009; Little and Brown, 2012); therefore, understanding how β oscillations originate, propagate, and can be mitigated could be of potential therapeutic value. While the mechanistic origins of β oscillations remain unknown, a number of models have been proposed, many of which involve the globus pallidus externa (GPe) (Holgado et al., 2010; Kita et al., 2007; Kumar et al., 2011; Mallet et al., 2008a; Pavlides et al., 2015).

Under dopamine-depleted conditions, GPe neurons fire synchronously and rhythmically (Bergman, 2004; Heimer et al., 2006; Mallet et al., 2008a; Nini et al., 1995; Raz et al., 2000), and GPe deep brain stimulation disrupts pathological β oscillations and improves movement in PD patients (Vitek et al., 2004; Vitek et al., 2012). Although GPe's contributions to β oscillations have generally been attributed to its reciprocal connections with the subthalamic nucleus (STN) (Brown

et al., 2001; Magill et al., 2001; Mallet et al., 2008a; Plenz and Kital, 1999; Tachibana et al., 2008), feedback projections from GPe to striatum (pallidostriatal) might also be involved.

Some anatomical data suggests that pallidostriatal projections are enriched onto GABAergic interneurons in striatum (Bevan et al., 1998; Mastro et al., 2014), which widely influence striatal output. Data from intracellular recordings of MSNs firing *in vivo* suggest that individual action potentials are evoked by disinhibition – the transient drop in powerful synaptic inhibition from fast-spiking interneurons (FSIs) (Wilson, 2009). Pauses in FSI spiking might arise through several pathways, but the pallidostriatal pathway represents an intriguing candidate because it may modulate FSIs independently of MSNs, unlike excitatory inputs, which target both cell populations (Wilson, 2009). This function of the pallidostriatal pathway is speculative, but opposing GPe and FSI activity in rats performing a delayed choice task (Gage et al., 2010) suggests a role for the pallidostriatal pathway during certain phases of behavioral selection.

We hypothesize that under dopamine-depleted (DD) conditions, the influence of the pallidostriatal pathway on FSIs becomes a critical component of a positive feedback loop, also involving enhancement of connectivity from FSI to indirect-pathway medium spiny neurons (iMSNs) (Gittis et al., 2011a), which can generate or amplify pathological synchrony and rhythmicity. To test this idea, we recorded the synaptic strength of pallidostriatal projections onto FSIs and MSNs in the striatum of acute slices from control and DD mice and then used this data in the construction of a conductance-based computational model of the pallidostriatal loop. Although anatomical studies have described a subset of GPe neurons that project to both FSIs and MSNs (Abdi et al., 2015; Dodson et al., 2015; Fujiyama et al., 2016; Hernández et al., 2015; Mallet et al., 2012; Sato et al., 2000), our synaptic data reveal that GPe projections onto MSNs are weak relative to their projections onto FSIs, suggesting a predominantly GPe-FSI-MSN architecture for

the functional pallidostriatal circuit. In our model of this circuit, GPe-FSI projections significantly impact the temporal organization of striatal activity, including pauses in FSI spiking, in a way that is essential for the emergence or amplification of β oscillations under network conditions simulating the DD state. These results suggest a novel circuit mechanism through which the pallidostriatal pathway shapes basal ganglia activity and promotes pathological rhythmicity in disease.

2.2 Materials and Methods

2.2.1 Animal Surgery and Viral Injections

Injections of adenoassociated virus 2 (AAV2)– human synapsin-1 gene promoter (hSyn)–channelrhodopsin 2 (ChR2)–EYFP or –mCherry (University of North Carolina Vector Core Facility) were made into the globus pallidus externa (GPe) of 4- to 5-week-old mice of both sexes. To facilitate targeted recordings of interneurons, Lhx6-GFP mice or striatal injected PV-cre mice were used. Anesthesia was induced using 50 mg/ml ketamine and 15 mg/ml xylazine and maintained throughout surgery using 2% isoflurane. Mice were placed in a stereotaxic frame (David Kopf Instruments), the scalp was opened, and bilateral holes over the GPe were drilled in the skull (0.17 mm anterior, 2.12 mm lateral from bregma). 200 nL of virus were injected with a Nanoject (Drummond Scientific) through a pulled glass pipette (30 μm tip diameter) (3.75 mm from the surface of the brain). PV-cre mice were injected with an opposite color fluorophore (500-700nL) in the dorsolateral striatum (relative to bregma, 1.15 mm anterior and 2.12 mm lateral, 2.75 mm from the surface of the brain). Mice were unilaterally dopamine-depleted via injection of

1uL of 6-hydroxydopamine (6-OHDA) into the medial forebrain bundle (relative to bregma, -.50 mm anterior and 1.10 mm lateral, 5.05 mm from the surface of the brain). Animals were housed for at least 2 weeks after injection for recovery and viral expression before recordings were conducted.

2.2.2 Electrophysiological Recordings

Parasagittal sections (300 μm thickness) containing the striatum and GPe were prepared from brains of 5- to 8-week-old mice of either sex that received ChR2 viral injections. Slices were prepared with a LeicaVT1000S vibratome in carbogenated ACSF containing (in mM): 125 NaCl, 26 NaHCO3, 2.5 KCl, 1 MgCl2, 2 CaCl2, 1.25 NaH2PO4, 12.5 glucose, 2 Mg-ATP, and 0.3 Na-GTP, pH 7.25. Slices were allowed to recover for 15 min at 33°C in a chamber filled with N-methyl-D-glucamine (NMDG)–HEPES recovery solution (in mM): 93 NMDG, 2.5 KCl, 1.2 NaH2PO4, 30 NaHCO3, 20 HEPES, 25 glucose, 10 MgSO4, 0.5 CaCl2, 5 sodium ascorbate, 2 thiourea, and 3 sodium pyruvate. Slices were then held at room temperature for at least 1 h before recording in a holding solution that was similar to the HEPES cutting solution but with 1mM MgCl2 and 2 mM CaCl2. Recordings were made at 33°C in carbogenated ACSF (in mM): 125 NaCl, 26 NaHCO3, 1.25 NaH2PO4, 2.5 KCl, 12.5 glucose, 1MgCl2, and 2 CaCl2.

Data were collected with a MultiClamp 700B amplifier (Molecular Devices) and ITC-18 analog-to-digital board (HEKA) using Igor Pro software (Wavemetrics) and custom acquisition routines (Recording Artist; Richard C. Gerkin, Phoenix, AZ). Current-clamp recordings were filtered at 10 kHz and digitized at 40 kHz; voltage-clamp recordings were filtered at 2 kHz and digitized at 10 kHz. Electrodes were made from borosilicate glass (pipette resistance, 2–6 MΩ).

The internal solution for voltage-clamp recordings consisted of the following (in mM): 120 CsMeSO3, 15 CsCl, 8 NaCl, 0.5 EGTA, 10 HEPES, 2 Mg-ATP, 0.3 Na-GTP, and 5 QX-314. The internal solution for current-clamp recordings consisted of the following (in mM): 130 KeMSO3, 10 NaCl, 2 MgCl2, 0.16 CaCl2, 0.5 EGTA, 10 HEPES, 2 MgATP, and 0.3 Na-GTP.

ChR2 terminals were activated by shining white light through a 473 nm filter cube with a 40nm bandwidth focused through the microscope objective onto the field of view. Inhibitory post-synaptic currents (IPSCs) were evoked by applying two 1ms light pulses with an inter-pulse interval of 100ms. Maximal responses were measured by increasing the light power (maximal power = 1 mW) until the evoked IPSC amplitude plateaued.

2.2.3 Immunohistochemistry

Slices that were used for data collection were fixed and resectioned at 30µm for further immunohistochemistry and processing. Tyrosine hydroxylase was stained using rabbit anti-TH primary antibody (1:1000, Pel-Freez) incubated for 24 hours at room temperature. Sections were then incubated in Alexa-Fluor 647 anti-rabbit (1:500, Life Technologies) for 1.5 hours at room temperature. Quantification of dopamine remaining was achieved by normalizing TH fluorescence in striatum to adjacent cortex and comparing normalized fluorescence in the depleted and non-depleted hemispheres.

Assessment of ChR2 viral spread was completed by enhancing and imaging ChR2-EYFP or by imaging ChR2-mCherry without enhancement necessary. ChR2-EYFP was enhanced with chicken anti-GFP (1:1000, aves Lab. Inc) incubated for 24 hours at room temperature. Sections

were then incubated in AlexaFluor 488 anti-chicken (1:500, Life Technologies) for 1.5 hours at room temperature.

2.2.4 GPe Viral Targeting Quantification

All processing of images and quantification was performed in ImageJ (National Institutes of Health). To quantify GPe fill, images were thresholded to the average background pixel intensity within GPe. The "Fill Holes" feature was applied to binary images to account for false negative pixels due to naturally occurring striation in the tissue. Mean pixel intensity of three 10 x10 pixel squares within GPe of each section was averaged to calculate average background pixel intensity. Measuring background level of fluorescence within GPe insured that any fluorescent collateral fibers would not be included in the quantification of viral soma expression. The number of pixels within GPe above threshold was expressed as a percentage of the total number of pixels occupied by GPe in the image to yield the percent fill. Percent fill values were averaged across 2-3 slices per animal.

2.2.5 Biophysical Network Model

We developed a computational representation of the pallidostriatal circuit by combining published, single-compartment models of three cell types: medium spiny neurons (MSN, (Mahon et al., 2000)) and fast spiking interneurons (FSI, (Golomb et al., 2007)) and globus pallidus externa neurons (GPe, (Fujita et al., 2012)). In each of these models, each cell's membrane potential V (mV) is governed by a differential equation specified in a conductance-based framework:

$$C_m \frac{dV}{dt} = \sum_X I_x$$

where C_m is membrane capacitance (μF/cm^2) and each I_x is a voltage-dependent intrinsic or synaptic current (μA/cm^2) in the set of currents X. Each intrinsic current is governed by the equation

$$I_x = g_x m_x^p n_x^q (V - V_x)$$

where g_x is maximal conductance (mS/cm^2), V_x is the reversal potential for the ion(s) in the current, and m and n are open fractions of voltage-dependent activation and inactivation gates, respectively, with integer exponents p and q. If a cell does not have an activation or inactivation gate, the corresponding m or n is set to 1. Otherwise, states of gates are governed by the equation

$$\frac{dm_x}{dt} = \frac{m_x^\infty - m_x}{\tau_{m_x}}$$

(and equivalently for n_x) where τ_{m_x} is the time constant for the gate and m_x^∞ is the voltage-dependent steady state value for m_x given by the Boltzmann equation

$$m_x^\infty = \frac{1}{1 + e^{(V - \theta_{m_x})/\sigma_{m_x}}}$$

(and equivalently for n_x) with constants θ_{m_x} and σ_{m_x}

Each published model includes a set of experimentally observed intrinsic currents, with parameters based on experimental findings, such that voltage traces produced by the models match experimental data (Fig. 2C).

In the MSN model (Mahon et al., 2000), the time constants for standard and slowly inactivating sodium (Na^+) and potassium (K^+) currents and for the persistent Na^+ current are voltage-dependent. As originally published, some gating variable equations in the model are presented in terms of voltage-dependent rates of channel opening and closing rather than a decay

to steady state with a time constant, but this representation is mathematically equivalent to the one presented above. We altered the published model by reducing the reversal potential for the L current to -90 mV based on more recent experimental findings (Gertler et al., 2008).

The GPe model (Fujita et al., 2012) includes a calcium (Ca^{2+}) dependent K^+ channel that deviates from the above framework and also includes incomplete inactivation of persistent Na^+, Kv2, and Kv3 channels. To better match the model's published traces, we reduced the conductance of the KCNQ-type channel to 0.15 mS/cm^2. In addition, to reduce computation time, we removed the s-gate of Na^+ channels and combined the fast and slow Kv4-type channels into a single channel covering their combined time constant ranges. Neither of these reductions had any effect on the qualitative behavior of the simulated GPe neurons.

The FSI model (Golomb et al., 2007) does not deviate from the above framework, and we made no changes to the published model.

We chose biologically realistic population proportions. MSNs make up at least 95% of all striatal cells (Kemp and Powell, 1971), approximately half of which are D2-expressing. Though both D1- and D2-MSNs send projections to GPe, the predominant striatal input to GPe is from D2-MSNs (Matamales et al., 2009), so only these MSNs were included in our model. We chose to simulate 40 **D2-**MSNs and 8 FSIs, a ratio of 5:1, which is approximately that seen *in vivo* (Gittis et al., 2010). Based on these numbers and the relative proportions of striatum to GPe (Oorschot, 1996), we chose to model 8 GPe cells.

The network architecture is shown in Fig. 2A-B, with connection probabilities ($C_{Pre\text{-}Post}$, where *Pre* and *Post* indicate the presynaptic and postsynaptic cell type, respectively) given in Table 2.1. Specific connections between cells were established randomly such that each cell in a

population receives an equal number of connections from a presynaptic population, given by the product of $C_{Pre\text{-}Post}$ with the total number of cells in the presynaptic population.

Table 2.1 Connectivity parameters for each modelled connection based on experimental observations.

Synaptic parameters used in the model were taken directly from experimental data when possible and were estimated based on empirical observations otherwise.

Pre	Post	$C_{Pre-Post}$	g_{syn}	a	b	θ_S	σ_S	Source
GPe	FSI	37.5%	0.12	2	0.23	-10.8	2	Figure 1; Bevan, et al., 1998
FSI	MSN	37.5% (75% in DD)	0.15	2	0.13	-0.8	2	Gittis, et al., 2010, 2011; Guzman, et al., 2003
MSN	GPe	37.5%	0.07	2	0.08	-0.8	2	Chuhma, et al., 2011; Shink and Smith, 1995; Miguelez, et al., 2012
GPe	GPe	25%	0.1	2	0.08	-10.8	2	Bar-Gad, et al., 2003; Bugaysen, et al., 2013; Miguelez, et al., 2012
FSI	FSI	62.5%	0.05	2	0.19	-0.8	2	Gittis, et al., 2010
MSN	MSN	35%	0.09	2	0.1	-5.8	2	Gertler, et al., 2008; Taverna, et al., 2008; Guzman, et al., 2003

$C_{MSN-MSN}$, $C_{MSN-FSI}$, and $C_{FSI-FSI}$ were taken directly from published values (Gertler et al., 2008; Gittis et al., 2010; Taverna et al., 2008). A given GPe cell receives approximately one GPe connection for every eight MSN connections (Shink and Smith, 1995). We thus chose $C_{MSN-GPe}$ and $C_{GPe-GPe}$ to maintain this ratio, which slightly overestimates published values for $C_{GPe-GPe}$ (Bar-Gad et al., 2003; Bugaysen et al., 2013), while underestimating $C_{MSN-GPe}$ (Chuhma et al., 2011). There is sparse data on $C_{GPe-FSI}$, but of GPe cells that project to striatum (the only GPe cells modelled here), 19-66% of their synapses are on FSI's (Bevan et al., 1998). Since all recorded FSI's were innervated by GPe (Fig. 1) and we do not model all GPe connections (such as those to SNr), we chose a $C_{GPe-FSI}$ such that $C_{GPe-FSI}$ / ($C_{GPe-FSI}$ + $C_{GPe-GPe}$) fell near the upper bound of this

range. When the GPe-MSN connections were included (Fig. 4), $C_{GPe\text{-}MSN}$ was chosen to be the same as $C_{GPe\text{-}FSI}$.

Each inhibitory synaptic current in the model is given by the equation

$$I_{syn} = g_{syn} s(V - V_{Cl}) \quad (1)$$

where V is the voltage of the postsynaptic cell, V_{Cl} is the reversal potential of chloride (-80mV), the primary ion contributing to current flow through GABAergic channels. In equation (1), s is a voltage-dependent synaptic gating variable governed by

$$\frac{ds}{dt} = aH(V)(1 - s) - bs$$

where a and b are channel opening and closing rates, respectively, and H is a smooth, monotone-increasing approximation of the Heaviside step function. Simulations including axonal conduction delays showed that the qualitative activity of the model was no different from the model without synaptic delays (data not shown), so for simplicity, delays were not included. The parameters a, b and g_{syn} for each type of synapse were calculated by matching simulated IPSCs to experimentally measured IPSCs in terms of decay time and maximum amplitude (Table 2.1). When unitary IPSC data was available (MSN-MSN: (Guzmán et al., 2003; Taverna et al., 2008); FSI-MSN: (Gittis et al., 2010; Guzmán et al., 2003); FSI-FSI: (Gittis et al., 2010)), we determined the single-synapse conductance for our model by multiplying the experimental unitary conductance by the ratio of the number of contacts from one presynaptic cell to one post-synaptic cell *in vivo* (Guzman, et al., 2003) divided by the number of contacts in our model. For IPSCs based on optical stimulation (MSN-GPe: (Miguelez et al., 2012); GPe-FSI: Fig. 1; GPe-GPe: (Miguelez et al., 2012)), we calculated the total conductance and divided by the number of contacts in our model.

Excitation to striatum (e.g., from cortex) and to GPe (e.g., from the subthalamic nucleus) is modeled as an ungated channel with current governed by

$$I_{ex} = g_{ex}(V - V_{cat})$$

where V is the postsynaptic voltage and V_{cat} is a cation reversal potential of 0 mV. Simulations used passive excitation except when otherwise noted, with constant g_{ex} chosen to best approximate published in vivo firing rates (Berke, 2008; Gage et al., 2010; Kita and Kita, 2011). In simulations including oscillatory excitatory inputs, g_{ex} is governed by

$$g_{ex} = g_{min} + (g_{max} - g_{min}) * (\sin(2\pi tf) + \sigma) \quad (2)$$

where $g_{max} - g_{min}$ = 1 mS/cm^2 is the amplitude of the oscillatory component, with g_{min} tuned to produce experimentally observed firing rates, f is the frequency of the input, and σ is a random variable that simulates random channel fluctuations, drawn at each time step from the distribution

$$\sigma \sim \frac{1}{4}\begin{cases} e^{x/2} & x < 0 \\ e^{-x/2} & x > 0 \end{cases}$$

chosen for its symmetry and accumulation of mass near zero.

Dopamine depletion was simulated in the model by 1) doubling the FSI-MSN connection probability (Gittis et al., 2011a) and 2) increasing MSN firing rate (Azdad et al., 2009; Fino et al., 2007; Kita and Kita, 2011) through an increase of excitatory current conductance (g_{ex}) of MSN neurons.

The model was simulated in XPPAUT (Ermentrout, 2012). Differential equations were solved numerically using Runge-Kutta integration with an adaptive time step (QRK method in XPPAUT) sampled every 0.1ms. Unless otherwise noted, models were run for 9500ms of simulated time and the first 500ms were discarded. For each set of results reported, three sets of connectivity matrices were generated, the model was simulated three times with each set of matrices, and results were averaged. Initial conditions for channel gating variables were set within

small neighborhoods of their rest values, and an initial condition for each cell's voltage was chosen randomly between -80 and -40 mV, independently across runs. For comparisons between healthy and DD conditions, the same random seed was used in each pair of trials compared.

2.2.6 Model Analysis

Results were exported for analysis in MATLAB (version 2014b). Spikes were detected from traces with a threshold voltage of 0 mV. Local field potentials (LFP) from a population were modeled as a low-pass filtered (250 Hz cutoff) average of the population voltage. Power spectral densities of LFP's were calculated by computing the squared Fast Fourier Transform of the LFP. Spectrograms were generated using the MATLAB function `specgram` with a window size of 4098 samples and a sliding window overlap of 3483 samples. Power within particular frequency bands was calculated from power spectra using the MATLAB function `bandpower` with a broadband range of 13-30Hz for beta frequency and 40-80Hz for gamma frequency. Assessment of power enhancement by applied oscillatory stimuli was computed within a narrow frequency band around the stimulus frequency: 3-13Hz for theta, 20-30Hz for beta, and 55-65Hz for gamma. Differences between the control and DD circuit's amplification of applied oscillations were quantified by subtracting the control power in the population of interest from its power in DD. Peak power was determined by finding the maximum value of the power spectral density within the 13-30Hz (beta) or 40-80Hz (gamma) frequency range.

Spike synchrony was computed by modifying the voltage synchrony metric presented by Golomb and Rinzel (1993), using counts of spikes binned into 15 msec bins. With $a_i(t)$ defined as the binned spike count over time for cell i, we compute the within-cell variance σ_i^2 and population variance σ_{pop}^2 as

$$\sigma_i^2 = \langle a_i(t)^2 \rangle_t - \langle a_i(t) \rangle_t^2,$$

$$\sigma_{pop}^2 = \langle a(t)^2 \rangle_t - \langle a(t) \rangle_t^2,$$

where $a(t) = (a_1(t)+\ldots+a_N(t))/N$ for a population of N neurons and the brackets denote averaging over our total simulation time, to find the synchrony measure χ as the ratio

$$\chi = \frac{\sigma_{pop}^2}{\frac{1}{N}\sum_{i=1}^{N} \sigma_i^2}.$$

When classifying spikes as "synchronous" or "asynchronous", synchronous spikes were defined as spikes accompanied by at least three other spikes from the same population within 10ms on either side, and asynchronous spikes were all spikes that did not meet this criterion. We computed spike-triggered spike latency probability distributions by locking onto spikes from a presynaptic population and computing the latency to spiking of each neuron in a population downstream (connected either monosynaptically or disynaptically). Pauses in FSIs were defined as epochs of at least 20 ms during which at least 6 (of 8) FSIs were silent. Power spectral densities of spikes and pauses were computed as above on binary vectors over time, where a 1 is placed at the onset of a spike or throughout a pause.

Instantaneous firing rate for a single cell was calculated by convolving its spike train (with each spike treated as a δ function) with a scaled Gaussian with 5 ms standard deviation and peak equal to 1. Instantaneous population firing rate plots were calculated by averaging the instantaneous firing rates of all cells within a population.

2.2.7 Statistical Methods

All statistical comparisons on electrophysiology data were performed using the Wilcoxon Rank Sums (WRS) test because the data was not normally distributed. Comparisons of the percentages of responding cells were conducted using a Fisher Exact Test (FET). Data from the model was compared using one-way ANOVAs and two-tailed t-tests when indicated.

2.3 Results

2.3.1 Pallidostriatal Projections are Selective for Interneurons

To investigate the synaptic projections from GPe to striatum, inhibitory currents were recorded in different striatal cell types in response to optical activation of GPe terminals (Fig. 2.1A). Recordings were conducted in slices from control and unilaterally dopamine-depleted animals, two weeks after 6-OHDA injection into the medial forebrain bundle. To achieve widespread ChR2 expression in GPe neurons, mice were stereotaxically injected at the time of dopamine depletions with AAV2 carrying ChR2 under the synapsin promotor (Fig. 2.1B). Viral spread was quantified and slices were excluded if less than ~40% of the GPe was infected (range: 44-84%, mean: 61.3%) or there was more than 100 μm spread into the striatum (Fig. 2.1B, right, see Methods). Variability in infection volume did not correlate with variability in response sizes ($r(9) = .22$, $p = 0.39$, Fig. 2.1F).

To target different striatal cell populations, recordings were performed in transgenic mouse lines that label GABAergic interneurons in striatum (see Methods). Most recordings were

conducted on simultaneously recorded pairs of interneurons and MSNs (Fig. 2.1C), but in some instances, recordings were done on sequentially patched pairs of neurons within 100 µm of each other. Neurotransmitter release from GPe terminals in the field of view was evoked with 1 ms pulses of white light, filtered through a 470 nm filter cube with a 40 nm bandwidth. Maximal light-evoked inhibitory post-synaptic currents (IPSCs) were observed in all FSIs sampled, and were similarly large in both control and DD conditions (control: 566 ± 560 pA, n = 37; DD: 844 ± 647 pA, n = 39; WRS, $p = 0.12$, Fig. 2.1E). In contrast, responses in MSNs were only observed in 38% (13/34) of MSNs sampled in control slices, and 73% (19/26) of MSNs sampled after DD. The increase in fraction of responsive MSNs in DD slices was significant (FET $p < 0.01$, Fig. 2.1D). In MSNs where responses were observed, the average IPSC amplitude was significantly larger after DD compared to control (control: 28 ± 44 pA, n = 13; DD: 108 ± 73 pA, n = 21; WRS, $p < 0.01$, Fig. 2.1E), but still smaller than IPSCs recorded in FSIs in both conditions ($p < 0.00001$).

As shown in Fig. 1E, there was a tremendous amount of variability in the amplitude of maximally-evoked IPSCs. We attribute this to biological variability because within-neuron responses were consistent across trials (Fig. 2.1C) and the range of response variability was consistent from animal to animal (Fig. 2.1F). Biological variability in response amplitude might reflect the clustered distribution of GPe projections in striatum (Fig. 2.1B, *inset*), which is supported by our observations that FSIs with the largest responses tended to be near MSNs that also exhibited relatively large responses (Fig. 2.1G, $p = 0.08$).

In summary, our synaptic data confirm previously published anatomical work showing that pallidostriatal projections are highly enriched onto GABAergic interneurons (Bevan et al., 1998). Indeed, IPSCs were also observed reliably in persistent low-threshold spiking interneurons (PLTS) (159 ± 395 pA, n = 11), but these projections are not further characterized here. In contrast,

pallidostriatal projections onto MSNs were synaptically weak, a surprising result given recent descriptions of an anatomically-specialized subset of 'arkypallidal' GPe neurons that densely project to striatum and target both MSNs and GABAergic interneurons (Magill et al., 2012; Abdi et al., 2015; Dodson et al., 2015). A summary of the synaptic properties recorded at each synapse in healthy and DD conditions is provided in Table 2.2.

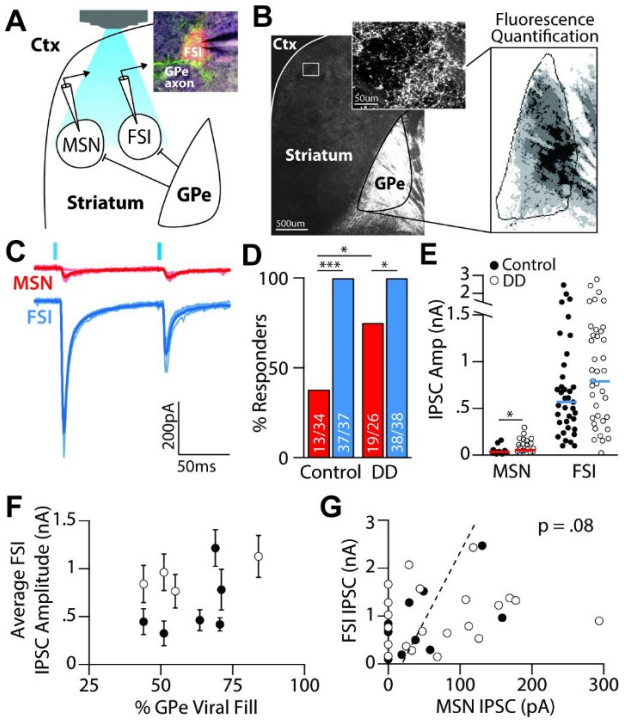

Figure 2.1 Pallidostriatal projections preferentially target interneurons.

A. Schematic of experimental configuration. ChR2-EFYP was expressed in GPe. Pallidostriatal terminals were optically activated locally within striatum. *Inset*: Image of ChR2-EYFP-expressing pallidostriatal terminals (*green*) surrounding a striatal *FSI* (red) targeted for recording. B. Raw fluorescent (*left*) and thresholded (*right*) images of a sagittal mouse brain slice, showing spread of ChR2-EFYP expression. C. Maximal light-evoked IPSCs measured in a simultaneously recorded MSN (*red*) and FSI (*blue*). Responses were calculated as the average (*thick line*) across five trials (*thin lines*). D. Percentage of MSNs (*red*) and FSIs (*blue*) which showed a synaptic response to pallidostriatal stimulation in control and DD slices. A significantly greater percentage of FSIs showed responses compared to MSNs in both control ($p < 0.0001$) and DD conditions ($p < 0.01$). A significantly greater percentage of MSNs showed responses in DD compared to control ($p < 0.01$). E. Evoked responses were significantly larger in FSIs than in MSNs in both control and DD conditions ($p < 0.00001$). Horizontal lines denote population medians. Median FSI response size did not differ significantly between control and DD conditions, while median response sizes from responding MSNs was significantly increased in DD ($p < 0.01$). F. Median values (*circles*) and SEMs (*error bars*) of FSI-IPSCs recorded in each mouse, plotted as a function of the % GPe viral fill, assessed histologically (B). Variability in IPSC amplitudes

did not correlate with the degree of viral fill. G. Scatter plot showing trending relationship of IPSC amplitudes between paired FSI and MSN recordings.

Table 2.2 Properties of synaptic recordings in healthy and dopamine depleted conditions

Properties of light-evoked synaptic responses from all recorded striatal cells. Values reported are median ± standard deviation. Like letters indicate a significant difference of $p < 0.05$ in a Wilcoxon Rank Sums Test.

	MSN		FSI		PLTS	
	Control	DD	Control	DD	Control	DD
N	34	26	37	38	11	N/A
Max IPSC (pA)	0 ± 39.5^{abd}	57.9 ± 80.8^{ac}	565.9 ± 560.2^{be}	843.8 ± 643.8^{c}	159.0 ± 395.5^{de}	N/A
Min IPSC (pA)	N/A	N/A	28.1 ± 54.1	29.6 ± 12.0	N/A	N/A
Input Resistance (MΩ)	200.2 ± 97.7	191.6 ± 221.5	134.9 ± 55.2	184.2 ± 79.4	1328.5 ± 631.2	N/A
Decay constant (ms)	7.0 ± 2.5	7.7 ± 3.0^{f}	4.5 ± 1.8	5.0 ± 6.0^{f}	$8.0 \pm .3$	N/A

2.3.2 Construction of a Biophysically Detailed Model of the GPe-FSI-MSN Loop

GPe has been implicated in promoting network synchrony and oscillations in the basal ganglia of human patients and in animal models of PD (Bergman et al., 1998; Brown et al., 2001; Hutchison et al., 2004; Kühn et al., 2009; Magill et al., 2001; Mallet et al., 2008a; Nini et al., 1995), but the cellular mechanisms through which this occurs remain unknown. Much work has focused on GPe's reciprocal connections with the STN, but a number of other mechanisms are also likely to be involved, including GPe's reciprocal connections with striatum.

The striatum provides the major inhibitory input to GPe and synchrony across MSNs can contribute to pathological rhythmicity in GPe (Kita and Kita, 2011). By comparison, the reciprocal effects of feedback inhibition from GPe to striatum have been underexplored, despite the fact that

its enrichment for striatal interneurons makes it a strong candidate to influence synchrony and rhythmicity throughout the circuit (Gage et al., 2010; Gittis et al., 2011a).

To investigate the role of GPe projections onto FSIs in shaping striatal activity and the emergence or amplification of β oscillations, we created a 56-cell network model (8 GPe, 8 FSI, 40 MSN) composed of previously published, conductance-based single cell models for GPe neurons (Fujita et al., 2012), MSNs (Mahon et al., 2000), and FSIs (Golomb et al., 2007) (Fig. 2.2A). Neurons in the model were connected using experimentally observed connection probabilities and synaptic parameters (Table 2.1). To mimic synaptic changes in the network observed following DD, synaptic connections between FSI-MSN were doubled (from 37.5% to 75%) (Gittis et al., 2011a), but GPe-FSI (Fig. 2.1) and MSN-GPe (Miguelez et al., 2012) were not changed (Fig. 2.2B).

To confirm that our single-cell model outputs were consistent with experimental observations, we compared their firing responses to square depolarizing current steps with those measured experimentally (Fig. 2.2C). GPe neurons fired spontaneously and responded quickly to square pulses with increases in firing rate (Fig. 2.2C). In contrast, FSIs and MSNs did not fire spontaneously, but fired in response to depolarizing inputs. FSIs responded with an initial spike and a brief period of subthreshold membrane oscillations followed by sustained, repetitive firing, often with a minimum firing rate of >40 Hz (Fig. 2.2C). MSNs also exhibited a delay between depolarization and firing onset (Fig. 2.2C), most likely due to outwardly rectifying K^+ currents present in these neurons (Nisenbaum et al., 1996; Surmeier et al., 1991; Wilson and Kawaguchi, 1996).

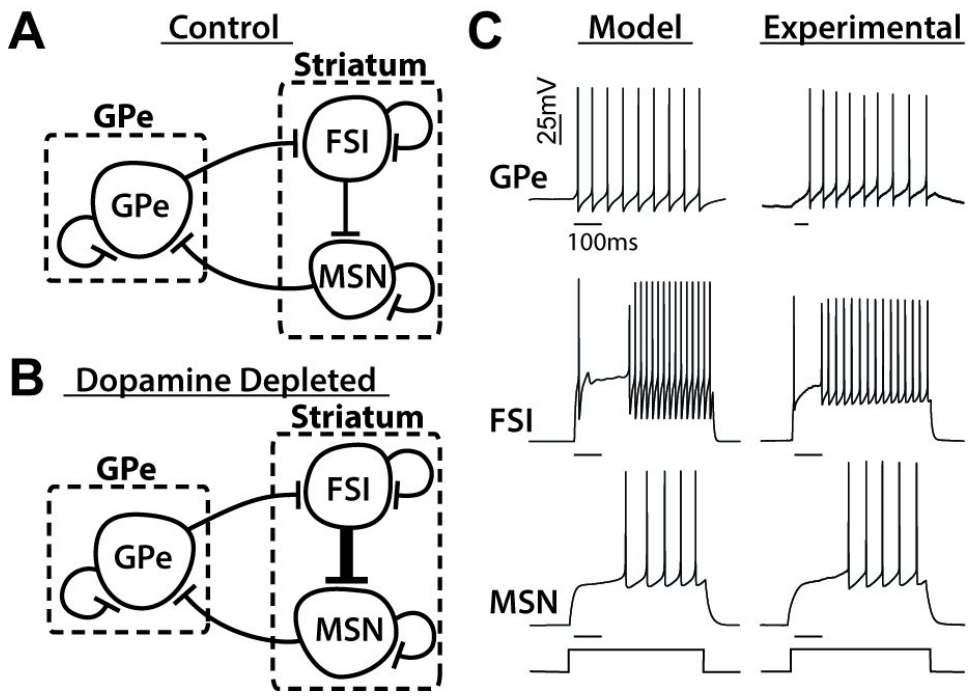

Figure 2.2 Developing a conductance-based 3-population pallidostriatal network model.

A. Schematic of the conductance-based network model, built from published cell models connected synaptically with experimentally-observed values for connection probabilities and strengths (Table 2.1). The models contained 40 MSNs, 8 GPe cells, and 8 FSIs. B. A DD network was created by doubling the number of connections from FSIs to MSNs. C. Responses of model neurons and experimentally recorded neurons to square depolarizing current injections. Scale bar corresponds to 100 ms.

2.3.3 GPe-FSI-MSN Loop is Sufficient to Produce β Under DD Conditions

To study the effects of dopamine loss on the dynamics of the GPe-FSI-MSN loop, we simulated network activity in control and DD conditions. The conductance (g_{ex}) of a passive excitatory channel (see Methods) was tuned in each population to generate average firing rates that match experimentally recorded values *in vivo* (Berke, 2008; Gage et al., 2010; Kita and Kita, 2011) (Fig. 2.3A). MSNs fired at 2.0 ± 0.24 Hz in control and 5.0 ± 0.63 Hz in the DD model ($p < 0.0001$, Fig. 2.3B) (Azdad et al., 2009; Fino et al., 2007; Kita and Kita, 2011). GPe neurons fired

at 24.5 ± 1.14 Hz in control and 18.9 ± 0.87 Hz in the DD model ($p < 0.0001$; Fig. 2.3B) (Boraud et al., 2001; Kita and Kita, 2011). FSIs fired at 21.4 ± 0.75 Hz in control and 23.7 ± 0.69 Hz in the DD model ($p < 0.0001$, Fig. 2.3B) (Hernandez et al., 2013).

To evaluate the firing dynamics of single neurons, raw voltage traces were analyzed to determine the spike times of single action potentials (Fig. 2.3A, *top*). To evaluate population activity as a whole, voltage traces in each neuron were low-pass filtered (250 Hz cutoff), and the results were averaged across neurons to obtain what we called a pseudo-local field potential (pseudo-LFP) (Fig. 2.3A, *bottom*). The pseudo-LFP does not accurately represent extracellular LFPs recorded *in vivo*, but it captures subthreshold activity and is therefore a suitable signal with which to assess oscillatory activity.

In the control network, firing of individual neurons was largely asynchronous across all three neuronal populations despite their synaptic interactions. Under DD conditions, epochs of synchronous activity emerged, as seen in DD animal models and PD patients (Hammond et al., 2007; Kühn et al., 2009; Mallet et al., 2008b) (Fig. 2.3C). To quantify synchrony, we assessed the proportion of neurons spiking within specified time bins for each population (see Methods) and observed a significant increase in spike synchrony for each neuronal population in the DD network ($GPe_{control}$: 0.14 ± 0.045, GPe_{DD}: 0.24 ± 0.01, $p < 0.00001$; $MSN_{control}$: 0.046 ± 0.015, MSN_{DD}: 0.124 ± 0.045. $p < 0.00001$; $FSI_{control}$: 0.167 ± 0.021, FSI_{DD}: 0.181 ± 0.48, $p < 0.05$, Fig. 2.3D).

To determine whether the observed increases in synchrony were accompanied by changes in the degree or frequency of rhythmicity within the network, we constructed power spectra for the pseudo-LFPs from each population in the control and DD networks (Fig. 2.3E). In the control network, spectral power in GPe was low, with the exception of a small peak at 38 Hz, in the range of high β/low γ (Fig. 2.3E). In contrast, GPe in the DD model showed β frequency activity (3.04

$\pm$ 1.68 x 10^9 V^2/Hz) that was 9-fold greater than in control (0.65 $\pm$ 0.24 x 10^9 V^2/Hz, $p < 0.0001$, Fig. 2.3E-F), with a peak centered at 23 Hz.

A significant increase in spectral power in the β frequency range was also observed in MSNs and FSIs in the DD network. While MSNs showed some β activity in control (1.24 $\pm$ 0.27 x 10^9 V^2/Hz), consistent with experimental findings (Courtemanche et al., 2003), they showed significantly more β activity in the DD model (3.16 $\pm$ 0.93 x 10^9 V^2/Hz, $p < 0.0001$, Fig. 2.3E-F). FSIs also showed a significant increase in β range activity in the DD model (0.60 $\pm$ 0.12 x 10^9 V^2/Hz) compared to control (0.53 $\pm$ 0.05 x 10^9 V^2/Hz, $p < 0.01$, Fig. 2.3E-F), but this effect was small. Taken together, these results suggest that the intrinsic dynamics of the GPe-FSI-MSN loop are sufficient to generate substantial β oscillations. Notably, prominent β oscillations did not emerge in the control network, suggesting that pallidostriatal circuit dynamics specifically in DD are necessary for increased spike synchrony and β oscillations.

One of the surprising aspects of these results was that β oscillations were propagated throughout the circuit in DD despite the fact that the FSI population, a major circuit node, did not display strong β activity. Indeed, although some β power was observed in the FSI population, most power in the spectrum occurred within the γ frequency range (40 – 80 Hz), centered around 46.5 Hz (Fig. 2.3E). This property of the FSI population is consistent with experimental findings showing that FSIs resonate at γ frequency (Berke, 2009; Cardin et al., 2009; Sohal et al., 2009; Van Der Meer and Redish, 2009). γ power was also observed to some degree in the MSN population following DD, consistent with the findings of Lemaire and colleagues (2012).

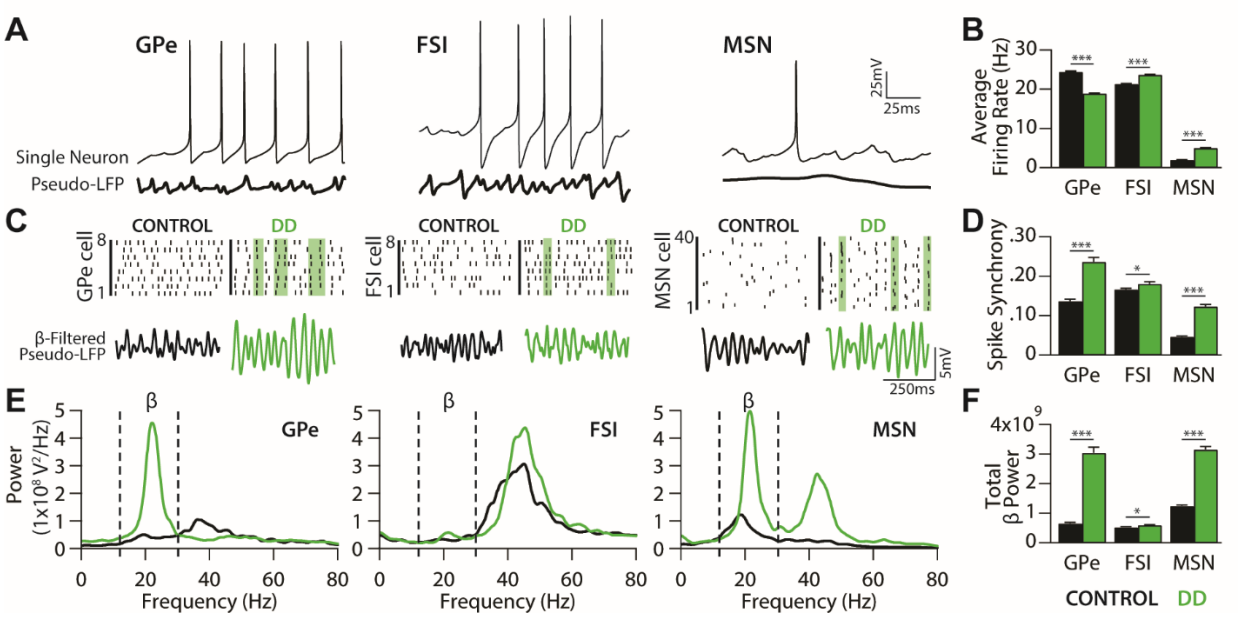

Figure 2.3 Pallidostriatal model exhibits enhanced synchrony and beta oscillations in simulated dopamine depletion.

A. Output of the model for each cell type. *Top*, Membrane voltage traces from individual cells. *Bottom*, Average low-pass filtered voltage trace across all neurons within a population ("pseudo-LFP"). B. Average firing rates for each cell population under control (*black*) and DD (*green*) conditions. Values were averaged across the output of nine runs for each condition (three runs for each of three connectivity matrices). C. *Top*: Spike rasters showing the timing of action potentials across all cells in each population, under control and DD conditions. Green shaded areas denote example periods of spike synchrony. *Bottom*: Corresponding pseudo-LFPs calculated during the same epochs shown above in rasters. D. Average spike synchrony for each cell population across nine runs of a control (*black*) and DD network (*green*). All cell populations showed a significant increase in spike synchrony in DD. E. Average power spectral densities computed from pseudo-LFPs (smoothed for display purposes) across nine runs of a control (*black*) and DD network (*green*). Note the increase in β activity (13-30 Hz, *dashed lines*) in DD for each population. F. All cell populations showed a significant increase in β power. Two sample t-tests were conducted to assess statistical differences, *indicates $p < 0.05$, * indicates at least $p < 0.0001$. All group values shown as mean ± SEM.**

2.3.4 GPe-MSN Connections Do Not Affect Model Rhythmicity

While GPe synapses onto MSNs are much weaker than those onto FSIs, their strength shows a small but significant increase in DD. To test whether these synapses affect the dynamics of the pallidostriatal model in DD, we added GPe-MSN connections to the DD model using experimentally-derived parameters (Fig. 2.4A, Table 2.2). The addition of GPe-MSN connections in the DD model caused no significant change ($p > 0.05$) in the β bandpower in any cell population (GPe, 2.48 ± 0.54; FSI, 0.61 ± 0.28; MSN, $2.87 \pm 0.29 \times 10^9$ V^2/Hz, Fig. 2.4B-C). Spike synchrony was similarly unaltered from the normal DD model in GPe (0.21 ± 0.03, $p = 0.26$) and FSIs (0.17 ± 0.01, $p = 0.92$), and was slightly but significantly decreased in MSNs (0.10 ± 0.01, $p < 0.05$, Fig. 2.4D). Adding GPe-MSN connections into the control model similarly had very little effect on its dynamics (data not shown).

These data suggest that the GPe-MSN synapses, though strengthened in DD, do not have a large effect on β or spike synchrony in the control or DD state. As we predicted based on our physiology data (Fig. 2.1), it seems that the pallidostriatal projections to FSIs, but not to MSNs, are important for the circuit dynamics studied here. The insignificance of the GPe-MSN connection validates our focus on the GPe-FSI-MSN loop as a key circuit in DD dysfunction.

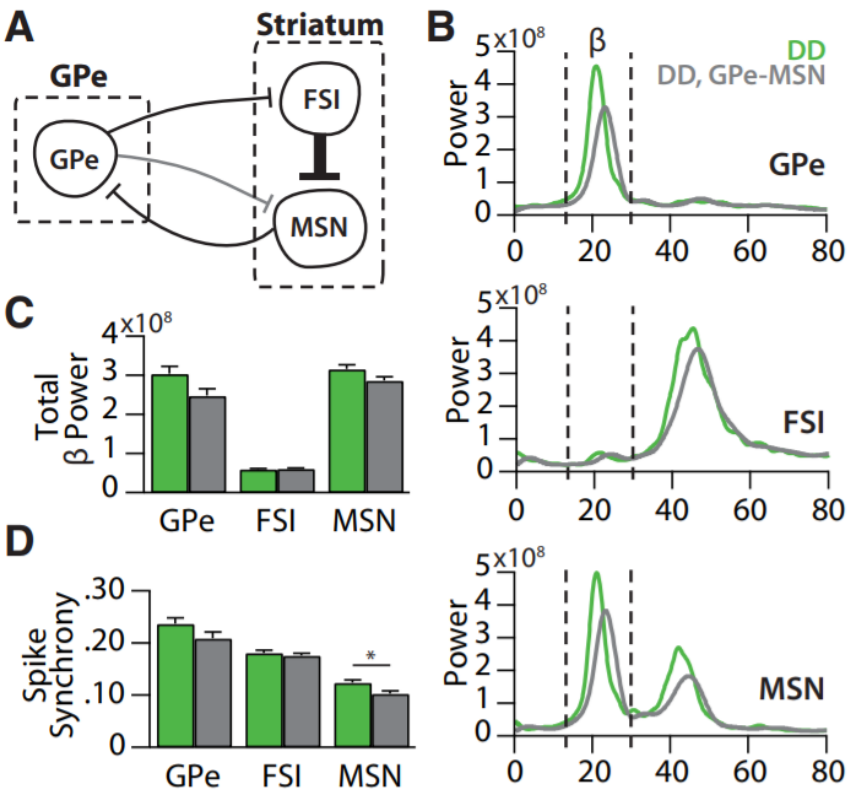

Figure 2.4 GPe-MSN synapses are not strong enough to influence DD circuit dysfunction.

A. Schematic showing the addition of GPe-MSN connections into the DD circuit. B. Average power spectral densities calculated in each cell population under DD conditions (*green*) or DD conditions with GPe-MSN connections added (*grey*). Power in units of $1x10^8$ V^2/Hz. C. Total β power (13-30 Hz) in each cell population in DD and DD plus GPe-MSN networks. GPe-MSN connections did not significantly alter the β power in any cell populations (all $p > 0.05$). D. Average spike synchrony in each cell population in DD and DD plus GPe-MSN networks. GPe-MSN connections slightly and significantly altered the spike synchrony in MSN's ($p < 0.05$) but did not affect spike synchrony in GPe or FSIs ($p > 0.05$). Comparisons between conditions were assessed using two sample t-tests on raw power or synchrony values. Plots display average values ± SEM.

2.3.5 The GPe-FSI Projection Significantly Enhances Synchrony and is Necessary for β Oscillations

To determine the role of GPe input to FSIs in the development of altered activity exhibiting β oscillations in the DD network, we replaced GPe input with randomly timed inhibitory inputs to FSIs (Fig. 2.5A). These random inhibitory stimuli maintained the overall amount of inhibition onto FSIs, but with timing decoupled from the activity of GPe neurons. This disruption of the GPe-FSI projection largely prevented β oscillations from developing in the DD network in all cell populations (Fig. 2.5B). In GPe, total β band power was 4.7-fold higher in the complete DD network compared to control, but only 2.3 fold higher with a less defined peak when GPe-FSI was disrupted ($1.47 \pm 0.66 \times 10^9$ V^2/Hz, $p < 0.00001$, Fig. 2.5C, *purple*). The mechanism driving residual β in the absence of GPe-FSI is not clear but might be related to residual effects of FSI γ in the network (see Discussion). In MSNs, disrupting the GPe-FSI connection reverted the 2.6-fold increase in β power seen in the DD network to control level ($1.22 \pm 0.33 \times 10^9$ V^2/Hz, $p < 0.00001$, Fig. 2.5C, *red*). Similarly, the increase in β power in FSIs in the DD network, although small, was also reversed by disrupting GPe-FSI ($0.40 \pm 0.45 \times 10^9$ V^2/Hz, $p < 0.00001$, Fig. 2.5C, *blue*). In contrast, γ oscillations were relatively unaffected by this manipulation, demonstrating that disruption of the GPe-FSI projection does not simply eliminate rhythmicity in the network altogether, but rather specifically reduces β frequency oscillations.

DD-induced spike synchrony also decreased in all populations when the GPe-FSI connection was disrupted (GPe, 0.18 ± 0.06; FSI, 0.14 ± 0.04; MSN, 0.08 ± 0.02; $p < 0.001$, Fig. 2.5D-E). FSI synchrony decreased to lower than control levels ($p < 0.001$), indicating that GPe input to FSIs not only is essential for β oscillations, but also serves to synchronize FSIs (Fig. 2.5E, *blue*). Interestingly, while MSN retained significant synchrony under disruption of GPe-FSI,

consistent with previous results that the FSI-MSN connection by itself is capable of increasing synchrony in MSNs in DD (Gittis et al., 2011a), its synchrony was only about half of that seen with GPe-FSI intact, highlighting another way in which the pallidostriatal influence permeated the DD network (Fig. 2.5E, *red*). Similarly, GPe synchrony remained significantly greater than control but with significantly reduced magnitude ($p < 0.001$, Fig. 2.5E, *purple*), suggesting that increased MSN synchrony is a major factor in the synchrony of GPe activity. Taken together, these results suggest that GPe input to FSIs is necessary for β oscillations in the DD circuit and that this effect may be mediated in part through its contributions to the enhancement of synchronization throughout the circuit.

It is possible that these reductions in β power and synchrony are due not to the disrupted GPe-FSI connection but rather due to the random inhibition on FSI's used to replace GPe. To rule out this possibility, we retained the GPe-FSI connection but incrementally reduced the conductance of the synapses. Unlike the GPe-FSI disruption, this manipulation did not include replacement of the inhibition onto FSIs; that is, it preserved input timing but weakened its magnitude. Decreases in GPe-FSI strength were significantly correlated with decreases in the total β power in GPe and MSNs ($p < 0.01$, Fig. 2.5F). The decrease in β as GPe-FSI strength is reduced is consistent with the loss of β activity when the GPe-FSI connection is completely disrupted, providing further evidence that the GPe-FSI connection is crucial for β oscillations in the DD network model.

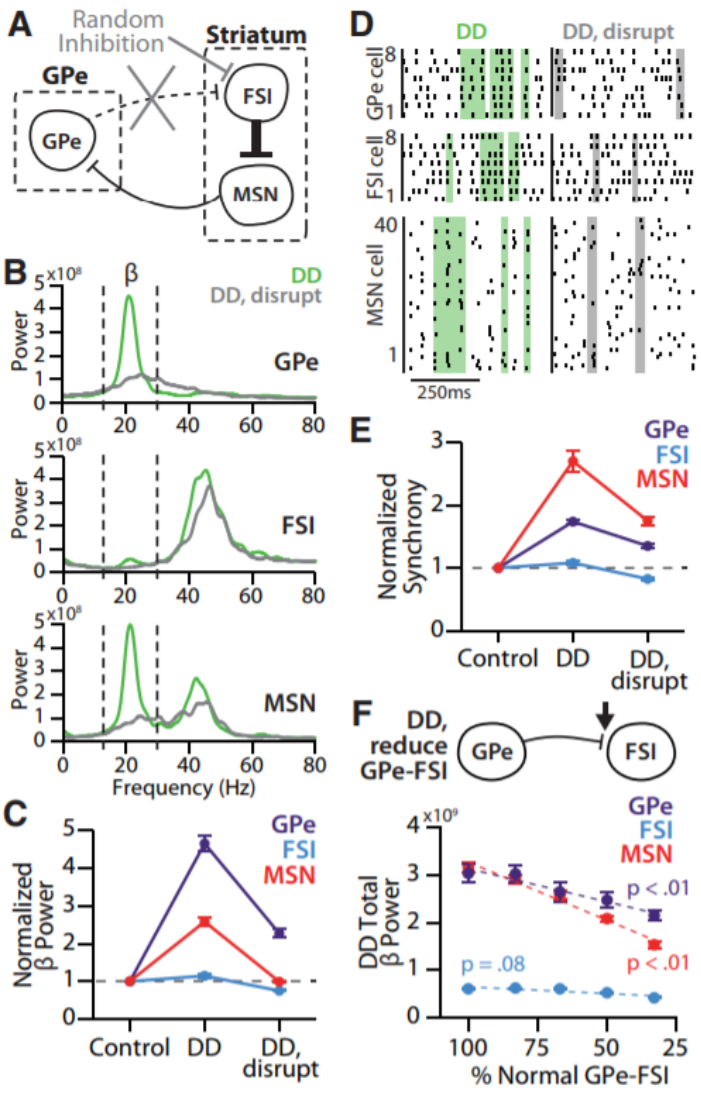

Figure 2.5 GPe-FSI connection is necessary for β activity in DD.

A. Schematic showing how GPe-FSI connections were replaced with randomly timed inhibitory inputs at the same frequencies. B. Average power spectral densities calculated in each cell population under DD conditions (*green*) or DD conditions with GPe-FSI disrupted (*grey*). Power in units of $1x10^8$ V^2/Hz. C. β power (normalized to control) in each cell population in DD and DD disrupted networks. GPe-FSI disruption caused a reduction in β power in all cell populations ($p < 0.0001$). D. Representative spike rasters for each cell population firing in a DD or DD disrupted network. Shaded areas denote example periods of spike synchrony. E. Average spike synchrony (normalized to control) in each cell population in DD and DD disrupted networks. GPe-FSI disruption caused a reduction in synchrony in all cell populations ($p < 0.0001$). F. *Top*, Schematic

representation of simulations of a DD network, in which the GPe-FSI connection was kept intact but conductance values were reduced. *Bottom*, β power in each cell population in a DD network, with diminishing values of GPe-FSI conductance. Reducing the strength of the GPe-FSI synapses was significantly correlated with a reduction in total β band power in GPe and MSNs ($p < 0.01$). Comparisons between conditions were assessed using two sample t-tests on raw power or synchrony values. Plots display average values normalized to control (C, E) or average raw power values (F) ± SEM.

2.3.6 Synchronous GPe Spikes Rhythmically Synchronize FSI Pauses and MSN Spikes

To determine how the GPe-FSI pathway promotes β oscillations in the DD circuit despite the absence of high β power in the FSI population, we further investigated patterns in GPe spiking. GPe spike synchrony is increased in the DD model (Fig. 2.3C-D), which, we reasoned, might alter the effect that GPe input has on FSI activity. To explore this possibility, GPe spikes were separated into two categories: synchronous spikes, which occurred within 10 ms of spikes from at least three other GPe cells (Fig. 2.6A), and asynchronous spikes, which did not meet this criterion. As expected, there was a significantly higher proportion of synchronous spikes in GPe in DD (0.72 ± 0.10) than in control (0.55 ± 0.10, $p < 0.00001$, Fig. 2.6B).

This increase in synchronous GPe spikes in DD could have important implications for circuit dynamics if synchronous and asynchronous GPe spikes cause different responses in the FSI population. To establish how synchronous and asynchronous GPe spikes differentially affect FSI activity, we computed the probability distribution for the latency of an FSI's first spike (averaged over all FSIs) after each synchronous or asynchronous GPe spike (Fig. 2.6C). In both control and DD conditions, FSIs were significantly less likely to spike following a synchronous GPe spike (control: 0.13 ± 0.03, DD: 0.12 ± 0.03) than after an asynchronous GPe spike (control: 0.21 ±

0.003, DD: 0.21 ± .01, $p < 0.00001$) (Fig. 2.6D). Thus, the increase in synchronous GPe spikes in DD allows GPe to have a stronger functional influence on FSI activity.

To further explore this decrease in FSI spike probability, we investigated FSI population pauses, defined by a period of at least 20 ms during which at least 6 of the 8 FSIs did not fire (Fig. 2.6G). Consistent with our findings that synchronous GPe spikes more strongly reduce FSI firing probability, and that there are more synchronous spikes in DD, we observed that there were significantly more FSI pauses in DD (178.3 ± 45.3) than in control (111.9 ± 25.08, $p < 0.001$).

The increase in functional strength of the GPe-FSI pathway in DD does not, on its own, explain why the GPe-FSI connection is necessary for the generation of β oscillations in the DD circuit. To assess the capacity of GPe spikes to promote oscillations, we calculated power spectra of synchronous and asynchronous GPe spikes (Fig. 2.6E). Synchronous GPe spiking occurs with strong β power in control ($3.86 \pm 0.30 \times 10^4$ V^2/Hz), and this effect is significantly enhanced in the DD circuit ($5.69 \pm 0.87 \times 10^4$ V^2/Hz, $p < 0.0001$, Fig. 2.6E-F). Asynchronous spiking in GPe does not show strong power in any frequency bands in control or DD (Fig. 2.6E). In order for rhythmic, synchronous spiking of GPe to influence downstream β activity, the induced FSI pauses must also occur at β frequency. Power spectra computed on the time series of FSI pauses (Fig. 2.6G-H) confirm that there is greater β range power in FSI pauses in DD ($4.38 \pm 0.96 \times 10^7$ V^2/Hz) than in control ($2.91 \pm 0.57 \times 10^7$ V^2/Hz, $p < 0.001$, Fig. 2.6H-I). These results suggest that despite the prominent γ oscillations in FSI pseudo-LFP activity in both control and DD conditions (Fig. 2.3E), synchronized pauses in FSI population activity occur at β frequency in DD and thus may be critical in propagating β activity throughout the pallidostriatal circuit.

To see how GPe-induced FSI pauses affect MSNs, probability distributions for MSN latency to fire were generated aligned to synchronous GPe spikes (Fig. 2.6J). MSNs showed

increased probability of firing in the 5-15 ms window after a synchronous GPe spike (control: 0.088 ± 0.003, DD: 0.092 ± 0.012) compared to asynchronous GPe spikes (control: 0.058 ± 0.003, DD: 0.03 ± 0.003, $p < 0.0001$). As with GPe, there were no significant differences between control and DD models. The critical difference between control and DD MSN spiking was instead in the patterning of synchronous spikes. Synchronous MSN spiking occurred at β frequency (Fig. 2.6K), and the amount of β activity was greater in the DD model ($8.93 \pm 1.95 \times 10^4$ V^2/Hz) than in control ($5.81 \pm 0.39 \times 10^4$ V^2/Hz, $p < 0.0001$, Fig. 2.6L). This amplification suggests that in DD, enhanced GPe synchrony carries over to MSN rhythmicity, while MSN input to GPe in turn reinforces GPe β activity.

Taken together, these data demonstrate how the GPe-FSI pathway promotes β activity in the DD circuit. In control and DD conditions, synchronous GPe spikes are able to cause synchronized FSI pauses in a way that asynchronous GPe spikes cannot. Synchronized GPe spikes tend to occur at β frequency, and thus FSI pauses and the resulting MSN disinhibition windows also occur at β frequency. In DD, because there are more synchronous GPe spikes, GPe more strongly organizes pauses in FSI firing. Correspondingly, MSNs in DD also display increased spike synchrony and increased β activity, and their synchronous β input to GPe reinforces heightened synchrony and β oscillations throughout the network.

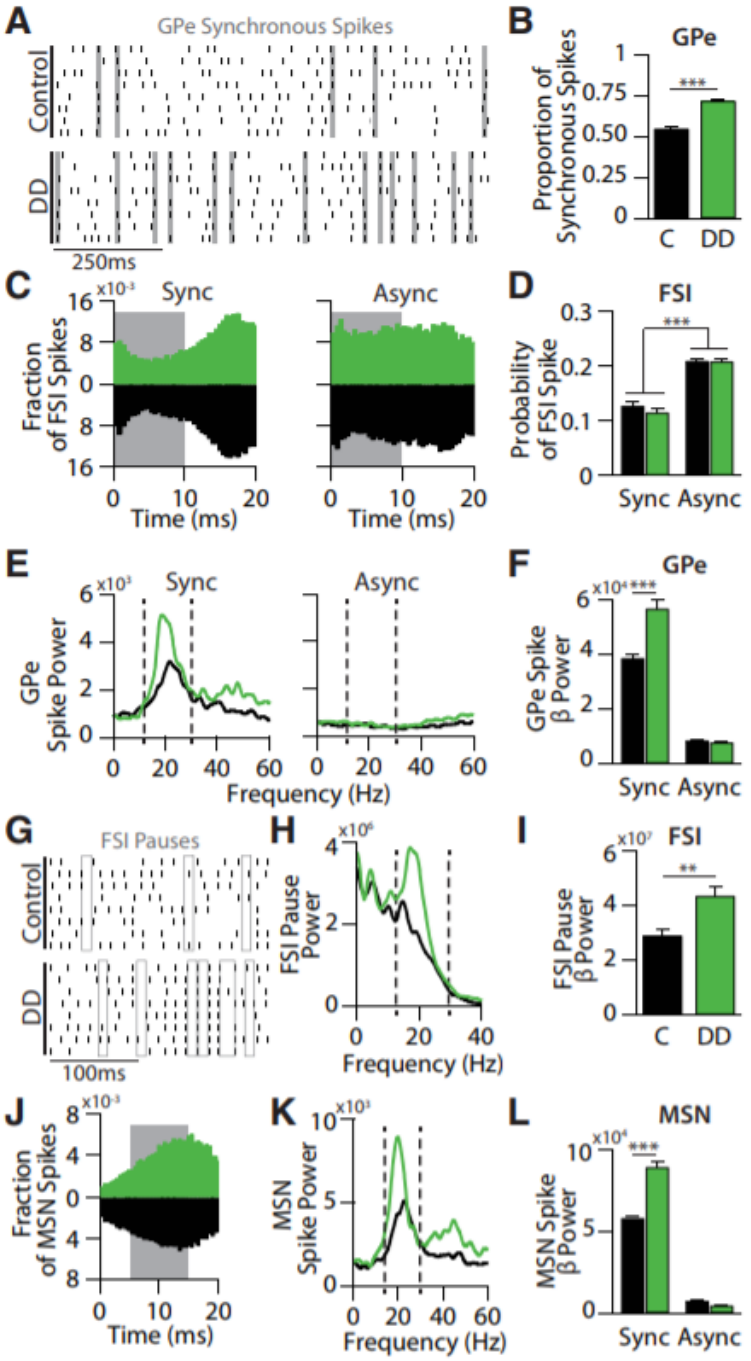

Figure 2.6 Rhythmicity in synchronous GPe spikes entrains FSI pauses and promotes β in the circuit.

A. Representative spike rasters showing 1 s of firing across all 8 GPe neurons in a control and DD network. Gray shaded areas denote example periods of spike synchrony. B. Bar graph comparing the proportions of all GPe spikes that were classified as either synchronous or asynchronous. In DD networks, a significantly greater proportion of GPe spikes were synchronized than in control networks ($p < 0.0001$). C. Probability distributions

of FSI spikes following synchronous and asynchronous GPe spikes in control (black) or DD networks (green). Gray boxes indicate 10 ms window over which FSI spike probabilities were calculated. D. Bar graph comparing the spike probabilities of FSIs (gray boxes, C) immediately after synchronous or asynchronous GPe spikes. In both control and DD networks, FSI spike probabilities were significantly lower following synchronous GPe spikes than asynchronous GPe spikes ($p < 0.0001$). E. Average power spectral densities calculated from spike rasters of synchronous or asynchronous GPe spikes in control (black) or DD (green) networks. F. Bar graph quantifying average spectral power in the β frequency range (13-30 Hz, dashed lines in E) following synchronous or asynchronous GPe spikes in control (black) and DD (green) networks. β power after synchronous spikes was significantly greater in DD networks compared to control ($p < 0.0001$). G. Representative spike rasters showing 250 ms of firing across all 8 FSI neurons in a control and DD network. Open boxes denote examples of FSI pauses, which occur more frequently in DD than in control. H. Average power spectral densities calculated from FSI pauses in control (black) or DD (green) networks. I. Bar graph quantifying average spectral power in the β frequency range (13-30 Hz, dashed lines in H) of FSI pauses in control (black) and DD (green) networks. β power of FSI pauses was significantly greater in DD networks than in control ($p < 0.001$). J. Probability distributions of MSN spikes following synchronous GPe spikes in control (black) or DD networks (green). Gray box indicates 10 ms window over which MSN spike probabilities were calculated. It was offset by 5 ms to account for the disynaptic connection from GPe to MSNs. K. Average power spectral densities calculated from synchronous MSN spikes in control (black) or DD (green) networks. L. Bar graph quantifying average spectral power in the β frequency range (13-30 Hz, dashed lines in K) of synchronous and asynchronous MSN spikes in control (black) and DD (green) networks. β power of synchronous MSN spikes was significantly greater in DD networks than in control ($p < 0.0001$). No β power was observed in asynchronous MSN spikes in either control or DD networks. All values shown as mean ± SEM. ** indicates $p < 0.001$, * indicates $p < 0.0001$ after a two-tailed t-test.**

2.3.7 β Oscillations are Selectively Amplified in the GPe-FSI-MSN Loop

Our simulations and data analyses have established that the model GPe-FSI-MSN loop has an intrinsic capacity to generate β oscillations in DD. Given the associated positive feedback

mechanisms, the loop might also be expected to sustain or amplify β oscillations that originate elsewhere. Indeed, while the origin of pathological β oscillations in PD is unknown, both the STN and the cortex have been proposed as potential sources (Bronte-Stewart et al., 2009; Brown et al., 2001; Hirschmann et al., 2011; Jenkinson and Brown, 2011; Magill et al., 2001; Mallet et al., 2008a; Mallet et al., 2008b; Sharott et al., 2005; Tachibana et al., 2008; Weinberger et al., 2006). To assess how oscillations transmitted from such external sources affect dynamics within the GPe-FSI-MSN loop, we delivered I_{ex} with sinusoidal conductance g_{ex} to different nodes in our model to simulate an oscillatory input (see Methods).

When a β frequency excitatory oscillatory input (25 Hz) was delivered to GPe (Fig. 2.7A), spectrograms revealed that oscillations were propagated throughout the loop in both control and DD networks, but they were highly amplified in the DD network compared to control (Fig. 2.7B-C). β was increased in the DD network 2.2-fold over control in GPe, (control: 2.17 ± 0.24, DD: 5.04 ± 0.72 x 10^9 V^2/Hz, $p < 0.00001$), 2.2-fold in MSNs (control: 1.48 ± 0.48, DD: 3.26 ± 0.93 x 10^9 V^2/Hz, $p < 0.00001$), and 1.5-fold in FSIs (control: 0.96 ± 0.27, DD: 1.40 ± 0.30 x 10^9 V^2/Hz, $p < 0.00001$).

To determine whether the DD network propagates all oscillatory stimuli to the same degree, or whether this amplification is specific to β oscillations, we also applied sinusoidal input to GPe with one of two alternative frequencies to mimic γ oscillations (60 Hz) or θ (8 Hz) oscillations. γ oscillations (60 Hz) are thought to be pro-kinetic and have been reported to be decreased in PD circuits, while θ oscillations (8 Hz) have been shown to be increased in PD circuits (Brown and Williams, 2005; Cheyne et al., 2008; Hutchison et al., 2004; Jenkinson et al., 2013; Muthukumaraswamy, 2010; Sarnthein and Jeanmonod, 2007; Tass et al., 2010). Amplification of each stimulus was measured by subtracting band power from a narrow range around the stimulus

frequency (± 5 Hz) in the control network from the power in that range in the DD network for a given cell population (amplification = $Power_{DD} - Power_{Control}$). Oscillations imposed on GPe at γ and θ frequencies were no more strongly amplified in the DD network than in control. In GPe, the resulting γ power was actually diminished in the DD network relative to control ($p < 0.05$, Table 2.3). However, GPe γ power was propagated throughout the circuit, with some amplification in DD in MSNs and FSIs. Still, the γ amplification was much smaller than the β amplification in MSNs ($p < 0.00001$, Table 2.3) and not different from the degree of β amplification in FSIs ($p = 0.80$, Fig. 2.7C, Table 2.3). Likewise, θ power was amplified significantly less than β power in all cell populations ($p < .0001$, Fig. 2.7C, Table 2.3). These results indicate that oscillatory input to GPe will propagate throughout the circuit, suggesting that GPe, when synchronized by an oscillatory input, can pass information to other nodes in the circuit; importantly, however, the DD network showed a preferential amplification of β frequency oscillatory stimuli applied to GPe.

When a β frequency oscillatory input was delivered to striatum (Fig. 2.7D), β propagated throughout the loop in both control and DD conditions and once again was amplified in the DD network relative to control (Fig. 2.7E-F). This amplification in the DD network was most prominent in GPe (control: 0.74 ± 0.45, DD: $3.00 \pm 1.61 \times 10^9$ V^2/Hz, $p < 0.00001$) and MSNs (control: 2.44 ± 0.63, DD: $4.75 \pm 1.11 \times 10^9$ V^2/Hz, $p < 0.00001$) and less obvious in FSIs (control: 1.00 ± 0.27, DD: $1.17 \pm 0.27 \times 10^9$ V^2/Hz, $p < 0.01$). Combined with the data above, these results demonstrate that β oscillations applied to the pallidostriatal circuit at any node will be amplified, particularly under DD conditions.

We again asked whether θ or γ oscillations, now applied to striatum, were differentially amplified in the DD network relative to control. We observed a statistically significant increase (in GPe and FSIs) or decrease (in MSNs) in the power of θ oscillations in the DD network relative

to control (all cell populations, $p < 0.001$, Fig. 2.7F, Table 2.3), but these effects were small in magnitude. In contrast, we observed that γ applied to striatum produced a different effect on network dynamics than γ applied to GPe. Specifically, striatally-applied γ in FSIs was greater in the DD network ($6.29 \pm 3.09 \times 10^9$ V^2/Hz) than in control ($4.35 \pm 0.42 \times 10^9$ V^2/Hz, $p < 0.0001$, Fig. 2.7F, *blue*), likely reflecting the tendency of FSIs to resonate at γ frequency (Berke, 2009; Cardin et al., 2009; Sohal et al., 2009; Van Der Meer and Redish, 2009). Striatally-applied γ was also amplified in MSNs in the DD network ($2.12 \pm 1.17 \times 10^9$ V^2/Hz) relative to control ($1.12 \pm 0.12 \times 10^9$ V^2/Hz, $p < 0.00001$), though the degree of amplification was significantly less than that for striatally-applied β oscillations ($p < 0.001$, Fig. 2.7F, *red*, Table 2.3). In GPe, little amplification of γ occurred (control: 0.32 ± 0.02, DD: $0.45 \pm 0.28 \times 10^9$ V^2/Hz, $p = 0.19$). Indeed, the DD amplification of striatal β oscillations in GPe ($2.25 \pm .48 \times 10^9$ V^2/Hz) was significantly greater than DD amplification of striatal γ oscillations ($0.13 \pm .30 \times 10^9$ V^2/Hz, $p < .001$, Fig. 2.7F, *purple*). Thus, overall, DD amplification of oscillatory input to striatum was preferential for β frequency, suggesting again that the pallidostriatal circuit has a tendency to promote β oscillations in the DD network.

Striatal stimulation at γ frequency also significantly enhanced β power in MSNs in the DD network ($5.13 \pm 0.66 \times 10^9$ V^2/Hz) relative to control ($1.79 \pm 0.09 \times 10^9$ V^2/Hz, $p < .0001$), and this amplification was significantly greater than DD amplification of β input ($p < 0.01$) and intrinsic β ($p < 0.01$) in MSNs (data not shown). In contrast, γ stimulation of the GPe did not enhance β activity in the circuit any more than the normal DD enhancement of intrinsic β activity. Likewise, θ stimulation of striatum or GPe did not significantly enhance intrinsic DD β activity. These results suggest a possible interaction between striatal γ and β activity in the circuit (see discussion).

Overall, these results suggest that the DD model circuit preferentially amplifies β frequency stimuli, whether applied to GPe or striatum, consistent with experimental evidence indicating an increase in β band oscillatory activity in the basal ganglia circuit in PD (Bronte-Stewart et al., 2009; Brown and Williams, 2005; Levy et al., 2002; Mallet et al., 2008a; Mallet et al., 2008b; Sharott et al., 2005; Weinberger et al., 2006). This preference for β amplification in DD, regardless of where β oscillations enter the circuit, indicates that the GPe-FSI-MSN loop will amplify β oscillations that originate in other regions of the brain, in addition to intrinsically generating β activity in DD.

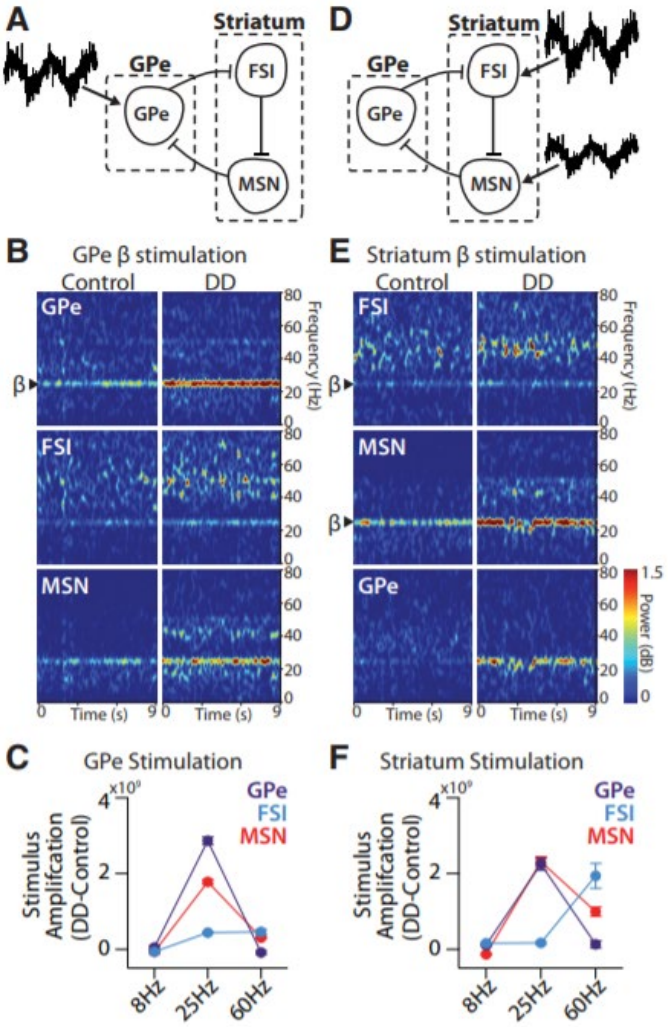

Figure 2.7 GPe-FSI-MSN loop selectively amplifies applied β oscillations in DD.

A. Schematic of a GPe-FSI-MSN network receiving an oscillatory stimulus applied to GPe. B. Spectrograms showing power across all frequencies (0 – 80 Hz) over the duration of a model simulation (9 s). β oscillations applied to GPe (arrow) were propagated to FSIs and MSNs in both control and DD conditions, but showed stronger power in DD than in control ($p < 0.00001$). C. Amplification (powerDD – powercontrol) of spectral power for each of three oscillatory inputs applied to GPe (□ = 8 Hz; β = 25 Hz; γ = 60 Hz). GPe and MSN populations amplified β more in DD than either □ or γ (see statistics in Table 4). FSIs amplified both β and γ equally (Table 4). D. Schematic of a GPe-FSI-MSN network receiving oscillatory stimuli applied to striatum. E. Spectrograms showing power across all frequencies (0 – 80 Hz) over the duration of a model simulation (9 s). β oscillations applied to FSIs and MSNs in striatum (arrows) were propagated to GPe in both

control and DD conditions, but showed stronger power in DD than in control ($p < 0.01$). F. Amplification of spectral power for each of three oscillatory inputs applied to striatum. GPe and MSN populations amplified β more in DD than either □ or γ (see stats in Table 4). FSIs in the DD network amplified γ more than any other frequency (Table 4). Power amplification in units of V2/Hz. All values shown as mean ± SEM.

Table 2.3 Amplification of oscillatory power in each circuit node when stimulus is applied to GPe or striatum Differences in DD amplification (DD stimulus bandpower – Control stimulus bandpower) of oscillatory stimulus. Power amplification in units of 1x109 V2/Hz. Values reported are median ± standard deviation. Asterisks show where pairwise comparisons between all three conditions were significantly different (at least $p < .05$) and like letters indicate a significant difference between pairs (at least $p < 0.05$). Pairwise comparisons were only computed following a significant one-way ANOVA.

		Applied to GPe			Applied to Striatum		
		8Hz	25Hz	60Hz	8Hz	25Hz	60Hz
Stim Power Amplification (DD-Control)	GPe	.04 ± .15*	2.87 ± .30*	-.09 ± .12*	.11 ± .06^{c}	2.25 ± .48^{cd}	.13 ± .30^{d}
	FSI	-.07 ± .06^{ab}	.44 ± .06^{a}	.45 ± .18^{b}	.15 ± .06^{e}	.17 ± .12^{f}	1.94 ± .99^{ef}
	MSN	-.07 ± .15*	1.78 ± .21*	.31 ± .06*	-.14 ± .06*	2.31 ± .39*	.99 ± .36*

2.4 Discussion

Our results reveal a novel mechanism through which the pallidostriatal pathway influences the functional coupling between the GPe and striatum. We show that within a GPe-FSI-MSN loop, transient synchronization occurs rhythmically at β frequencies and this effect is amplified by the pallidostriatal pathway under DD conditions, despite no change in the strength of GPe-FSI synaptic connections. DD-induced increases in synchrony and β power in GPe produce rhythmic

pauses in FSIs, via the pallidostriatal pathway, which enable MSNs to fire at β frequencies. Similar mechanisms yield amplification of β oscillations transmitted from neurons outside of the circuit. These results suggest that the pallidostriatal pathway shapes striatal output during periods of synchronous activity in GPe, which have been observed during certain behavioral tasks and in disease.

2.4.1 Synaptic Properties of Pallidostriatal Projections

Pallidostriatal projections are often overlooked in circuit models of the basal ganglia, but they have been described anatomically for over three decades (Beckstead, 1983; Bevan et al., 1998; Kita and Kitai, 1991; Mallet et al., 2012; Rajakumar et al., 1994; Sato et al., 2000; Staines and Fibiger, 1984; Staines et al., 1981). A number of pallidostriatal projections arise from axon collaterals of GPe neurons projecting to STN and SNr (Bevan et al., 1998), but a subset of GPe neurons, recently dubbed 'arkypallidal', project exclusively to striatum (Abdi et al., 2015; Dodson et al., 2015; Fujiyama et al., 2016; Hernández et al., 2015; Mallet et al., 2012; Sato et al., 2000). Axon collaterals of 'prototypic' GPe neurons (STN- and SNr-projecting) selectively innervate GABAergic interneurons in striatum (Bevan et al., 1998), but axons of arkypallidal neurons make synaptic-like contacts onto both interneurons and MSNs (Mallet et al., 2012).

In contrast to previous anatomical evidence, results from our synaptic experiments reveal that GABAergic responses recorded in MSNs in response to pallidostriatal stimulation are much weaker than those recorded in FSIs. If pallidostriatal projections are more distal onto MSNs than they are onto FSIs, synaptic responses might be attenuated before reaching the soma. However, our Cs-based internal should minimize signal attenuation from distal sites. It is possible that arkypallidal neurons did not strongly express ChR2, but this is unlikely because EYFP

fluorescence was detected in FoxP2^{+} neurons, a molecular marker of arkypallidal neurons (data not shown). Another possibility is that the release probability of pallidostriatal synapses onto MSNs is very low or that postsynaptic GABA receptors are absent from these synapses. After dopamine-depletion, IPSC amplitude was increased in MSNs but the paired pulse ratio was not changed (PPR not shown), suggesting that changes in postsynaptic GABA receptors could be involved. Nonetheless, our results suggest that pallidostriatal projections do not exert the same degree of fast GABA-mediated inhibition onto MSNs that they do onto FSIs.

In contrast, pallidostriatal projections evoked strong IPSCs in FSIs. These responses likely arise from axon collaterals of 'prototypic' GPe neurons but projections from arkypallidal neurons might contribute as well. The large amplitude and rapid synaptic kinetics of these responses suggest that they mediate strong, fast synaptic inhibition capable of suppressing and/or synchronizing FSI activity, as previously proposed (Bevan et al., 1998; Shouno et al., 2009; Wilson, 2009; Gage et al., 2010).

2.4.2 Model β Activity is Generated Through GPe Synchronization at β Frequency

An important prediction of our model is that synchronous firing in GPe is required for the pallidostriatal pathway to influence striatal output. Synchronized firing in GPe produces a coordinated pause across multiple FSIs (Fig. 2.8B), which does not result from asynchronous spiking (Fig. 2.8A). This transient pause provides a window in which MSNs have a high probability of spiking (Fig. 2.8B). The disinhibitory role of the pallidostriatal pathway has been previously hypothesized from *in vivo* recordings (Wilson, 2009). Indeed, coordinated changes in GPe activity coincide with changes in FSI population activity at key decision points on a behavioral task (Gage et al., 2010).

In contrast to transient epochs of GPe synchrony that occur during behavioral selection in healthy animals (Courtemanche et al., 2003; Leventhal et al., 2012; Turner and Anderson, 2005), GPe synchrony is chronic in low dopamine (Hammond et al., 2007; Heimer et al., 2006; Kühn et al., 2009; Mallet et al., 2008a; Nini et al., 1995; Raz et al., 2000). This observation suggests that the pallidostriatal pathway exerts greater influence on striatal dynamics in PD. This prediction is supported in our model by observations that there are more synchronous FSI pauses in the DD network compared to control (Fig. 2.6). Furthermore, because the influence of FSIs over MSNs is increased by DD (Gittis et al., 2011a), FSI pauses become even more important in determining the timing of MSN spikes.

In our model, synchronous firing of GPe neurons exhibits β frequency rhythmicity, which in turn establishes rhythmicity in the pauses of FSIs and entrains MSN firing to β frequencies (Fig. 8B-C), both of which become more pronounced in the DD network due to the pallidostriatal pathway (Figs. 2.5-2.6). Synchronized MSN activation, particularly with the higher MSN firing rate in the DD condition, further reinforces β rhythms in GPe (Fig. 2.8B), which represent a physiological hallmark of BG dysfunction in PD (Bronte-Stewart et al., 2009; Brown et al., 2001; Levy et al., 2002; Mallet et al., 2008a; Mallet et al., 2008b; Sharott et al., 2005; Weinberger et al., 2006). The interplay between FSI γ activity, FSI β pauses, and MSN/GPe β activity is evident in instantaneous firing rate plots from the DD model (Fig. 2.8C).

In addition to our model's intrinsic β generation capability in DD, it exhibits preferential amplification of applied oscillations in the β band. Thus, the propensity of the DD network for β frequency activity could manifest either in the generation of rhythmic activity or in the propagation of oscillatory inputs originating outside the pallidostriatal loop. Additionally, stimulation of striatum at γ frequency enhances β activity in the DD state (data not shown), suggesting a

relationship between γ and β activity in the DD model, likely due to increased FSI-MSN inhibition, that is consistent with past observations in PD (De Hemptinne et al., 2013) and theoretical work (Whittington et al., 2000).

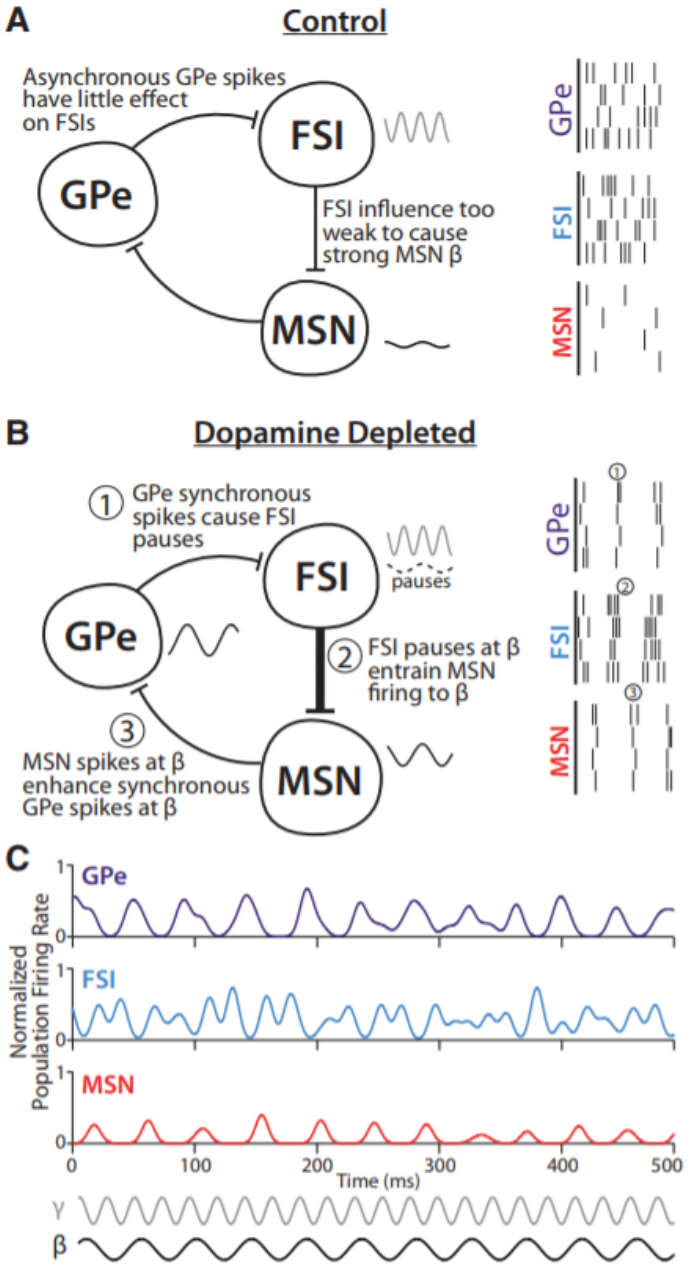

Figure 2.8 Proposed mechanism of synchrony and β oscillations.

A. In control conditions, firing synchrony in GPe is low, so there are few synchronized pauses in FSIs. Because pauses in FSIs are unsynchronized, spikes in MSNs exhibit little temporal structure. FSIs exhibit strong γ activity (red line), but their control over MSNs is too weak to cause strong MSN β (black line). B. In DD conditions, firing synchrony in the GPe is increased, especially at β frequencies (1, black line). This synchronizes pauses in FSIs to β frequencies (2, dashed black line) and entrains the pattern of MSN spikes to β (3, solid black line). Additional β entrainment of MSNs occurs via 2:1 entrainment from FSI γ activity (gray

line), because FSIs have a greater influence over MSNs in DD due to increased connection probabilities. Firing of MSN at β frequency further enhances β rhythmicity in GPe, which reinforces β and synchrony throughout the loop. C. Example instantaneous population firing rate plots for each cell type over 500 ms in the DD model. Simultaneous traces show how peaks of GPe firing at β frequency (purple) align with troughs in FSI firing at β frequency (blue). These pauses in FSI activity are followed by peaks in MSN firing at β frequency (red). Concurrently, FSI γ activity can be seen overlaid on the β oscillation, with two γ frequency peaks occurring between the β frequency pauses. Reference oscillations are shown at β (black, 22 Hz) and γ (gray, 44 Hz) frequencies.

2.4.3 Relation to Previous Models

Previous results have indicated that phasic striatal inhibition has a stronger impact than STN excitation on slow oscillations in GPe (Walters et al., 2007). Nonetheless, prominent theories of β in PD regard the GPe-STN reciprocal circuit as critical to the generation of oscillations (Brown et al., 2001; Kumar et al., 2011; Magill et al., 2001; Mallet et al., 2008a; Nevado-Holgado et al., 2014; Rubin and Terman, 2004; Terman et al., 2002). Our model suggests that, regardless of the source, the crucial mechanism in amplifying β oscillations in DD is rhythmic synchrony within GPe, which in turn strongly impacts striatal output. β activity in the STN could act as the synchronizer of GPe; in such a case, the amplification of β oscillations in the GPe-FSI-MSN loop could play a critical role in reinforcing STN oscillations, compatible with GPe-STN theories of β generation. Another potential synchronizer of GPe may be motor cortex, which has been shown to exhibit β activity in PD and to have direct connections to GPe (Jenkinson and Brown, 2011; Mallet et al., 2008b; Naito and Kita, 1994; Smith and Wichmann, 2015) in addition to its projections to striatum. Regardless of the site of origin, our model suggests a central role for GPe in amplifying

cortico-basal ganglia β oscillations in PD and predicts that compromising the pathway from GPe to FSIs should diminish β power elsewhere in the basal ganglia.

In our model, β activity in the MSN population, caused by precisely timed FSI population pauses, promotes synchronization of GPe. One previous model has shown how striatal β activity could develop in MSNs alone, without the inclusion of an FSI population or GPe inputs (McCarthy et al., 2011). We have suggested that the FSIs are crucial for β based on our finding that they receive strong input from the pallidostriatal pathway, earlier observations of increased FSI-MSN connection probability in DD (Gittis et al., 2011a), and the synchronizing effect of FSI pauses on MSN firing. Because our proposed mechanism for propagating oscillations relies on a β synchronization of GPe via MSNs, an MSN-only generation of β could be compatible with our central hypothesis, in which case our model would still offer new insights about propagation of rhythmicity throughout the pallidostriatal circuit. The work of Damodaran and colleagues (2015) supports a role for increased FSI inhibition in amplifying β oscillations but also suggests that decreased MSN-MSN connectivity is necessary for β emergence. In our model, while we do not implement a direct change in MSN lateral inhibition, we do include an increase in MSN firing rate in DD. Thus, our model predicts that any modification that yields increased MSN firing could play a similar role to plasticity in MSN connections in the emergence of β activity in DD.

2.4.4 Conclusion

This work highlights a novel dynamic capacity of a basal ganglia circuit composed of GPe and striatal neurons and provides an exploration of the involvement of the pallidostriatal projection in shaping circuit activity. The results suggest a pivotal role for GPe, through its projection to striatal FSIs, in synchronizing MSN activity and therefore striatal output. Through this connection,

GPe may serve to generate pathological β synchrony throughout multiple basal ganglia nuclei or to amplify oscillations transmitted to GPe from another source. This effect offers a complementary mechanism to previously identified pathways through which GPe may contribute to abnormal activity in Parkinsonism. The pallidostriatal connection may therefore merit further exploration as a modulator of information flow through basal ganglia pathways and as a target for interventions for Parkinson's disease.

3.0 Strengthened Inputs From Secondary Motor Cortex to Striatum in a Mouse Model of Compulsive Behavior

3.1 Introduction

Although stereotyped and compulsive behaviors are prominent, disabling, and notoriously-treatment resistant symptoms in multiple severe neuropsychiatric disorders, including Tourette Syndrome (TS) (Leckman et al., 2010), grooming disorders (e.g. skin-picking, trichotillomania (Chamberlain et al., 2009; Flessner et al., 2012), and Obsessive Compulsive Disorder (OCD) (Ayuso-Mateos, 2006; Karno et al., 1988; Menzies et al., 2008), little is known about their underlying neural mechanisms. Imaging studies in patients with OCD and other compulsivity-associated disorders have consistently identified both hyperactivity in the striatum (caudate head) and increased corticostriatal functional connectivity at baseline and when symptoms are expressed (Chamberlain et al., 2009; Del Casale et al., 2011; Denys et al., 2013; Figee et al., 2013; Harrison et al., 2009; Leckman et al., 2010; Maia et al., 2008; Menzies et al., 2008; Rauch et al., 1994; Rauch et al., 1997; Saxena et al., 1998). However, the cellular and synaptic abnormalities that underlie this hyperactivity are unclear.

Determining whether striatal hyperactivity originates in striatum or in upstream cortical projections could help inform whether neuromodulatory treatments for OCD-related disorders should target cortical or subcortical regions. Though striatal deep brain stimulation (DBS) has reported efficacy in OCD (Figee et al., 2013; Greenberg et al., 2010), studies demonstrating aberrant activity in corticostriatal circuits in OCD patients (Chamberlain et al., 2008; Del Casale et al., 2011; Figee et al., 2013; Harrison et al., 2009; Menzies et al., 2008; Nakamae et al., 2014)

suggest that cortical regions may be useful targets for non-invasive neurostimulation via repetitive transcranial magnetic stimulation (rTMS), either through direct cortical effects or modulation of connected subcortical structures. Consistent with this idea, orbitofrontal cortex (OFC) and pre-supplementary motor area (pre-SMA), which are hyperactive in OCD patients (de Wit et al., 2012b; Del Casale et al., 2011; Grützmann et al., 2016; Leckman et al., 2010; Maltby et al., 2005; Yücel et al., 2007), have been identified as promising targets for rTMS (Berlim et al., 2013). Determining how these hyperactive cortical regions interact with the striatum to generate both dysfunctional striatal activity and compulsive behaviors could help refine stimulation patterning for neuromodulatory treatments.

To begin to dissect the contributions of intrinsic striatal vs. extrinsic cortical factors to abnormal OCD-relevant striatal activity, we used an animal model system that displays both striatal hyperactivity and compulsive behavior: Sapap-3-knockout (KO) mice (Burguiere et al., 2013; Welch et al., 2007). Mutations in the *Sapap3* gene, which encodes the synapse-associated protein 90/ postsynaptic density-95-associated protein, have been associated with TS, pathological grooming disorders, and OCD in humans (Bienvenu et al., 2009; Crane et al., 2011; Züchner et al., 2009). *Sapap3*-KOs demonstrate ex vivo abnormalities in striatal spiny projection neurons (SPNs), including both increased NMDA-receptor mediated and reduced AMPA-receptor mediated transmission in dorsal striatum (Ade et al., 2016; Wan et al., 2014; Wan et al., 2011; Welch et al., 2007). Furthermore, consistent with human OCD literature, they also exhibit hyperactivity in central striatum at baseline and during compulsive grooming (Burguiere et al., 2013). This hyperactivity is relieved by stimulation of lateral OFC (LOFC) inputs into central striatum, suggesting dysregulation of LOFC corticostriatal inputs to spiny projection neurons (SPNs) or fast-spiking interneurons (FSIs). However, the contribution of corticostriatal inputs from

M2 to striatal hyperactivity in *Sapap3*-KOs has been unexplored, despite the fact that M2 is the mouse homologue of pre-SMA, a promising treatment target.

To investigate cellular and synaptic abnormalities that could contribute to pathologic striatal hyperactivity and resulting compulsive behaviors, we used acute slice electrophysiology to measure intrinsic excitability of SPNs and FSIs and characterize excitatory cortical inputs to central striatum in *Sapap3*-KOs and wild-type (WT) littermate controls. Although the intrinsic excitability of central striatal neurons was normal in *Sapap3*-KOs, we found substantial differences in functional cortical innervation. While LOFC input to SPNs was weakened in *Sapap3*-KOs, strength and reliability of M2 input to central striatum was substantially increased. These results are the first demonstration of upregulated M2 corticostriatal input in an OCD-relevant mouse model, and highlight the potential role of pre-supplementary/supplementary motor regions in the pathology of compulsivity.

3.2 Materials and Methods

3.2.1 Animals

Male and female *Sapap3*-KOs and wild-type (WT) littermates were maintained on C57/BL6 background and were derived from a colony initially established at MIT by Dr. Guoping Feng. For identification of FSIs, *Sapap3*-heterozygous (*Sapap3*-het) mice were bred with *Sapap3*-het::parvalbumin(PV)-cre mice to generate *Sapap3*-KO and WT littermates that were PV-cre hemizygous (Fig.1). PV-cre mice were derived from a mouse knockin of Cre recombinase directed by the parvalbumin promotor/enhancer (Pvalbtm1(cre)Arbr, Jackson Laboratory, Bar Harbor,

Maine, RRID:IMSR_JAX:017320). Mice were group housed with 2-5 mice per cage and ad libitum access to food and water. Mice underwent stereotaxic surgeries at post-natal day 35-39 or 46-50 (p35-39 or p46-50). All experiments were approved by the Institutional Animal Use and Care Committee at the University of Pittsburgh in compliance with National Institutes of Health guidelines for the care and use of laboratory animals.

Grooming assessments were conducted in a separate cohort of animals that had not undergone stereotaxic surgery, by placing *Sapap3*-KO and WT littermates individually into a 10 inch square plexiglass chamber and video-recording behavior for 20 minutes. Grooming behavior was manually scored offline.

3.2.2 Stereotaxic Surgeries

Stereotaxic surgeries were performed under isofluorane anesthesia (2%). Burr holes were drilled over the target location and virus was injected using either a Nanoject (Drummond Scientific) and glass pulled pipette or a syringe pump (Harvard Scientific) fitted with a syringe (Hamilton) connected to PE10 tubing and a 30 gauge cannula.

Viral injections were performed at p35-39 and allowed to incubate for 3 weeks for optogenetic slice electrophysiology. Channelrhodopsin 2 (AAV2-hsyn-ChR2-eYFP or AAV2-hsyn-ChR2-mCherry, University of North Carolina Vector Core Facility, virus titer 3.1x1012) was injected unilaterally into either lateral orbitofrontal cortex (lOFC) (AP 2.78, ML 1.54, DV 1.65mm; all coordinates from bregma and brain surface) or M2 (AP 2.74, ML 1.54, DV 0.75mm). *Sapap3*::PV-cre mice were injected with cre-dependent AAV5-DIO-mCherry into central striatum (AP 0.65, ML 1.90, DV 3.00 mm) to target PV-positive interneurons.

Fluoro-Gold (FG, 2% in cacodylate buffer; Fluorochrome, Denver, Colorado) iontophoresis was performed in central striatum (AP 0.65, ML 1.90, DV 2.85mm) at p46-50 for retrograde anatomical tracing. Iontophoretic injections were conducted with 5mA of current (7s on, 7s off) for 5-8 minutes. Animals were transcardially perfused 10 days after surgery.

3.2.3 Slice Electrophysiology

Coronal slices containing striatum (300μm) were prepared using a LeicaVT1000S vibratome from brains of 8-week-old mice that had received ChR2 viral injections 3 weeks prior. Brains were sliced for recording with experimenter blind to genotype. Slices were cut in carbogenated HEPES ACSF containing the following (in mM): 20 HEPES, 92 NaCl, 1.2 NaHCO3, 2.5 KCl, 10 MgSO4, 0.5 CaCl2, 30 NaH2PO4, 25 glucose, 5 sodium ascorbate, 2 thiourea, and 3 sodium pyruvate, pH 7.25. Slices were allowed to recover for 15 min at 33°C in a chamber filled with N-methyl-D-glucamine-HEPES recovery solution (in mM): 93 N-methyl-D-glucamine, 2.5 KCl, 1.2 NaH2PO4, 30 NaHCO3, 20 HEPES, 25 glucose, 10 MgSO4, 0.5 CaCl2, 5 sodium ascorbate, 2 thiourea, and 3 sodium pyruvate. Slices were then held at room temperature for at least 1 h before recording in a holding solution that was similar to the HEPES cutting solution but with 1mM MgSO4 and 2mM CaCl2.

Recordings were conducted at 33°C in carbogenated ACSF (in mM) as follows: 125 NaCl, 26 NaHCO3, 1.25 NaH2PO4, 2.5 KCl, 12.5 glucose, 1 MgSO4, and 2 CaCl2. Picrotoxin (50μM) was included in the ACSF to block all striatal local inhibitory activity, and DNQX (6,7-dinitroquinoxaline-2,3-dione) (5μM) was included in the ACSF for intrinsic firing rate data (Fig. 1) and NMDA-mediated current recordings (Fig. 6). For asynchronous release experiments, 2mM CaCl2 was replaced with 2mM SrCl2.

Data were collected with a MultiClamp 700B amplifier (Molecular Devices) and ITC-18 analog-to-digital board (HEKA) using Igor Pro software (Wavemetrics, RRID:SCR_000325) and custom acquisition routines (Recording Artist; Richard C. Gerkin, Phoenix). Current-clamp recordings were filtered at 10kHz and digitized at 40kHz; voltage-clamp recordings were filtered at 2 kHz and digitized at 10kHz. Electrodes were made from borosilicate glass (pipette resistance, 2–6MΩ). The internal solution for voltage-clamp recordings consisted of the following (in mM): 120 CsMeSO3, 15 CsCl, 8 NaCl, 0.5 EGTA, 10 HEPES, 2 Mg-ATP, 0.3 Na-GTP, and 5 QX-314. The internal solution for current-clamp recordings consisted of the following (in mM): 130 KMeSO3, 10 NaCl, 2 MgCl2, 0.16 CaCl2, 0.5 EGTA, 10 HEPES, 2 Mg-ATP, and 0.3 NaGTP.

Electrically-evoked synaptic responses were elicited with 0.1ms current pulses [50ms or 100ms inter-pulse interval (IPI)] passed through a glass stimulating electrode placed in striatum. Optogenetically-evoked synaptic responses were elicited with two 1ms pulses of light (100ms IPI) filtered at 470nm, delivered through the 60x objective of the rig microscope. Maximum responses were obtained by turning the LED to maximum power (1mW). Trials were conducted 20s apart, except for aEPSC trials, which were conducted 12s apart.

3.2.4 Histology

Counts of PV-positive interneurons (FSIs) were conducted by staining 35µm tissue sections containing central striatum with rabbit anti-PV (1:3000, overnight 4°C incubation, Swant, Switzerland, RRID:AB_10000343) and Alexa Fluor 488 anti-rabbit (1:500, 3hr room temperature incubation, AbCam, Massachusetts). Sections were counter-stained with Hoechst (1:1000) to confirm cell bodies. The number of PV-positive cells in a 600µm square region over central striatum was counted and summed across six sections for each animal. Central striatum region was

chosen based on known location of LOFC/M2 projection field overlap, (AP 0.02-0.98mm, ML 1.90mm, DV 2.85mm).

Retrograde tracing experiments were analyzed by quantifying the number of FG labeled cell bodies in regions of the prefrontal cortex (PFC) delineated by the Paxinos Brain Atlas (Paxinos and Franklin, 2004). Sections (35µm) were taken 105µm apart and underwent a nuclear stain before imaging (NeuroTrace Nissl 640/660, ThermoFisher, Massachusetts). Sections containing central striatum (0.85-0.25mm AP) were examined to ensure appropriate targeting and spread of FG before proceeding with cell counting. For each animal, images of PFC sections (4-6 sections per animal, approximately 3.08-2.34mm AP) were imaged using the same parameters (20x magnification, 600ms exposure). To normalize differences in Fluoro-Gold brightness and background in different animals, images were then manually thresholded so that the signal:background ratio were similar across animals. Cells were then automatically detected and counted in each region of interest (Olympus CellSens, RRID:SCR_016238). Proportions of labeled cells in each region were determined by dividing each regional sum by the sum of the total number of cells detected in each animal (ipsilateral and contralateral hemispheres). Proportions were compared between genotype and region using a two-way repeated measures ANOVA and post-hoc contrasts.

3.2.5 Experimental Design and Statistical Analysis

Acute slice electrophysiology experiments were designed to include roughly equal numbers of *Sapap3*-KOs and WTs, taking into account animal availability. Animal and cell numbers for each experiment are reported in the corresponding figure legends. Roughly equal

numbers of male and female mice were used. Recordings were obtained from 2-4 striatal slices per animal. All data were analyzed with genotype blind to the experimenter.

Firing rate (Figure 1) was calculated by counting the number of action potentials evoked with a 500ms current step, and multiplied by 2 to obtain the spikes/second. All synaptic response amplitudes were calculated by finding the average amplitude of evoked EPSCs in five consecutive trials. Strontium asynchronous release events were manually detected within 500ms after the light presentation, and the peak of the event was calculated and averaged over 20-160 events per cell. NMDA-mediated currents were calculated in two ways. First, cells were held at +40mV and the amplitude was found at 60ms after the peak response. The AMPA/NMDA ratio was then calculated by dividing the average AMPA amplitude by the average NMDA amplitude. Second, in DNQX experiments, the peak of the NMDA-mediated current at Vhold = +40mV was calculated and averaged across 5 trials.

Because data were not normally distributed, statistical differences between two groups of values were determined using Wilcoxon Rank Sums Tests (WRST) (Figs. 1, 3-6). To statistically compare input-output curves across multiple stimulation currents (Fig. 2), a two-way repeated measures ANOVA was used because an appropriate non-parametric test could not be found. All values reported are median ± interquartile range (IQR) unless otherwise noted.

3.3 Results

3.3.1 Intrinsic Excitability of Central Striatal Neurons is Not Different in *Sapap3*-KOs and WTs

Hyperactivity in central striatum SPNs has been implicated in the compulsive grooming phenotype observed in *Sapap3*-KOs (Burguiere et al., 2013). Increased SPN activity could result from dysfunction at the level of striatum, including increased SPN intrinsic excitability or reduced FSI inhibitory activity. Because FSIs make up only 1% of the striatal cell population (Berke, 2011; Luk and Sadikot, 2001), we used a transgenic fluorescent strategy to target these neurons using acute slice electrophysiology. PV-Cre transgenic mice were bred with *Sapap3*-KOs to generate *Sapap3*-KO//PV-Cre and *Sapap3*-WT//PV-Cre offspring (Fig. 3.1A). Striatal FSIs were then labeled by injecting the PV-Cre transgenic mice with a cre-dependent fluorescent mCherry virus (Fig. 3.1B). Viral injections were conducted when mice were postnatal day 35-39 (p35-39), and recordings were conducted at p56-p60. At this age, mice exhibit the over-grooming phenotype that is characteristic of the *Sapap3*-KO model (WT mean = 64.17, SEM = 9.01s; KO mean = 204.35, SEM = 23.22s; $t(34) = -5.23$, $p = 8.53\text{x}10\text{-}6$).

We first found that there were no genotype differences in SPN intrinsic excitability, as assessed by firing rate input-output curves (Fig. 3.1C). The slopes of the linear portion of the I-O curve were not significantly different between WTs and KOs (Table 3.1). Additionally, there were no significant differences in other SPN intrinsic properties such as input resistance and resting potential (Table 3.1). This indicates that increased SPN intrinsic excitability does not contribute to in vivo hyperactivity in SPNs.

Hyperactivity in SPNs could also be caused by reduced activity of FSIs, which could stem from either decreased FSI intrinsic excitability or fewer FSIs. However, there were no detectable genotype differences in intrinsic excitability of FSIs as assessed by firing rate input-output curves (Fig. 3.1D), I-O curve linear slope, or any other intrinsic properties (Table 3.1). To investigate whether *Sapap3*-KO mice have fewer FSIs in central striatum, we counted PV-immunoreactive cells in tissue sections from *Sapap3*-KO mice and wild-type (WT) littermates. Summing across six sections for each animal, the number of FSIs was not significantly different in *Sapap3*-KOs and WT littermates ($p = .21$, WRST; Fig 3.1E inset), suggesting that a reduction in the number of FSIs does not contribute to central striatal dysfunction.

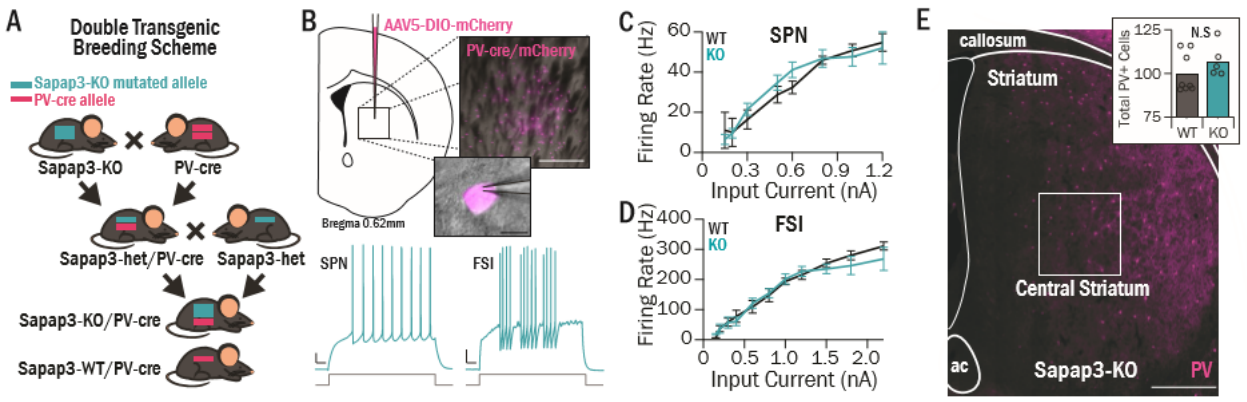

Figure 3.1 Central striatum cell types were interrogated using ex vivo electrophysiology in double transgenic *Sapap3*-KO//PV-cre mice.

(A) Double transgenic mice were generated to investigate functional properties of FSIs. *Sapap3*-KO mice were bred with PV-cre mice to generate mice with one *Sapap3*-KO allele and one PV-cre allele (*Sapap3*-het//PV-Cre). *Sapap3*-het//PV-Cre mice were then used as breeders to generate *Sapap3*-KO//PV-cre and *Sapap3*-WT//PV-cre progeny. (B) (top) AAV5-DIO-mCherry was injected in central striatum; resulting infection of cre-positive PV cells led to fluorescent labeling for targeted slice electrophysiology recordings (inset top: scale bar = 200µm, inset bottom: scale bar = 10µm). (bottom) Examples of evoked spiking traces in KO SPNs and FSIs (right) (scale bars = 50ms, 10mV). (C) No differences were observed between SPN input-output curves in *Sapap3*-KOs (4 animals, 25 cells) and WTs (4 animals, 14 cells). (D) No differences were observed between FSI input-output curves in *Sapap3*-KOs (3 animals, 23 cells) and WTs (5 animals, 18 cells). (E) Tissue sections from *Sapap3*-KO (N=5) and WT (N=8) mice were immunohistochemically stained for PV to perform FSI cell counts in central striatum (box); scale bar = 500µm. (Inset) There was no difference observed in the number of FSIs in WTs vs KOs (ranksum = 44, p = 0.21, WRST).

Table 3.1 Intrinsic properties of FSIs and SPNs in *Sapap3*-KOs and WT littermates.

WT and KO groups were compared using Wilcoxon Rank Sums Test. No significant differences were observed.

IQR: Interquartile range; I-O: input-output.

Median, IQR	FSIs			SPNs		
	WT	KO	*p*	WT	KO	*p*
N (animals, cells)	5,18	3,25		4,14	4,25	
Resting potential (mV)	-76.03, 9.03	-81.17, 9.33	.08	-82.98, 13.67	-86.18, 7.58	.33
Rheobase (pA)	250, 150	300, 150	.79	325, 150	225, 100	.14
Maximum firing rate (Hz)	209, 124	250, 96	.82	50, 9.50	44, 22	.39
I-O curve linear slope	0.64, .64	0.56, .64	.87	0.17, 0.11	0.22, 0.18	.31
Input Resistance (MΩ)	159.12,70.72	184.61, 108.91	.12	299.80, 162.38	298.28,120.76	.70

3.3.2 Excitatory Drive to FSIs in Central Striatum is Increased in *Sapap3*-KOs

Next, we investigated whether the observed hyperactivity of SPNs in *Sapap3*-KO mice (Burguiere et al., 2013) reflected differences in excitatory inputs to central striatum, which could augment SPN activity directly or via decreasing feedforward inhibition mediated by FSIs (Berke, 2011; Gittis et al., 2011b; Gittis et al., 2010; Mallet et al., 2005; Parthasarathy and Graybiel, 1997). To assess excitatory drive onto both FSIs and SPNs, we performed intrastriatal electrical stimulation in acute slices (Fig. 3.2A) and recorded excitatory postsynaptic current responses (EPSCs, Fig. 3.2B,C). Electrical stimulation elicited robust EPSCs whose amplitudes increased with stimulus intensity in both SPNs and FSIs (Fig. 3.2D-E). In SPNs, EPSC amplitudes increased

with similar slopes in WT and KO mice as a function of stimulation intensity ($p = 0.90$, ANOVA; Fig. 3.2D); at a maximum stimulation intensity of 20μA, the average EPSC amplitude was 453pA (SEM 74pA) in WTs and 564pA (SEM 99pA) in KOs ($p = .45$, WRST). By contrast, evoked EPSCs in FSIs were consistently larger in KOs compared to WTs (genotype: $p < .05$; interaction: $p < .05$, ANOVA; Fig. 3.2E); at a maximum stimulus intensity of 20μA, average EPSC amplitude was 422pA (SEM 59pA) in WTs and 857pA (SEM 128pA) in KOs ($p < .01$, WRST). No differences in paired-pulse ratio (PPR) or EPSC decay kinetics were observed in either cell type (Table 3.2).

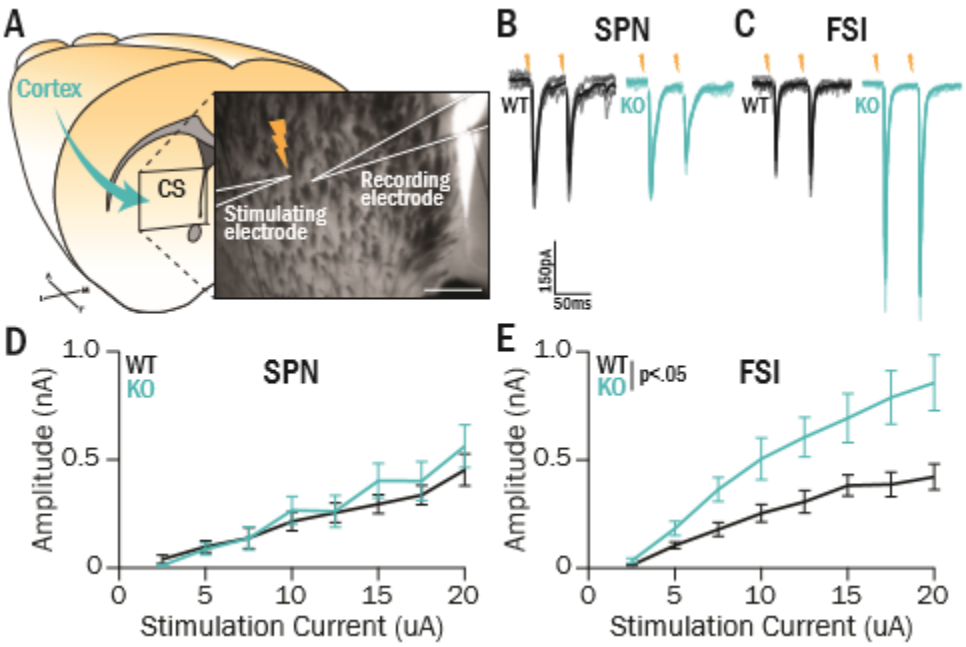

Figure 3.2 Excitatory drive to central striatum FSIs is increased in *Sapap3*-KOs.

(A) Non-specific excitatory inputs from cortex were activated using intrastriatal stimulation while recording nearby cells in central striatum; scale bar = 200µm. (B,C) Synaptic responses were evoked by passing current pulses (0.1ms) through the stimulating electrode during whole-cell recordings of SPNs (B) or FSIs (C) in *Sapap3*-KOs and WT littermates. (D) Evoked response input-output curves in SPNs were not different in KOs vs WTs (WTs = 8 animals, 14 cells; KOs = 6 animals, 12 cells; F(1) = 0.016, p = .90, ANOVA). At maximum stimulation intensity (20µA), EPSC sizes were not different between WTs and KOs (Z = -0.75, p = .45, WRST). (E) Evoked responses in FSIs were significantly greater in KOs relative to WTs (WTs = 6 animals, 13 cells; KOs = 6 animals, 12 cells; genotype F(1) = 8.11, p = .014, interaction F(7) = 4.05, p = .023, ANOVA). At maximum stimulation intensity (20µA), KOs displayed significantly larger EPSCs (ranksum = 57, p = .0057, WRST).

Table 3.2 Paired-pulse ratio and decay constant obtained from all stimulation experiments in *Sapap3*-KOs and WT littermates.

(A) Non-specific excitatory inputs from cortex were activated using intrastriatal stimulation while recording nearby cells in central striatum; scale bar = 200µm. (B,C) Synaptic responses were evoked by passing current pulses (0.1ms) through the stimulating electrode during whole-cell recordings of SPNs (B) or FSIs (C) in *Sapap3*-KOs and WT littermates. (D) Evoked response input-output curves in SPNs were not different in KOs vs WTs (WTs = 8 animals, 14 cells; KOs = 6 animals, 12 cells; F(1) = 0.016, p = .90, ANOVA). At maximum stimulation intensity (20µA), EPSC sizes were not different between WTs and KOs (Z = -0.75, p = .45, WRST). (E) Evoked responses in FSIs were significantly greater in KOs relative to WTs (WTs = 6 animals, 13 cells; KOs = 6 animals, 12 cells; genotype F(1) = 8.11, p = .014, interaction F(7) = 4.05, p = .023, ANOVA). At maximum stimulation intensity (20µA), KOs displayed significantly larger EPSCs (ranksum = 57, p = .0057, WRST).

Median, IQR		FSI			SPN		
		WT	KO	*p*	WT	KO	*p*
Electrical Stim	PPR 50ms	1.24,0.32	1.10,0.17	.83	0.77,0.16	0.86,0.24	.53
	N (animals, cells)	3,8	3,3		5,7	3,6	
	PPR 100ms	0.99,0.25	1.15,0.07	.19	0.84,0.38	0.86,0.18	.95
	N (animals, cells)	3,5	3,9		5,7	3,6	
	Decay constant (ms)	3.77,1.34	3.18,0.94	.07	6.49,1.50	6.19,2.14	.25
	N (animals, cells)	5,12	5,12		8,13	6,12	
LOFC Stim	PPR	0.36,0.23	0.31,0.19	.39	0.27,0.21	0.29,0.11	.90
	N (animals, cells)	10,21	5,10		12,33	5,15	
	Decay constant (ms)	4.17,1.71	4.63,1.61	.29	9.33,5.70	7.10,1.81	.12
	N (animals, cells)	10,19	5,9		12,32	5,10	
M2 Stim	PPR	0.40,0.37	0.43,0.28	.37	0.32,0.11	0.33,0.27	.71
	N (animals, cells)	13,30	7,23		10,21	7,22	
	Decay constant (ms)	4.08,1.72	4.02,2.26	.72	6.70,2.84	6.89,2.71	.95
	N (animals, cells)	11,16	7,22		8,14	7,17	

3.3.3 M2 and LOFC are the Main Sources of Cortical Input to Central Striatum

Our synaptic data indicating that FSIs receive more excitatory drive in *Sapap3*-KO mice was surprising based on a previous in vivo study demonstrating overactive SPNs in KOs (Burguiere et al., 2013). This motivated closer examination of the possible cortical sources of excitatory drive to the central striatum. We therefore iontophoretically infused the retrograde tracer Fluoro-Gold (Fluorochrome) into central striatum of *Sapap3*-KOs and WTs (Fig. 3.3A). To ensure consistency with slice electrophysiology data, mice were sacrificed at p56-p60 after a 10-day incubation period. Only animals with confirmed injection sites in central striatum were used for analysis (Fig. 3.3B). Retrogradely labeled cell bodies were observed in the ipsilateral frontal cortices (Fig. 3.3C), and, to a lesser extent, in the contralateral frontal cortices (data not shown). Although we did not observe a strong laminar pattern, labeled cells were present in Layer V, as anticipated based on past work (Lévesque et al., 1996). To quantify the origins of these cortical-central striatum projections, the number of Fluoro-Gold labeled cells was counted in the five cortical regions where labeling was observed, and the regional proportion of total labeled cells was calculated (Fig. 3.3C-D). In both WT and KO mice, many neurons projecting to central striatum were located in LOFC. However, unexpectedly, the highest proportion of labeled cells was located in the region directly dorsal to LOFC, M2 (Fig. 3.3C). Smaller numbers of neurons were also observed in medial orbitofrontal cortex (MOFC), prelimbic cortex (PL), and dorsolateral orbitofrontal cortex (DLOFC). There were no genotype differences in proportions of retrogradely labeled cells in any of these cortical regions ($p = .10$, ANOVA, Fig. 3.3D).

To further characterize the projections of LOFC and M2 to central striatum, the anterograde virus AAV2-hSyn-ChR2-EYFP was injected into either LOFC or M2 of *Sapap3*-KOs and WTs (Fig. 3.3E). The projection fields in central striatum were qualitatively assessed and their coverage

was mapped onto a representative atlas image (Fig. 3.3F, magenta: M2 projection fields; violet: LOFC projection fields). This assessment highlights that both M2 and LOFC send projections to central striatum, and thus may contribute to corticostriatal dysfunction underlying striatal hyperactivity in *Sapap3*-KOs.

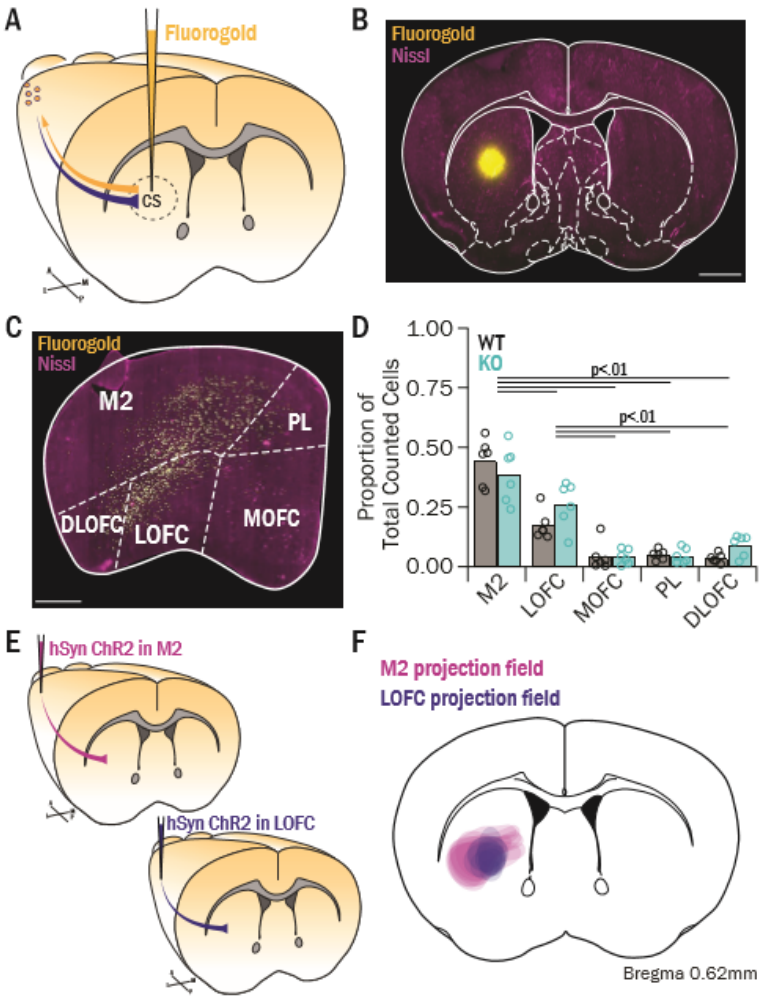

Figure 3.3 Retrograde tracing shows that M2 and LOFC project to central striatum.

(A) Fluoro-Gold was injected into central striatum of *Sapap3*-KO (n = 6) and WT (n = 6) mice to retrogradely label cortical projection cells. (B) Example of a Fluoro-Gold injection into central striatum; scale bar = 1mm. (C) Labeled cortical cells were present throughout frontal cortex in M2, LOFC, MOFC, PL, and DLOFC; scale bar = 500µm. (D) No genotype difference in counted cells was observed ($F(1) = 3.22$, $p = .10$, ANOVA). However, there were differences in the proportions of labeled cells counted across regions ($F(1) = 60.19$, $p = .000$, ANOVA). Ipsilateral M2 showed the highest proportion of labeled cells (WT 44.3 ± 3.9%, KO 38.9 ± 4.8%), which was significantly greater than the proportions in LOFC ($p < .05$), MOFC ($p < .001$), PL ($p < .001$), and DLOFC ($p < .001$, post-hoc contrasts). LOFC contained a significantly higher proportion of labeled cells (WT 17.3 ± 2.4%, KO 26.3 ± 3.9%, $p < .001$) than MOFC (WT 4.2 ± 2.4%, KO 4.1 ± 1.3%, $p < .001$), PL (WT 5.0 ± 0.8%, KO 4.5 ± 1.3%, $p < .001$), and DLOFC (WT 3.5 ± 0.8%, KO 9.0 ± 1.8%; $p < .001$, post-hoc contrasts).

Data are reported as mean ± SEM. (E) AAV2-hSyn-ChR2-EYFP was injected into M2 (5 WTs, 2 KOs) or LOFC (8 WTs, 3 KOs) to map anterograde projection fields in striatum (F) The fluorescence territories of terminals from M2 or LOFC were mapped onto a representative atlas image, demonstrating that M2 and LOFC have partially overlapping inputs in central striatum.

3.3.4 LOFC Input to Central Striatum is Reduced in *Sapap3*-KO SPNs, But Unchanged in FSIs

Based on our anatomical results, we integrated channelrhodopsin (ChR2) into our slice electrophysiology experiments to study region-specific inputs to central striatum. We first focused on LOFC projections, as this region has been implicated in compulsive behavior (Burguiere et al., 2013; Chamberlain et al., 2008; Maltby et al., 2005; Saxena et al., 1998) and related behavioral constructs including action selection, cognitive flexibility, and reversal learning (Dalton et al., 2016; Gremel et al., 2016; Schoenbaum et al., 2002; Sul et al., 2010; Takahashi et al., 2009). To selectively measure the strength of LOFC inputs onto FSIs and SPNs in KOs vs WTs, a pan-neuronal virus (AAV2-hSyn-ChR2-EYFP) was injected into the LOFC of *Sapap3*-KO/PV-Cre or WT/PV-Cre mice and recordings were performed in central striatum after three weeks of virus incubation (p56-60) (Fig. 3.4A,B). LOFC axon terminals in central striatum were stimulated with two brief pulses of light, and evoked EPSCs recorded in FSIs and SPNs were compared between *Sapap3*-KOs and WT littermates (Fig. 3.4C,D). Activation of LOFC terminals evoked large EPSCs in SPNs in WT mice (445pA; IQR = 637pA), but these responses were reduced ~3.2-fold in KOs (138; IQR = 110pA; $p < .001$, WRST; Fig. 3.4F). To address whether the decreased EPSC amplitudes in KO SPNs were due to a decrease in presynaptic release probability, we calculated PPR; no significant differences were observed (Table 3.2), suggesting a postsynaptic effect.

In contrast to our findings in SPNs, WTs and KOs had similar EPSC amplitudes in FSIs following LOFC terminal stimulation. Maximally evoked EPSCs were 563pA (IQR = 662pA) in WT and 510pA (IQR = 681pA) in KOs ($p = .57$, WRST; Fig. 3.4E). These data reveal that LOFC input to central striatum is reduced onto SPNs, but not FSIs, in *Sapap3*-KOs. Given our findings of increased excitatory drive to FSIs using electrical stimulation, as well as no difference in overall excitatory drive to SPNs, these findings in LOFC suggested an alternative source of increased excitatory input to central striatum.

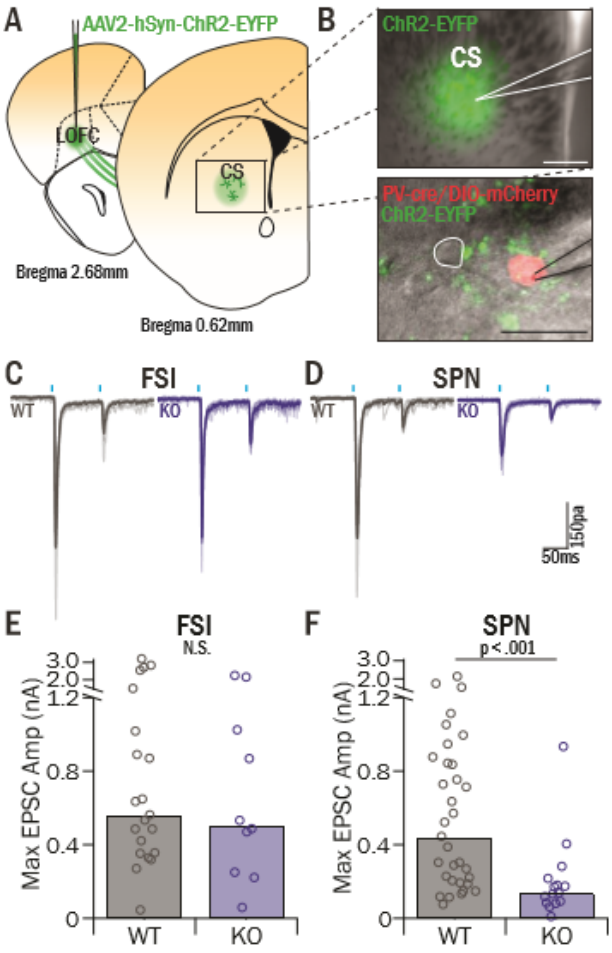

Figure 3.4 LOFC inputs to SPNs have reduced amplitude in *Sapap3*-KOs, while inputs to FSIs are unchanged.

(A) AAV2-hSyn-ChR2-EYFP was injected into LOFC to selectively identify LOFC projections in central striatum. (B) (top) Recordings were targeted to the EYFP-labeled LOFC projection zone in central striatum; scale bar = 200µm. (bottom) Whole-cell patch voltage-clamp recordings (Vhold = -80mv) were conducted in FSIs (identified by the presence of mCherry) and nearby SPNs (white outline); scale bar = 25µm. (C,D) Brief pulses of light (1mW, 10ms pulse, 100ms inter-pulse interval) filtered at 470nm and delivered through the 60x microscope objective evoked synaptic release from ChR2-infected LOFC terminals, and the resulting EPSCs were recorded in FSIs (C) and SPNs (D) and compared between *Sapap3*-KOs and WT littermates. (E) LOFC-evoked EPSCs in FSIs were no different in KOs and WTs (WT: 563.38pA, IQR = 661.69pA, 5 animals, 10 cells; KO: 509.81pA, IQR = 680.86pA, 10 animals, 21 cells; Z = 0.57, p = .57, WRST). (F) SPNs in central striatum

had significantly smaller LOFC-evoked EPSCs in KOs relative to WTs (WT: 444.84pA, IQR = 637.43pA, 12 animals, 33 cells; KO: 137.92pA, IQR = 110.20pA, 3 animals, 15 cells; Z = 3.43, p = 6.14x10-4, WRST).

3.3.5 M2 Input to Central Striatum is Increased in *Sapap3*-KOs

Surprisingly, our anatomical tracing study demonstrated that the largest source of neurons projecting to central striatum was M2, rather than its neighboring cortical area, LOFC. Because M2 is associated with planning of sequenced movements (Cao et al., 2015; Li et al., 2015; Sul et al., 2011) and is thought to be homologous to pre-SMA [which is implicated in OCD (de Wit et al., 2012b; Mantovani et al., 2010)], we investigated whether M2 was a source of upregulated excitatory drive to central striatum in *Sapap3*-KOs (Fig. 3.5A). Using optogenetics and acute slice physiology in WTs, we found that optical stimulation of M2 terminals in central striatum evoked EPSCs in FSIs and SPNs that were much smaller than those evoked by LOFC stimulation (FSIs 84pA, IQR = 158pA; SPNs 43pA, IQR = 136pA; both $p < .0001$, WRST, Fig. 3.5B-E). Furthermore, in a number of cells, EPSCs were either not reliably evoked by each laser pulse, or were not evoked at all. To quantify this, each recorded cell was categorized as having reliability between 100% (5/5 responses) and 0% (0/5 responses). In WT mice, SPNs and FSIs had an average response reliability of 65.4% and 85.9%, respectively (Fig. 3.5F).

In contrast, we found a dramatic increase in the strength of synaptic input from M2 onto both FSIs and SPNs in *Sapap3*-KOs. EPSC amplitudes were increased ~6-fold in SPNs (254pA, IQR = 222pA, $p < .001$) and ~6.6-fold in FSIs (565pA, IQR = 641pA, $p < .0001$, WRST; Fig. 3.5B-E). *Sapap3*-KOs also exhibited increased response reliability relative to WTs in SPNs (100%, $p < .01$, WRST) and FSIs (95.0%, $p = .35$, WRST; Fig. 3.5F). This general increase in synaptic strength was not due to a difference in viral expression levels, because terminal fluorescence in

central striatum was similar across genotypes and we saw no correlation between EPSC amplitude and fluorescence intensity (Fig. 3.5G). Thus, unlike LOFC projections, which exhibited an SPN-specific decrease in *Sapap3*-KOs, M2 projections to central striatum were broadly increased in amplitude and reliability in KOs relative to WTs.

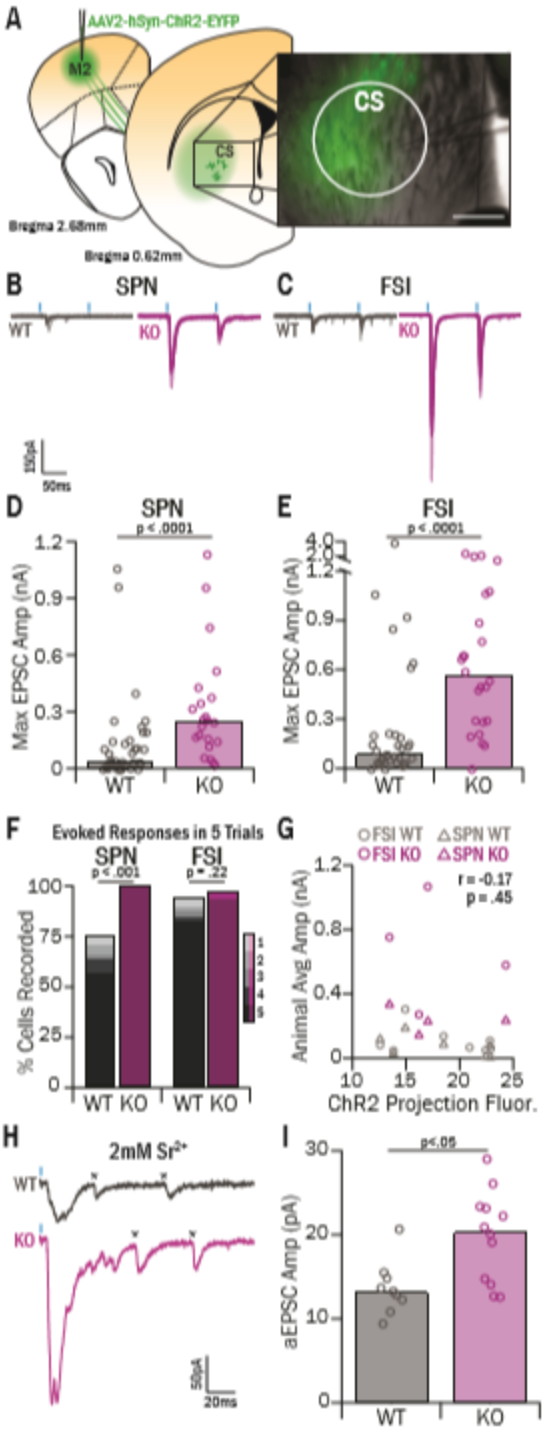

Figure 3.5 M2 input to CS is increased in *Sapap3*-KOs.

(A) AAV2-hSyn-ChR2-EYFP was injected into M2 to selectively label M2 projections in central striatum. Recordings were targeted to the central striatum region, which included the medial portion of the EYFP-labeled M2 projection zone; scale bar = 200µm. (B,C) Brief pulses of 470nm light (1mW, 10ms pulse, 100ms

inter-pulse interval) evoked synaptic release from ChR2-infected M2 terminals, and the resulting EPSCs were recorded in SPNs (B) and FSIs (C) in *Sapap3*-KOs and WT littermates. (D) SPNs in the central striatum of KOs had significantly greater EPSC amplitudes than WTs (WT: 42.58pA, IQR = 136.36pA, 15 animals, 37 cells; KO: 254.28pA, IQR = 221.90pA, 7 animals, 22 cells; Z = -3.87, p 1.11x10-4, WRST). (E) FSIs in central striatum of KOs had significantly greater EPSC amplitudes than WTs (WT: 85.81pA, IQR = 158.33pA, 15 animals, 34 cells; KO: 564.65pA, IQR = 640.84pA, 8 animals, 24 cells; Z = -4.22, p = 2.44x10-5, WRST). (F) Response reliability for each cell was assessed by quantifying the number of optically evoked responses in five trials of stimulation. SPN mean response reliability was significantly increased in KOs relative to WTs (WT 65.41%, SEM = 7.17%; KO 100%; Z = -2.93, p = .0034, WRST). FSI mean response reliability was greater in KOs, but not significantly (WT 85.88%, SEM = 5.31%; KO 95, SEM = 4.21%; Z = -0.93, p = .22, WRST). (G) Average fluorescence intensity of ChR2-infected M2 projections was calculated and correlated with the overall average amplitude of EPSCs recorded in FSIs (10 WTs, 4 KOs) and SPNs (9 WTs, 4 KOs) in a given animal. There was not a significant correlation (r = -0.17, p = .45, Pearson's R). (H) Example traces of strontium asynchronous EPSC (aEPSC) events in WT and KO SPNs. Asterisks denoted detected aEPSC events. (I) SPNs in KO mice showed significantly greater aEPSCs relative to WT mice (WT = 13.25pA, IQR = 2.27pA, 2 mice, 9 cells; KO = 20.48pA, IQR = 8.59pA, 3 mice, 12 cells; Z = -2.38, p = .02, WRST).

3.3.6 Increases in M2 Input to Central Striatum are Driven by Postsynaptic Changes

Upregulation in M2 drive of central striatum responses could reflect abnormalities in M2 cortical presynaptic terminals, or postsynaptic changes in striatal neurons. To evaluate whether presynaptic changes in M2-CS inputs were present, we calculated PPR. No genotype differences in PPR were observed in either FSIs or SPNs (Table 3.2), suggesting a postsynaptic alteration in glutamate receptor number or composition. The decay kinetics of EPSCs were also similar in WTs and KOs (Table 3.2), suggesting no change in subunit composition of AMPA receptors.

To investigate whether strengthened M2-CS synapses were a consequence of a postsynaptic alteration in the number of AMPA receptors, M2-evoked asynchronous EPSCs (aEPSCs) were recorded in SPNs in the presence of 2mM strontium chloride and 0mM calcium chloride (Fig. 3.5H) to measure the strength of quantal release events. aEPSC amplitudes were significantly greater in *Sapap3*-KOs (20.48pA, IQR = 8.59pA) relative to WTs (13.25pA, IQR = 2.27pA, $p < .05$, WRST; Fig. 3.5I), indicating that M2 synapses are strengthened in part by an upregulation in postsynaptic AMPA receptors.

3.3.7 Increases in NMDA-Mediated Currents Are Also Present at M2 Synapses

Sapap3-KO mice have been shown to have alterations in NMDA signaling that can impact synaptic strength, including differential expression of NMDA receptor subunits, increased NMDA-mediated currents in dorsolateral striatum, and reduced AMPA/NMDA ratios in dorsolateral striatum ((Wan et al., 2011; Welch et al., 2007)). We therefore also assessed AMPA/NMDA ratios at M2 synapses in central striatum. AMPA-mediated currents were measured at a holding potential of -80 mV; neurons were then voltage clamped to +40mV to remove the Mg2+ block from NMDA channels and EPSCs were measured again (Fig. 3.6A,B). NMDA currents were estimated by taking the peak EPSC amplitude measured 60ms after onset, a time when the majority of AMPA receptors have closed. In SPNs, AMPA/NMDA ratios were significantly lower in KOs (1.95, IQR =2.22) relative to WTs (4.09, IQR = 4.34, $p < .001$, WRST; Fig. 3.6C). In contrast, there were no detectable differences in the FSI AMPA/NMDA ratio in KOs (11.79, IQR = 14.14) and WTs (16.67, IQR = 14.28, $p = .39$, WRST; Fig. 3.6D).

The fact that AMPA/NMDA ratios were decreased in KO SPNs despite the strong increase in AMPA currents (Fig. 3.5) suggested that NMDA currents are increased even more than AMPA

currents. To better isolate NMDA currents by eliminating the possibility of AMPA current contamination, light-evoked currents were measured at Vhold = +40mV in the presence of DNQX in a separate experiment (Fig. 3.6E,F). Increased NMDA-mediated currents in SPNs were observed in *Sapap3*-KOs (174.77pA, IQR = 268.43pA) relative to WTs (95.99, IQR = 111.69pA, $p < .05$, WRST; Fig. 3.6G). These data are consistent with the idea that SPN NMDA currents are increased proportionately more than AMPA currents in KOs. We observed similar findings in FSIs: KOs had significantly greater NMDA-mediated currents (108.61, IQR = 79.91pA) relative to WTs (27.56, IQR = 75.81pA, $p < .05$, WRST, Fig. 3.6H). To account for the lack of change in FSI AMPA/NMDA ratio, this suggests that, in contrast to SPN findings, AMPA- and NMDA-mediated currents in FSIs are increased similarly in *Sapap3*-KOs. Together, these data suggest that strengthened M2 inputs in central striatum of *Sapap3*-KOs are caused by an increase in both AMPA and NMDA receptor-mediated currents at these synapses.

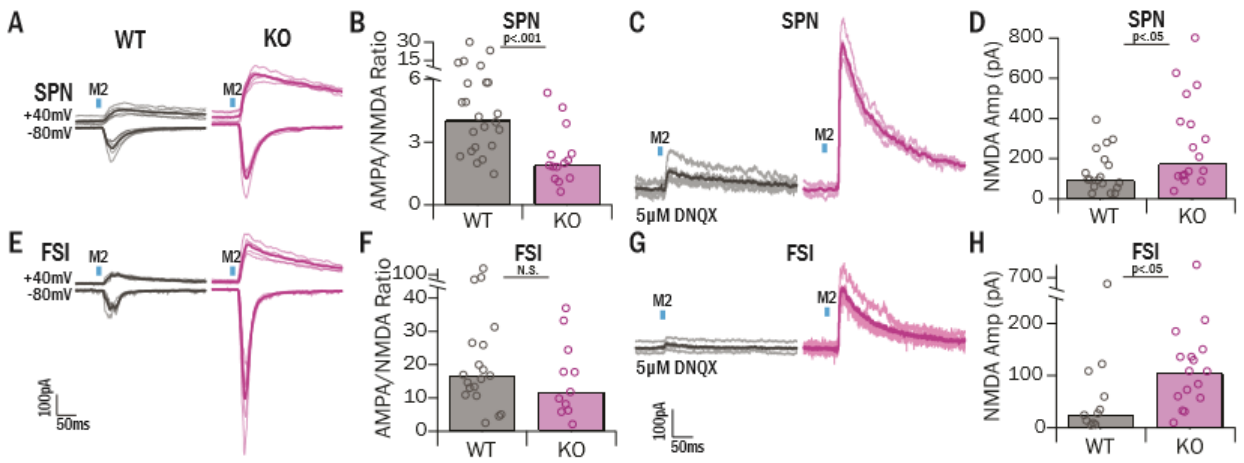

Figure 3.6 Increased M2 input in central striatum is accompanied by increased NMDA currents.

(A,B) After recording M2 light-evoked AMPA-mediated currents at Vhold = -80mV, cells were held at Vhold = +40mV to record NMDA-mediated currents. Amplitude of NMDA-mediated current was measured 60ms after the peak of the response, at which time the AMPA-mediated portion of the current has decayed (gray = WT, pink = KO). (C) AMPA/NMDA ratios in SPNs were significantly lower in KOs relative to WTs (WT 4.09 ± 4.36, KO 1.94, IQR = 2.22; Z = 3.29, p = 9.89x10-4, WRST). (D) AMPA/NMDA ratios were not significantly different between genotypes in FSIs (WT 16.67, IQR = 14.28, KO 11.79, IQR = 14.14; Z = 0.86, p = .39, WRST). (E,F) Examples of isolated NMDA responses with pharmacological block of AMPA receptors with 5uM DNQX (gray = WT, pink = KO). (G) NMDA-mediated currents were significantly greater in SPNs in KO mice (174.77, IQR = 268.43pA, 3 mice, 18 cells) relative to WTs (95.99pA, IQR = 111.69pA, 5 mice, 19 cells; Z = -2.23, p = .02, WRST). (H) NMDA-mediated currents were significantly greater in FSIs in KO mice (108.61pA, IQR = 79.91pA, 3 mice, 16 cells) relative to WT mice (27.56, IQR = 75.81pA, 4 mice, 11 cells; Z = -2.25, p = .02, WRST).

3.4 Discussion

Our data reveal an unexpected contribution of M2 projections to corticostriatal dysfunction in a transgenic mouse model that exhibits OCD-relevant compulsive behavior, *Sapap3*-KOs. We found no abnormalities in intrinsic striatal properties in KOs, but found substantial alteration in

cortical inputs to central striatum. First, we found a reduction of LOFC input specifically onto SPNs, in contrast to predictions that LOFC-SPN input would be upregulated. Even more strikingly, we found that M2 inputs are strengthened by at least ~6-fold onto both SPNs and FSIs in central striatum (Fig.3.7). These results suggest a model in which increased responsiveness of central striatum to input from M2 contributes to the generation of OCD-relevant striatal hyperactivity.

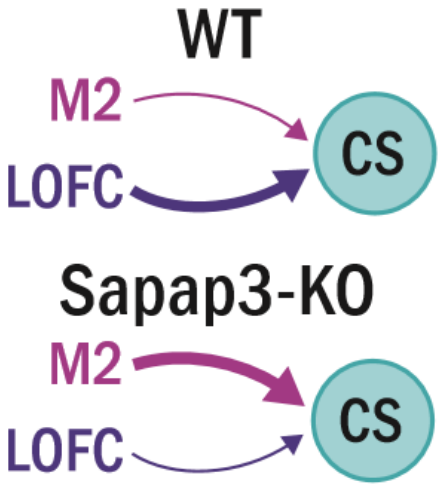

Figure 3.7 Ex vivo synaptic physiology suggests a model of imbalanced cortical input to central striatum. In WT mice, the prominent input to central striatal cells is LOFC, and cells receive weak input from M2. In *Sapap3*-KO mice, the normally strong input from LOFC is reduced, and M2 input substantially increases.

3.4.1 Strengthened M2 Input to CS May Lead to Increased Behavioral Initiations

These findings are the first demonstration of increased strength of M2-striatal circuits in an OCD-relevant mouse model. Similar to SMA/pre-SMA in humans and primates (Isoda and Hikosaka, 2007), M2 in mice is involved in behavioral planning and movement preparation during behavioral selection (Barthas and Kwan, 2017; Cao et al., 2015; Gremel and Costa, 2013a; Guo et al., 2014; Li et al., 2015; Rothwell et al., 2015). Of particular interest, M2-striatal projections have been shown to be critical for initiation of behavioral sequences (Rothwell et al., 2015). Our data indicate that increased strength of M2-central striatum projections in *Sapap3*-KOs includes both increased amplitude and increased reliability of central striatal SPN responses to evoked M2 input. This heightened functional connectivity and increased response reliability could result in striatal neurons that are primed to respond to M2 activity, which in turn could increase the likelihood of initiating specific sequenced behaviors. Previous work has also shown that artificially increasing

M2-dorsal striatum activity via ChR2 after a behavioral sequence was initiated led to decreased completion of the sequence (Rothwell et al., 2015). This evidence supports the hypothesis that abnormally strengthened M2 input to central striatum leads to more initiations and fewer completions of grooming behavior sequences in *Sapap3*-KOs.

3.4.2 Pathological Plasticity May Be Present at M2-CS Synapses

The upregulation of M2 input to central striatum results from increased AMPA and NMDA currents, consistent with other ex vivo observations in striatum of *Sapap3*-KOs (Wan et al., 2011; Welch et al., 2007). Increased NMDA activity at M2 striatal synapses may lead to abnormal corticostriatal plasticity in an already-strengthened projection. For instance, it has been shown that KOs have higher levels of the NR2B subunit in the striatum relative to WTs (Welch et al., 2007), and increased NR2B expression in hippocampus has been associated with enhanced long-term potentiation and heightened learning (Cao et al., 2007; Xu et al., 2009). This suggests pathologically enhanced plasticity mechanisms may be present at M2 corticostriatal synapses, which could contribute to abnormal learning phenotypes (Burguiere et al., 2013) and persistence of compulsive grooming behavior (Welch et al., 2007) observed in *Sapap3*-KOs.

3.4.3 Balanced M2 and LOFC Input to Striatum May Be Necessary for Appropriate Behavioral Selection

Coincident with increased strength and reliability of M2-striatal input in *Sapap3*-KOs, we observed weakened LOFC input to central striatal SPNs that may also play a role in the generation of OCD-relevant compulsive behaviors. Generally, LOFC is known to support functions essential

for flexible selection of behaviors, including reversal learning (Bohn et al., 2003; Schoenbaum et al., 2002; Sul et al., 2010). Consistent with this, Gremel and colleagues (2016) reported that activity in LOFC corticostriatal projections is essential for updating action-value associations (Gremel et al., 2016). These findings suggest that our observed downregulation of LOFC corticostriatal inputs could further bias *Sapap3*-KOs towards decreased flexible action selection and increased compulsivity and/or habit formation.

Taken together, this evidence supports a model in which normally balanced activity of M2 and LOFC is necessary to properly select goal-directed and habitual actions, and strengthened M2 drive and/or reduced LOFC input to central striatum could play a role in generating compulsive grooming behavior in *Sapap3*-KO mice. These findings highlight central striatum as a potential critical node for behavioral selection. We propose that mouse central striatum corresponds to the human caudate head because this region receives input from both LOFC and anterior pre-SMA in humans, but in depth studies by neuroanatomists and in vivo functional assessments in rodents are needed to accurately define the human homologue of central striatum in rodents, including tracing studies in mice, rats, and non-human primates. In *Sapap3*-KO mice, the shift towards M2 motor control and away from LOFC associative control of central striatum may particularly interfere with flexible switching between habitual and goal-directed behaviors, which has been implicated in OCD symptomatology (Gillan and Robbins, 2014). For instance, reduced activity in LOFC corticostriatal terminals is necessary for habit expression, and habit expression is dependent on endocannabinoid-mediated LTD (Gremel et al., 2016); since both phenomena are enhanced in *Sapap3*-KOs (Chen et al., 2011), KOs could display enhanced habit expression.

3.4.4 Identifying the Etiology of Spn Hyperactivity Needs Further Investigation

While the synaptic data presented here describe an intriguing shift to M2-cortical influence over central striatum in *Sapap3*-KOs, our ex vivo data do not directly explain baseline SPN hyperactivity in vivo. However, there are several possibilities for how the described circuit abnormalities may lead to increased SPN firing rates in vivo. While we observed no difference in overall presynaptic excitatory drive to SPNs in KOs vs. WTs, we did observe a substantial increase in M2 reliability. This increased reliability may cause increased drive of SPNs that we cannot capture with ex vivo physiology, especially if M2 itself is hyperactive or hypersynchronous in vivo. In addition, SPN hyperactivity has been described during compulsive grooming as well as at baseline (Burguiere et al., 2013). If M2-central striatum circuits are specifically engaged during sequenced behaviors like grooming, this could lead to behavior-specific generation of larger evoked post-synaptic responses, resulting in striatal hyperactivity. Increased drive to FSIs could also play a role in SPN hyperactivity. While FSIs are canonically thought to strongly inhibit SPN firing (Owen et al., 2018), other reports show that FSI firing can potentiate activity in a subset of SPNs (O'Hare et al., 2017). It has also been suggested that FSIs can tune SPN firing to task-relevant events (Lee et al., 2017; O'Hare et al., 2017; Owen et al., 2018). Increased FSI drive could therefore contribute to enhanced neural activity specifically during performance of sequenced motor behaviors such as grooming in *Sapap3*-KOs. It is important to note that we did not measure FSI-SPN synapses in our study; changes in FSI-SPN synaptic strength in KOs could affect interpretation of our findings. Future studies investigating the in vivo activity of M2 and central striatal SPNs are needed to understand how our observed ex vivo dysfunction leads to compulsive behaviors.

3.4.5 Synaptic Findings Have Implications for Human Treatments

Our findings of increased reliability of M2-central striatum synapses are intriguing in light of functional imaging studies that have identified hyperactivity in pre-SMA in OCD subjects relative to healthy controls (de Wit et al., 2012a; Grützmann et al., 2016; Yücel et al., 2007). In addition, pre-SMA activity has been associated with the "urge" to move in both Tourette Syndrome patients and healthy subjects (Bohlhalter et al., 2006; Neuner et al., 2014). Together with our findings, these studies suggest that hyperactivity in pre-SMA-striatal circuits could promote compulsive behaviors through increased responsiveness of striatal SPNs, and that decreasing pre-SMA activity through low frequency rTMS could be therapeutic. However, it is important to note evidence suggesting that pre-SMA hyperactivity in OCD patients is compensatory, with higher pre-SMA activity correlating with lower YBOCS scores (van Velzen et al., 2014). This would suggest that the appropriate therapeutic intervention would be to use high-frequency rTMS to enhance compensation in OCD subjects whose pre-SMA activity is in the lower range. These discrepancies highlight the fact that the ideal treatment intervention would involve closed-loop technology that could tune neural activity up or down depending on specific context, task requirements, and individuals' symptom levels. However, it is important to cautiously interpret our results with respect to the human OCD literature. While we believe it is critical to further explore the role of M2-striatal circuits in compulsivity using preclinical models, our findings should be translated with caution, and should not be used as the basis for treatment recommendations.

3.4.6 Conclusions

Our data highlight M2-striatal pathology in an OCD-relevant mouse model, and support a novel conceptual model in which *Sapap3*-KO mice display a shift towards increased motor control and decreased associative control over central striatum. In vivo investigations of these circuits will be essential to determine if the observed alterations in synaptic weights result in an imbalance of corticostriatal activity that leads to aberrant behavioral selection, with a bias towards repeating sequenced motor programs associated with compulsive grooming. In addition, these findings support the potential clinical importance of further investigations of pre-SMA/ SMA function in OCD patients. Our data raise the intriguing possibility that pre-SMA is a more important treatment target for decreasing compulsive behaviors in OCD and related disorders than previously suspected.

4.0 Investigation of Relationship Between M2-Central Striatal Circuits and Grooming Behavior

4.1 Introduction

Compulsive behaviors are ritualized, repetitive behaviors that persist despite negative consequences, and are a key feature of Obsessive-Compulsive Disorder (OCD) and related diseases. Compulsive behaviors have been associated with hyperactivity in corticostriatal circuits in human patients (Chamberlain et al., 2009; Del Casale et al., 2011; Denys et al., 2013; Figee et al., 2013; Harrison et al., 2009; Leckman et al., 2010; Maia et al., 2008; Menzies et al., 2008; Rauch et al., 1994; Rauch et al., 1997; Saxena et al., 1998). However, exactly what circuits and synapses are involved in this pathology is unclear.

In the *Sapap3*-KO mouse model of compulsive grooming, corticostriatal abnormalities exist in the central striatum (CS) (Burguiere et al., 2013; Welch et al., 2007, Chapter 3). Specifically, in vivo hyperactivity has been observed at baseline in central striatum, and stimulating lateral orbitofrontal cortical (LOFC) terminals in central striatum relieves that hyperactivity and compulsive grooming behavior (Burguiere et al., 2013). Furthermore, this *in vivo* effect is supported by *ex vivo* work demonstrating that LOFC inputs to central striatum are reduced onto SPNs in *Sapap3*-KO mice (Chapter 3). Importantly, LOFC inputs are not reduced onto FSIs, resulting in enhanced feed-forward inhibitory capabilities by LOFC inputs. This may explain how artificially stimulating LOFC inputs hyperactivated FSIs in central striatum and quieted SPN hyperactivity. Given that this manipulation also reduced grooming behavior, it further suggests that the CS hyperactivity and compulsive grooming may be related.

In support of this relationship, we have observed that CS hyperactivity occurs at the onset of a grooming bout in KOs (Appendix A), in line with human observations that corticostriatal hyperactivity is observed both at baseline and during symptom provocation in OCD patients(Chamberlain et al., 2009; Del Casale et al., 2011; Denys et al., 2013; Figee et al., 2013; Harrison et al., 2009; Leckman et al., 2010; Maia et al., 2008; Menzies et al., 2008; Rauch et al., 1994; Rauch et al., 1997; Saxena et al., 1998). How this hyperactivity plays a role in compulsive grooming is unclear. Potentially, the source of this hyperactivity may be abnormally driving CS to produce grooming behavior. For this to be the case, CS activity must be causal to grooming behavior. This would further support the idea that CS hyperactivity would lead to increased or compulsive grooming behavior.

One unexplored potential source of this effect is M2, which I have demonstrated shows enhanced post-synaptic responses *ex vivo* in CS in *Sapap3*-KOs. These data suggest that excitatory input from M2 may be amplified in CS of KOs, potentially contributing to the observed hyperactivity and compulsive grooming phenotypes. However, it is still unknown how this circuit plays a role in grooming in healthy or abnormal conditions. In support of the idea that M2 may play a role in grooming, it has been shown that stimulating anterior M2 can cause increased licking behavior (Li et al., 2015), which is a key part of grooming. To further investigate how the M2-CS circuit may play a role in grooming and potentially compulsive grooming, we conducted in vivo investigations of M2 and CS activity and the relationship of their activity to grooming behavior.

4.2 Materials and Methods

4.2.1 Animals

Male and female *Sapap3*-KO and wild-type (WT) littermate mice were maintained on a C57/BL6 background and were derived from a colony initially established at MIT by Dr. Guoping Feng. Specific make-up of each cohort is provided in figure legends. Mice were group housed with 2-5 mice per cage except when noted. All mice had ad libitum access to food and water. All experiments were approved by the Institutional Animal Use and Care Committee at the University of Pittsburgh in compliance with National Institutes of Health guidelines for the care and use of laboratory animals.

4.2.2 Stereotaxic Surgeries

Mice underwent stereotaxic surgery between the ages of 4 and 8 months. Stereotaxic surgeries were performed under isofluorane anesthesia (2%). Burr holes were drilled over the target location for subsequent virus injection or implant. Virus was injected using a syringe pump (Harvard Apparatus) fitted with a syringe (Hamilton) connected to PE10 tubing and a 30 gauge cannula and allowed to incubate for at least 3 weeks before experiments.

All recording (electrophysiology, fiber photometry) experiments were conducted using unilateral virus and implants. For electrophysiology recordings, 8 tetrodes were implanted into central striatum (AP .50, ML 1.95, DV 2.85mm; all coordinates from bregma and brain surface). For fiber photometry, AAV9-Synapsin-GCamp6m-WPRE-SV40 (250nL, Addgene) was injected into M2 (AP 2.90, ML 1.55, DV .75mm) and AAV1-syn-NES-jRGECO1a-WPRE-SV40 (500nL,

Addgene) was injected into CS (AP .50, ML 1.95, DV 3.00mm). Optical fibers (NA = .37) were implanted input M2 and CS at the same coordinates but 0.15mm above the injection site.

All behavioral manipulations were conducted with bilateral virus injections and fiber implants into either M2 (AP 2.90, ML 1.55, DV 0.75mm) or CS (AP 0.70, ML 2.00, DV 3.00mm, fibers at 2.60-2.85mm). For M2 terminal stimulation, AAV2-hSyn-ChR2-EYFP (350nL, Addgene) was injected into M2 and fibers were implanted into CS. For CS stimulation, AAV2-hSyn-ChR2-EYFP (500nL, Addgene) and fibers were implanted 0.15-0.40mm above the injection site.

4.2.3 Optogenetic Behavior Manipulations

After 4-6 weeks of virus incubation and recovery, mice were handled for several days prior to behavior experiments. All mice were habituated to the observation chamber and optical fiber tethering for three days prior to behavioral manipulation. On experiment day, mice were scruffed and attached to optical cables and placed in a 10x10inch clear plexiglass observation chamber. A Point Grey camera was fixed beneath the chamber and behavior was filmed from below.

For ChR2 stimulation experiments, 5mW 470nm light was used. Fifty trials of constant light (CS stimulation, 10s trials) or 20Hz light (M2 terminal stimulation, 10ms pulse width, 20s trials) were presented with a pseudorandom inter-trial interval at an average of 30s (25-35s, 5s jitter).

4.2.4 Histology

After experiments were completed, mice were transcardially perfused using 4% paraformaldyhyde (PFA) and post-fixed in PFA for 24 hours. Post-hoc confirmation of viral and implant targeting was conducted on 35um slices from the harvested brains. Slices were mounted with a DAPI coverslipping media and inspected for relevant fluorophores, such as GFP or mCherry for virus or DiI for tetrode tracks. Fiber implants were identified by finding damage tracks in the brain at the specific location.

4.2.5 Experimental Design and Statistical Analyses

Experiments were designed to contain both male and female mice at an age when the *Sapap3*-KOs displayed the overgrooming phenotype. Animals were randomly assigned to experimental or control groups, balancing for sex and cage mates.

Repeated measures ANOVAs with post-hoc contrasts were used to assess differences across time and genotype for fiber photometry activity and behavioral experiments. For behavior, grooming probability in 500ms time bins was analyzed, and for fiber photometry, 1s bins were used.

In vivo extracellularly recorded cells during CS optogenetic stimulation were classified as activated or inhibited by comparing the 5s before and 5s after laser onset and assessing whether average firing rate was significantly different across 50 trials of laser presentation.

4.3 Results

4.3.1 M2 In Vivo Activity is Not Different in *Sapap3*-KOs

Imaging data demonstrates two features of CS activity related to grooming behavior: 1) there is an increase in CS activity at the onset of a grooming bout, and 2) this increase is heightened in *Sapap3*-KO mice relative to WTs (Appendix A). The most likely candidates for drivers of this hyperactivity in KOs are the main cortical inputs to CS: LOFC and M2 (Chapter 3). LOFC input is significantly reduced to CS in KOs, so it is unlikely that increased drive comes from LOFC. However, M2 input to CS is significantly increased in KOs, suggesting that M2 input may be a driver of hyperactivity in CS in KOs.

To determine if M2 inputs are contributing to heightened grooming activity in CS, we first examined whether M2 shows grooming-related activity increases and sends that activity to CS. To investigate this possibility, fiber photometry calcium imaging of M2 and M2 terminals in CS of WTs and KOs was conducted during an observation session of spontaneous grooming. A pan-neuronal calcium indicator virus (AAV9-hSyn-GCamp6m) was injected unilaterally into M2 and an optical fiber was implanted just above the virus injection to record fluorescent calcium activity (Fig. 4.1A). A fiber optic was also implanted in central striatum to observe M2 axon terminal calcium activity. Calcium activity was then aligned to initiations of observed grooming bouts (Fig. 4.1B).

A significant increase in M2 calcium activity was observed at the initiation of a grooming bout (### ; Fig 4.1C). This increase began just prior to the start of a grooming bout and did not differ between KOs and WTs (###). This is consistent with the idea that M2 in mice is similar to a supplementary motor region which shows preparatory activity before a movement (Amador and

Fried, 2004; Lee et al., 1999; Li et al., 2015; Tanji and Mushiake, 1996). Interestingly, M2 did not show a similar activity increase before another discrete behavioral event, rearing (Fig. 4.1D). This suggests that grooming behavior may have a privileged representation in this anterior region of M2 relative to other behaviors.

An increase in calcium activity at the onset of grooming was also observed in M2 terminals in central striatum (Fig. 4.1E), suggesting that this transient increase in M2 activity is propagated to central striatum. Note, the calcium activity between M2 and M2 terminal activity within an animal were highly correlated in both WTs and KOs ($p = .29$, Fig. 4.1B,F). This suggests that our M2 activity profiles are comprised of corticostriatal neurons, consistent with previous evidence showing increases in spike rate at the beginning of a movement, specifically in pyramidal tract cortical neurons (Li et al., 2015).

To further understand how strengthened M2 inputs to central striatum may play a role in increased baseline striatal firing rates in *Sapap3*-KO mice (Burguiere 2013), we recorded M2 baseline activity in vivo. Tetrodes were chronically implanted in anterior M2 in *Sapap3*-KO and WT littermates (Appendix) and spiking activity was recorded for 20 minutes. Baseline firing rates of putative pyramidal neurons were not significantly different in KOs (1.97 ± 0.21Hz) vs WTs (2.07 ± 0.21Hz, $t(91) = p = .75$, Appendix A).

Taken together, these data suggest that M2, the presynaptic side of the M2-CS circuit, is normal in *Sapap3*-KOs relative to WTs. Thus, the observed hyperactivity in central striatum at baseline and during grooming is not due to increased pre-synaptic drive from M2. However, our *ex vivo* work demonstrated a post-synaptic increase in the strength of M2 synapses onto CS cells in KO mice (Chapter 3). This presents the possibility that CS may potentiate normal signals from M2 in KOs, which may lead to the observed hyperactivity.

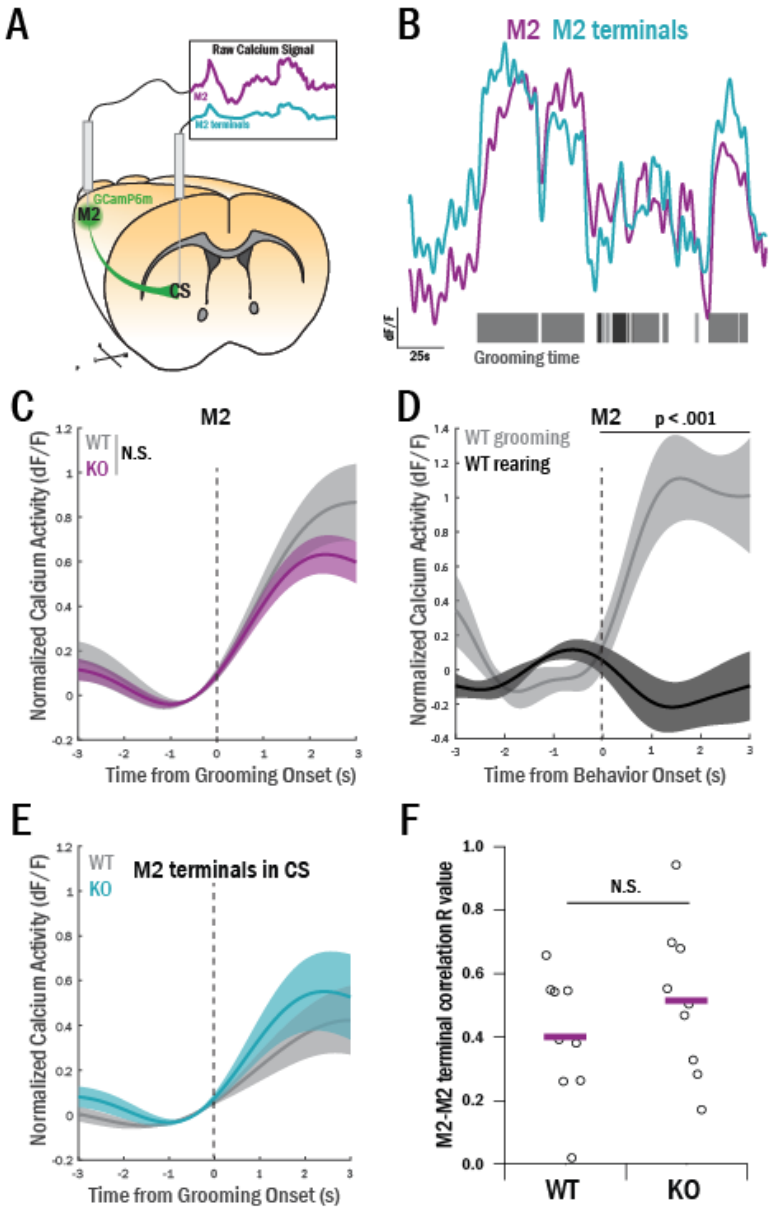

Figure 4.1 M2 sends transient increases in activity at grooming onset to central striatum.

(A) AAV9-hSyn-GCamp6m was injected unilaterally into M2 of *Sapap3*-KO and WT mice. Optical fibers were placed in M2 and CS to record fluctuations in calcium activity. (B) Activity was recorded from M2 and M2 terminals during spontaneous grooming behavior. (C) M2 shows transient increases in activity at the onset of a grooming bout (activity in time bin -1:0s less than activity in time bins -3:-2s ($p < .05$) and 0:3s ($p < .001$)). No genotype difference was present, $F(1) = .175$, $p = .679$). (D) In a subset of WT mice, M2 activity at the onset of rearing was compared to that at the onset of grooming. There was a significant interaction of time and behavior type, $F(1) = 18.49$, $p = .001$, such that activity in time bin 0:3s was significantly different

between grooming and rearing. (E) Calcium activity in M2 terminals in CS also shows a significant increase at the onset of grooming, with time bin -1:0s being significantly lower than time bins 0:3s, $F(1) > 11$, $p < .01$. No significant genotype differences were observed. (F) Correlations of activity between M2 and M2 terminals within an animal shows that M2 and terminals in CS are significantly correlated in every case, with no significant difference between genotypes.

4.3.2 Optogenetic Manipulation of Central Striatum Produces Immediate-Onset Grooming Related Movements

To investigate whether CS hyperactivity is causal to grooming behavior, we bilaterally activated CS cells using ChR2 (Fig 4.2A,B). Stimulation was conducted using 10s constant light (473nm) pulses over 50 trials (Fig. 4.2C). Stimulation of central striatum resulted in partial grooming-related movements, such as turning towards the flank as if to groom the body and raising paws up to the face as if to groom the face. The observed behaviors were stereotyped within a mouse, with each responsive mouse conducting the same movement for every affected stimulation trial. These partial grooming movements were evoked immediately when the light was presented and lasted for roughly ~5s, or half of the stimulation period. To quantify how reliable this behavioral effect was, probability of grooming or grooming-related movements was calculated across all 50 trials of stimulation (Fig. 4.2D). Probability of grooming was significantly increased at the onset of the laser pulse in ChR2 animals but not in EYFP control animals ($p < .05$).

To further understand the dynamics of this behavioral response, *in vivo* electrophysiological recordings were conducted while CS was stimulated via ChR2. We observed that awake, behaving in vivo optogenetic stimulation of CS cells caused an immediate population spike across all tetrodes, suggesting a transient increase in synchronous activity at the beginning of the pulse (Fig. 4.2E). Following the population spike, we observed two different types of

responses in recorded responsive neurons (note: 53% of the neurons were not affected by light stimulation). Of the neurons that did show a response to light, 28% showed an increase in activity and 72% showed a reduction in activity (Fig. 4.2F, right). In addition, neurons tended to show a difference in activity in the first 5s of the pulse relative to the last 5s. Neurons that increased their response showed a ramping of activity up to ~3-4s, then a ramping down in activity for the latter half of the pulse (Fig. 4.2F, top). In contrast, many neurons which decreased activity showed a sharp reduction in activity after the population spike, and remained low in firing rate for the first 5s, then started to increase activity in the second half of the stimulation (Fig. 4.2F, bottom).

Taken together, these data suggest that there is a complex pattern of inhibition and excitation in central striatum that is driving the initiation of grooming related movements. This is in line with data showing that striatal cells have varying dynamics of activity around the onset of behavioral syllables (Markowitz et al., 2018). Furthermore, because activity in striatum due to this stimulation changes around 3-4s post laser onset (Fig. 4.2F), which matches the temporal dynamics of the behavioral response (Fig. 4.2D), these data may also suggest that activity dynamics in striatum play a role in the cessation of grooming behavior. For instance, activation of specific ensembles in striatum (i.e. synchronous population spikes and initial inhibition/excitation profile) may be responsible for the start of grooming, while a secondary response profile (i.e. cells change their stimulation response after a few seconds) may play a role in stopping the grooming behavior.

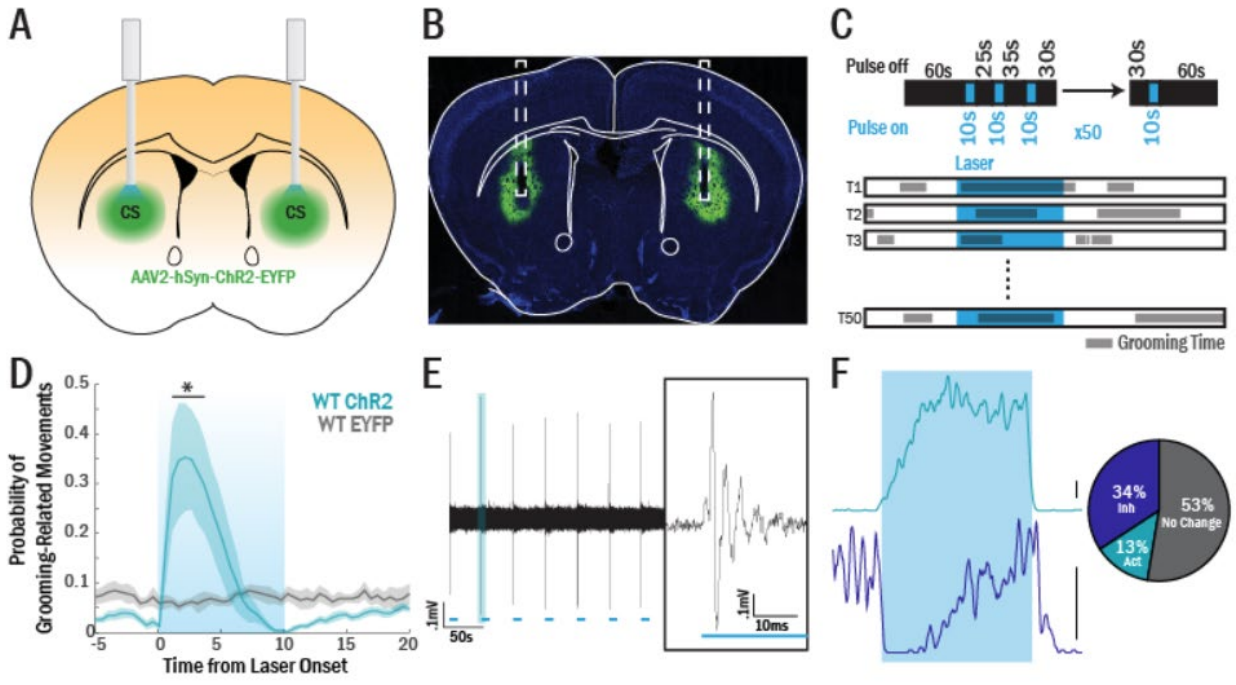

Figure 4.2 Central striatal stimulation evokes a heterogeneous response of inhibition and excitation and causes grooming movements.

(A,B) AAV2-hSyn-ChR2-EYFP or EYFP control virus was bilaterally injected into central striatum of *Sapap3* WT littermates. (C) A "random stimulation" paradigm was utilized in which 10s pulses of constant light stimulation were presented in 50 trials, with a 25-35s intertrial interval (5s jitter). Grooming time was then quantified and probability of grooming was assessed across 50 trials. (D) Probability of grooming was significantly greater in ChR2 animals (N=9) relative to EYFP animals (N=6) (time bins 1:3.5s, all $p < .01$). (E) In vivo electrophysiology (unilateral) in a separate set of animals demonstrates that the stimulation paradigm causes initial population spikes, transiently synchronizing the entire CS population. (F) Following population spikes, some cells (13% of all cells) showed a ramping up in activity over the first 3-5s of stimulation (top), while other cells (34% of all cells) showed inhibition in this initial period followed by a ramping up of activity back to baseline (bottom).

4.3.3 Optogenetic Stimulation of M2 Terminals in CS Evokes Grooming in WTs with Long Temporal Onset

Because evidence suggests that M2 input to CS is strengthened on the post-synaptic side of the synapse, we investigated whether stimulating M2 synapses in CS could generate these increased post-synaptic responses and evoke grooming behavior. Given that KO mice show strengthened M2-CS projections, CS is involved in grooming, and the KOs compulsively groom, it follows that CS cells receiving M2 input may be grooming-related. In WT mice, though weaker, M2 projections may also contact grooming-related CS cells, so artificially stimulating them in WT mice should recapitulate a grooming behavior. To investigate this question, bilateral injections of AAV2-hSyn-ChR2-EYFP (or EYFP control) were conducted in M2, and fiber optics were implanted in CS. To increase the power of our analyses, we designed a "random stimulation" paradigm where 20 trials of 20s pulses of constant 470nm light were presented with a pseudorandom inter-trial interval (25-35s with a 5s jitter). This paradigm prevents the animal from being able to predict the stimulation periods and provides many trials of light over which we can investigate light-evoked activity. Light was delivered at a 20Hz frequency (10ms pulse width) to better mimic naturalistic cortical activity (Riehle et al., 1997).

Experiments were run at a range of powers of 10mW, 7mW, and 5mW to titrate laser power for each mouse, paying careful attention to minimize possible seizure or pre-seizure activity due to antidromic activation of M2 cortical cells. After observing and quantifying grooming behavior, we observed a non-significant increase in the average grooming probability of ChR2 mice. Upon closer inspection of individual animals' responses, it became clear that there was a set of six "responder" mice which showed an increase in probability of grooming during the 473nm light presentation. In contrast, the remaining nine ChR2 mice did not show an increase in grooming

during light presentation, but sometimes showed stereotypies or behavioral arrest. This heterogeneity suggested possible differences in viral spread or fiber optic placement in these mice that could affect the extent or intensity of projection stimulation and antidromic activation in cortex; histological investigations of these mice's brain tissue are currently underway. Potentially, post-synaptic activation of CS and antidromic activation of M2 may cause competing behavioral effects, such as grooming and seizure/behavioral arrest.

In responder mice, the grooming effects were consistently delayed relative to laser onset (Fig. 4.3C). This delay in behavioral effect could be due to low recruitment of post-synaptic CS cells until there is a sufficient activation to cause grooming initiation. Consistent with this idea, nVoke single-cell calcium imaging in CS with optogenetic stimulation of M2 terminals shows that CS cells are not all activated at the onset of a 20s laser pulse (Appendix A). Rather, many cells are activated only after 5-15s after the onset of the laser, and remain elevated in activity after the laser is turned off. The dynamics of activation in the significantly activated cells match the dynamics of the behavioral response (Appendix A).

An additional prediction about this circuit is that the M2 synapses in CS are stronger in *Sapap3*-KOs and will therefore more reliably evoke a response in CS. To begin to investigate this hypothesis, a small pilot group of 4 KO mice were run in an identical experiment. Of these mice, 2 showed a robust grooming response (Fig. 4.3D). When comparing WT and KO responder mice, we observed a significantly greater likelihood of grooming in the KO mice relative to the WTs during the laser pulse (Fig. 4.3D). These data support the prediction that M2 synapses more reliably activate CS and cause grooming behaviors in *Sapap3*-KOs.

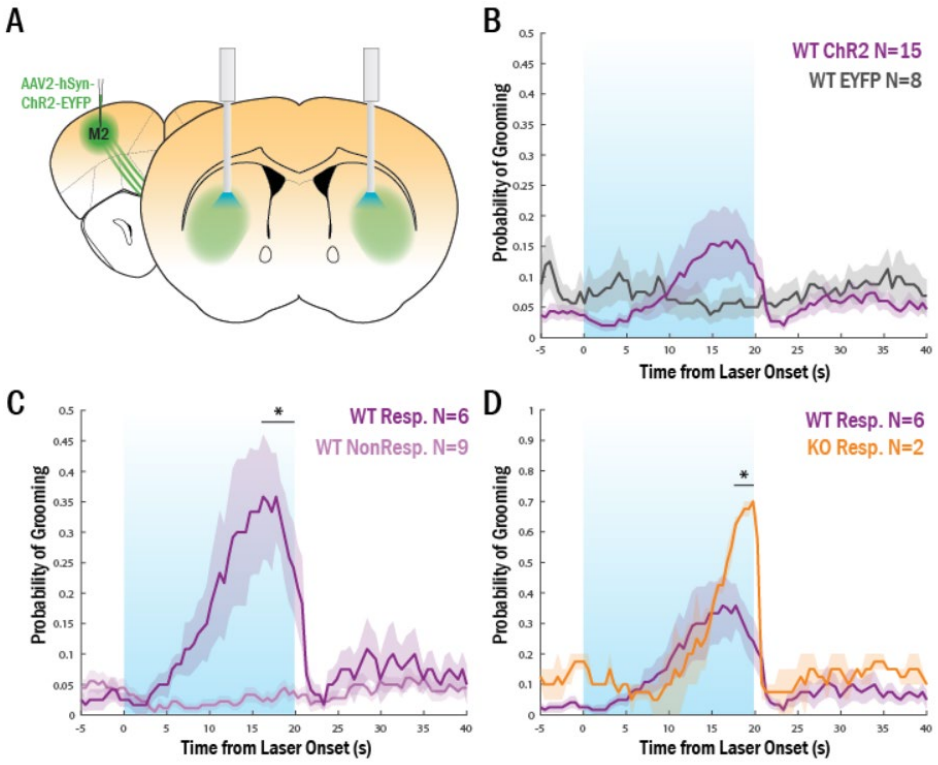

Figure 4.3 M2 terminal stimulation in CS evokes grooming more reliably in KOs relative to WTs. **(A) AAV2-hSyn-ChR2-EYFP or EYFP control virus was bilaterally injected into *Sapap3* WT littermates and optical fibers were bilaterally implanted in CS. (B) During 20 trials of 20Hz 20s pulses of 473nm light presentation, ChR2 animals (N=15) showed a slight but non-significant increase in grooming probability relative to EYFP animals (N=8). (C) A closer inspection of the individual animal responses revealed that a subset of mice were responding to the light with a grooming response (WT Responders, N=6) significantly more than WT Non-Responders (N=9; time bins 10.5:20s, all $p < .05$). (D) In a small group of pilot *Sapap3*-KO mice (N=4), an identical experiment was conducted. KO Responders (N=2) showed significantly higher likelihood of grooming during light presentation relative to WT Responders (time bins 18.5:20s, all $p < .05$).**

4.4 Discussion

The data presented here demonstrate a role for M2-CS circuitry in compulsive grooming behavior. We propose a model in which post-synaptic strengthening of M2 synapses in CS may play a role in heightened grooming behavior in the *Sapap3*-KO mice. We demonstrate that anterior M2 and its terminals in CS show grooming-specific increases in activity, which *ex vivo* work suggests would lead to potentiated responses in CS of *Sapap3*-KOs. To replicate this activation of CS, we show that direct stimulation of CS cells in the region downstream of M2 can cause immediate-onset partial grooming movements. The neuronal activity underlying this stimulation is heterogeneous and dominated by brief population synchrony followed by a period of inhibition, which suggests that specific dynamics of excitation and inhibition in CS may be important for generating grooming movements. To understand how M2 cortical input may play a role in this grooming behavior, we optogenetically stimulated M2-CS synapses and observed that, in contrast to striatal stimulation, grooming behavior was evoked less reliably and at a longer latency after stimulation. Furthermore, preliminary evidence suggests that M2 terminal stimulation evokes grooming more reliably in *Sapap3*-KO mice, supporting the idea that strengthened M2 synapses leads to more readily activated CS cells in KO mice.

4.4.1 Central Striatal Amplification of M2 Cortical Signal in *Sapap3*-KOs

These data support the hypothesis that M2 inputs are amplified in central striatum. Previous reports have demonstrated increased synaptic strength ex vivo at these synapses, and shown that this effect is driven at least in part by a post-synaptic mechanism, such as increases in AMPA receptors at the synaptic cleft (Chapter 3). Here we demonstrate that, *in vivo*, M2 input activity

during grooming onset is normal in *Sapap3*-KOs relative to WTs, but that KOs display a greater CS grooming-related activation. Additionally, M2-CS terminal stimulation more reliably evokes grooming in KOs relative to WTs, suggesting that this projection is more readily activated in KOs.

The fact that activity at the level of M2 is normal suggests that M2 is not the site of compulsivity in these mice. Rather, compulsive behavior may involve specifically the M2 synapses and post-synaptic cells in CS. The amplification of this signal is likely propagated throughout the basal ganglia and downstream motor structures, eventually leading to increased grooming behavior. These data highlight the important role that striatum, and specifically central striatum, plays in the selection and initiation of behavioral plans. If movement initiation signals initiate in cortex instead, we may have predicted abnormalities in M2 at grooming onset in KOs. Rather, our data suggest that, while grooming initiation signals may occur in M2, they are not consistently transferred to striatum in WTs and their transference to striatum is necessary for actual initiation of grooming behavior. Thus, it seems more likely that a true initiation signal for grooming behavior is generated in striatum. The idea that behavioral selection and initiation is mediated through striatum is supported by existing work showing that striatal manipulations can affect what trained behaviors are selected and how quickly they are initiated (Brown and Robbins, 1989), as well as recordings showing that striatal activity is associated with flexible decision making (Kimchi and Laubach, 2009). Furthermore, activity in both dSPNs and iSPNs is present at the initiation of many behaviors (Markowitz et al., 2018), consistent with our data that stimulating striatal cells can lead to the initiation of grooming-related movements.

4.4.2 Central Striatal Ensembles and Behavior

Imaging data suggests that central striatal grooming ensembles are larger in KOs. These ensembles are made up largely of activated cells, but also include inhibited cells (Fig. 4.2F). Optogenetic stimulation of CS cells causes an initial hyperactivation followed by a mix of excitation and inhibition. This paradigm also causes grooming-related movements, but not normal grooming sequences. Interestingly, the proportions of activated and inhibited cells in the calcium imaging data are different than the proportions in the optogenetic stimulation data. This suggests that our stimulation paradigm is likely not evoking the proper balance of activation and inhibition in the ensemble, which may explain why the movements produced are not naturalistic grooming behaviors. Another possibility as to why CS stimulation doesn't cause normal grooming is that our blunt, unnaturalistic stimulation is activating only sub-parts of normal behavioral ensembles in striatum, causing partial, interrupted movements. In normal circumstances, there are likely specific ensembles of cells that need to be activated and inhibited in a stereotyped way in order to produce normal movements.

The cellular make-up of these ensembles is not specified in our data. Thus, grooming-related ensembles of cells likely involve direct and indirect pathway SPNs (dSPNs, iSPNs) as well as interneurons. Previous findings have demonstrated that both dSPNs and iSPNs are involved in cellular ensembles (Barbera et al., 2016; Parker et al., 2018), supporting the prediction that both cell types are involved in the ensembles reported here. Traditional ideas about the striatum predict that dSPNs are movement promoting and iSPNs are movement inhibiting, which would suggest that hyperactivity specifically in dSPNs are the underlying cause of compulsive grooming. However, more recent data has shown that both dSPNs and iSPNs are concurrently active at the beginning of a movement (Cui et al., 2013; Meng et al., 2018), and there can be different patterns

of activation/inhibition for different types of movements (Markowitz et al., 2018). Therefore, we posit that the cell ensembles examined here include both dSPNs and iSPNs, which are activated and inhibited in a manner that is specific to grooming behavior. Further investigations using double transgenic *Sapap3*-KOs and WT littermates will be necessary to conclusively answer this question.

4.4.3 Grooming Initiation and Cessation in M2-CS Circuit

Direct stimulation of CS cells evoked stereotyped, partial grooming-related movements instantaneously, suggesting that there may be representations of pieces of movements in CS. This idea is consistent with previous reports showing that motor tics can be evoked via disinhibition in the central striatum (Bronfeld et al., 2013; Pogorelov et al., 2015).

In contrast, when M2 cortical terminals in central striatum were stimulated, full sequences of grooming behavior were produced. This further suggests that cortical inputs may relay full motor programs to striatum, consistent with previous thoughts (Nachev et al., 2008; Nakayama et al., 2008; Shima et al., 1996; Tanji and Shima, 1994). These data set up a model where full motor commands are activated in M2 cortex, and these inputs activate several different ensembles in central striatum. By bluntly stimulating central striatal cells, it is likely we were activating only certain ensembles related to the stereotyped partial grooming-related movements we observed, or even inhibiting some cells of relevant CS ensembles. However, when a more naturalistic activation of the central striatum was conducted, via activation of M2 cortical inputs to central striatum, more complete and complex CS ensembles (i.e. patterns of activation and inhibition) were potentially activated so that full grooming sequences were evoked.

4.4.4 Compulsive Grooming and the M2-CS Circuit

In both WTs and KOs, we observed an increase in M2 and CS activity at the beginning of a grooming bout, though this striatal increase was significantly greater in KO mice. How exactly the magnitude of CS activity relates to compulsivity of grooming is unclear, though one potential explanation is that greater activity at grooming initiation leads to longer grooming bouts. This type of process could be related to persistent activity in an ensemble, and how these persistent activity patterns underlie the cognitive processes of working memory and decision making (Curtis and Lee, 2010). Further, we have shown that a grooming bout can be evoked via stimulation of the M2-CS terminals, and that this paradigm more reliably evokes grooming in KOs relative to WTs. This suggests that these synapses may more reliably lead to CS activity in KOs. Potentially, this input from M2 acts as an "activation signal", and stronger synapses in KOs allow this signal to be passed to CS more reliably.

It remains unclear what causes the increased initiations of grooming behavior in the *Sapap3*-KOs. One possibility is an increase in the frequency of "movement initiation" signals. While these signals to initiate grooming bouts may be originating in M2, the fact that our stimulation of M2 terminals produced grooming at such a long latency suggests that the first initiation signal may be coming from somewhere else in the cortico-basal ganglia circuit. Because central striatal stimulation produced instantaneous grooming movements, we hypothesize that the grooming initiation signals arise either in central striatum directly or from another monosynaptic connection to striatum, such as thalamostriatal projections or corticostriatal projections from another cortical source.

Given that central striatal cells are relatively silent without an outside source of excitatory input (Gertler et al., 2008; Gittis et al., 2010), it may seem unlikely that a movement initiation

signal could arise de novo in CS. However, it is possible that there is some mechanism of disinhibition in striatum that allows SPNs to spike even in the absence of an excitatory initiation signal. For instance, GPe has the capability to strongly inhibit FSIs in striatum, which would cause a disinhibition of SPNs (Chapter 2). Given the right conditions, GPe inhibition may transiently silence FSIs and allowing SPNs a window in which to produce movement initiation signal. Furthermore, SPNs are known to exhibit hyperpolarized downstates interspersed with depolarized upstates. While these upstates are thought to be stimulated in part by cortical inputs (Plotkin et al., 2011), it has been theorized that GPe-FSI connections could be responsible for SPN upstates (Wilson, 2009). Instead, varying upstates evoked by cortex may coincide with GPe inhibition of FSIs, producing circuit and behavioral conditions that are permissive for movement initiation. In this way, central striatum itself may be the site of grooming initiation signals.

4.4.5 Conclusions and Implications

Taken together, these data propose a novel post-synaptic amplification of M2 cortical signals in central striatum that plays a role in compulsive grooming behavior in *Sapap3*-KO mice. These findings highlight the need to further investigate the role of this understudied striatal region in the generation of compulsive behaviors and related behavioral phenomenon like tics and other repetitive behaviors. It is still unclear how this central striatal region in mice maps on to striatal regions in the human. We propose defining the homologous central striatal area via overlapping projections from LOFC and pre-SMA/SMA (McFarland and Haber, 2000; Selemon and Goldman-Rakic, 1985). Moving forward, it will be essential to investigate these regions in patients who exhibit compulsive behaviors so that we can further understand how to address and treat this pathology.

5.0 CONCLUSIONS AND DISCUSSION

5.1 Summary

5.1.1 Strong GPe-FSI Connection Can Control Striatal Output

In Chapter 2 I described data showing a strong functional connection from GPe to striatal FSIs. Using computational modeling, it was demonstrated that this GPe-FSI connection has the capacity to strongly control striatal output through SPNs, particularly when FSIs increase their connections to SPNs in dopamine depletion (DD) conditions. Specifically, I showed that in DD, this strong loop formed between iSPNs, GPe, and FSIs has the capability of propagating synchronous oscillatory activity. Given that FSIs and iSPNs also interact with dSPNs, even though they were not in our model, presumably this GPe control over FSIs would extend at least partially to dSPNs, as well.

Though our model focused on the effects of circuit reorganization in DD, the GPe-FSI connection may also play an important role in striatal output in healthy conditions. Under normal conditions, GPe is spontaneously and tonically active (Bevan et al., 2002). This suggests that GPe may be tonically inhibiting FSIs and preventing them from regulating SPNs. However, a synchronous pause in GPe activity (for instance, between bursts of spiking) would provide a brake in the inhibition of FSIs, allowing them a brief period of inhibitory regulation over SPNs. This profile of activity of a GPe population decrease coincident with an FSI population increase has been reported during the choice point in a T-maze task (Gage et al., 2010). In contrast, a transient increase in GPe activity (i.e., a burst) would cause a stronger inhibition of FSI firing and therefore

a window of time for SPNs to fire. For instance, a mechanism like this may occur at movement initiation, which has been associated with both GPe activation and SPN activation (Anderson and Horak, 1985; Gritton et al., 2019; Jin et al., 2014).

Exactly how this projection plays a role in behavior is largely speculation, but much can be learned from abnormal behavioral conditions. In Parkinson's Disease and DD, GPe has been shown to have an increase in synchronous and bursting activity (Bevan et al., 2002). These synchronous bursts would theoretically cause alternating periods of strong inhibition and disinhibition of FSIs, which may disrupt normal inhibitory regulation in striatal processing. This disruption of striatal computational power could interfere with the ability to select behaviors, which may relate to akinesia associated with DD (Johnston et al., 1999). In contrast, tonic inhibition of GABA signaling in GPe would cause an increase in GPe activity, which would inhibit FSIs and disinhibit SPNs. Indeed, infusion of a $GABA_A$ blocker into GPe in primates elicits abnormal movements and/or stereotypies (Grabli et al., 2004), which may be in part due to disinhibition of striatal activity.

5.1.2 Post-Synaptic Strengthening of M2 Synapses in Central Striatal SPNs and FSIs

Chapter 3 highlighted central striatum and its potential role in corticostriatal abnormalities in the *Sapap3*-KO mouse model of compulsive behavior. Retrograde anatomical tracing showed that M2 and LOFC are the major cortical inputs to central striatum (CS). This suggests that CS may serve to integrate motor planning information from M2 and outcome value information from LOFC to play an important role in behavioral selection. However, *ex vivo* electrophysiology demonstrated that under normal conditions, M2 synapses in CS are relatively weak and unreliable. In contrast, synapses from LOFC are prominent. This suggests that CS may, in WTs, be driven

largely by LOFC inputs, which have been shown to be important for behavioral flexibility and value updating (Bohn et al., 2003; Gremel et al., 2016; Schoenbaum et al., 2002; Sul et al., 2010).

In *Sapap3*-KO mice, LOFC synapses were significantly reduced in strength onto SPNs, while LOFC synapse strength in FSIs did not change. This suggests that, in response to an equivalent LOFC input, SPNs in *Sapap3*-KOs would experience greater evoked feedforward inhibition from FSIs relative to WTs. These data may explain the findings from Burguiere and colleagues that hyper-stimulation of LOFC projections in central striatum activates FSIs, reduces SPN hyperactivity, and normalizes grooming behavior (Burguiere et al., 2013). These findings all suggest that CS may be receiving less information from LOFC about outcome value, and therefore may cause decreased behavioral flexibility in *Sapap3*-KOs.

In contrast, in *Sapap3*-KO mice, there is a post-synaptic strengthening of the M2 synapses onto both SPNs and FSIs in CS. In addition, I found that more SPNs received reliable input from M2 in the *Sapap3*-KOs relative to WTs, which suggests a potential presynaptic strengthening of this projection as well. These data suggest that there may be increased pre-supplementary/supplementary motor control over CS-mediated behavioral selection in KOs, in line with M2's role in movement preparation and planning (Barthas and Kwan, 2017; Cao et al., 2015; Gremel and Costa, 2013a; Guo et al., 2014; Li et al., 2015; Rothwell et al., 2015). This heightened M2 input may also play a role in the observed central striatal hyperactivity at baseline and during grooming behavior.

5.1.3 Heightened Information Transfer from M2 to Central Striatum is Related to Compulsive Grooming

In the final chapter, I demonstrate the involvement of the M2-CS circuit in grooming behavior using fiber photometry and optogenetic behavioral experiments. While M2 grooming-related increases in activity are similar in WTs and KOs, central striatal grooming-related increases are heightened in *Sapap3*-KOs. These data suggest that central striatum amplifies M2 grooming-related inputs in KOs, likely due to a post-synaptic increase in synaptic strength (Chapter 3).

The observed CS hyperactivity in KOs is due to an increased number of grooming-activated cells (Appendix A), suggesting an increase in the cellular ensemble related to grooming behavior. The size of "grooming ensembles" in CS may therefore be heightened in KOs, such that more of the striatum is devoted to grooming related behaviors. *Ex vivo* data shows that more CS cells receive M2 input in KOs relative to WTs (Chapter 3). Additionally, M2 and its terminals show grooming-related increases in activity, and stimulation of M2 terminals in CS causes grooming. Taken together, these data suggest that M2 inputs may form behaviorally relevant CS cell ensembles and that the strength of this circuit is related to compulsive grooming behavior.

A particularly interesting aspect of these data are the temporal dynamics of the behavior manipulations. Central striatal stimulation resulted in a fairly immediate transition to grooming-related movements. Stimulation of M2 terminals in CS, however, had a significantly longer latency of grooming onset, approximately ~5s. If the start signal for grooming were relayed from M2 to CS, the prediction would be that M2 terminal activation would result in short latency grooming behavior. Thus, these data open the door to the idea that striatum may lead cortex in behavioral initiation activity. While our imaging data do not have a high enough temporal resolution to answer

this question, this idea is supported by previous work demonstrating that movement signals arise in striatum prior to cortex in primates (Pasupathy and Miller, 2005).

5.2 Behavioral Selection in the Central Striatum

5.2.1 Central Striatal Cell Ensembles

A large body of evidence now suggests that striatal cells function in ensembles that include both dSPNs and iSPNs, as well as interneurons (Barbera et al., 2016; Gritton et al., 2019; Parker et al., 2018). Data from our lab and others has demonstrated that striatal cell ensembles play a role in the selection and initiation of various movements, including locomotion, licking, and grooming (Burguiere et al., 2013; Gritton et al., 2019; Kravitz et al., 2010; Kravitz et al., 2012; Mittler et al., 1994). Exactly which behaviors are encoded in these ensembles likely has to do with specifically where in striatum the ensemble is located, with dorsolateral/dorsomedial striatum being important for rearing and locomotion, central striatum being important for grooming, and centrolateral striatum being important for licking (Burguiere et al., 2013; Kravitz et al., 2010; Kravitz et al., 2012; Mittler et al., 1994; Pisa, 1988).

What determines how these ensembles are generated is still unclear, though some data suggest that, in learned behaviors, striatal FSIs play an important role in shaping SPN ensembles as mice learn (Lee et al., 2017; O'Hare et al., 2017; Owen et al., 2018). Potentially, in naturalistic behaviors, ensembles are formed early in life, based on SPN-SPN connectivity, interneuron connectivity, and outside inputs from areas such as cortex or GPe. What is clear from modeling work is that FSIs can play a strong role in shaping SPN ensemble output (Damodaran et al., 2015;

Damodaran et al., 2013, Chapter 2). Because FSIs receive strong cortical and GPe input, it follows that these outside inputs could play a strong indirect role on shaping functional and anatomical connectivity between cells in an ensemble.

There is still much work to be done to investigate the role of FSIs in these cellular ensembles. It has been demonstrated that dorsomedial FSIs are active at the beginning of a locomotion bout, and stimulation of FSIs can evoke a locomotion bout (Gritton et al., 2019). Preliminary data from our lab also shows an increase in FSIs at the beginning of a compulsive grooming bout in KOs (Appendix B). FSIs have strong inhibitory synapses on SPNs (Gittis et al., 2010), which predicts that increases in FSI activity would correspond to a decrease in SPN activity. In both cases, however, that is not what has been observed (Gritton et al., 2019; Owen et al., 2018)(Appendix B). Interestingly, while striatal FSIs are perfectly poised to regulate feed-forward inhibition onto SPNs, it has been difficult to demonstrate that feed-forward inhibition in vivo, despite evidence of this type of inhibition from cortical FSIs (Bakhurin et al., 2016; Gage et al., 2010). Thus, more nuanced investigations of cellular ensembles in striatum will be necessary to further understand how FSIs play a role in regulating these ensembles in behavioral selection and initiation. The idea of FSIs playing a role in behavioral initiations is supported by data from Chapter 3 showing that FSIs receive greater excitatory drive in *Sapap3*-KOs. Specifically, if FSIs are receiving greater drive in *Sapap3*-KOs and FSIs are involved in behavioral initiations, they may be more readily activated and able to initiate grooming behaviors more excessively.

The stimulation of central striatum described in Chapter 4 was conducted with a pan-neuronal virus that infects interneurons in addition to SPNs. Thus, the effects of this stimulation potentially may involve activation of FSIs instead of or in addition to SPNs. Regardless, stimulation of central striatum produced what appeared to be “pieces” of grooming movements,

rather than full grooming sequences. This suggests that cell ensembles in central striatum may be important for the expression of specific aspects of grooming behavior. Interestingly, the proportions of CS activated and inhibited cells from CS stimulation and from grooming onset are weighted in opposite directions, such that the stimulation causes more inhibited cells (Fig. 4.2) while grooming onset shows a pattern of more activated cells (Appendix A). This presents the possibility that our stimulation paradigm may be causing an inappropriate balance of activation and inhibition in CS ensembles, which may lead to the "grooming-like" movements we observed rather than normal grooming behavior. It is also possible that the stereotyped partial movements we observed are due to incomplete activation of full behavioral ensembles in striatum. In contrast, stimulation of M2 terminals produced normal-looking grooming behavior, suggesting that, when CS ensembles are activated in a move naturalistic way by cortical input, they evoke more complete grooming behavior.

5.2.2 Central Striatum Integrates Multiple Inputs to Generate Movement Signals

While movement plans may be stored in striatum, it is not obvious the way behaviors are selected from that repertoire or how movements are initiated. One possibility is that behaviors are selected and initiated by upstream cortical inputs to striatum, which is supported by previous work examining dorsal striatum and prefrontal cortex in primates (Seo et al., 2012). However, given our data showing that stimulation of M2 terminals in central striatum causes a behavior effect at a long latency, it seems unlikely that initiation signals are coming from M2. Another possible site of behavioral selection and initiation is in striatum itself.

Though striatal cells rest relatively hyperpolarized and need external input to fire Gertler 2008; Gittis 2010; Chapter 2,3), they exhibit depolarized upstates interleaved with hyperpolarized

downstates in their resting potential (Plenz and Kitai, 1998; Stern et al., 1998; Wilson and Kawaguchi, 1996). In these permissive upstates, they are more likely to fire in response to an excitatory input (Plenz and Kitai, 1998; Stern et al., 1998; Wilson and Kawaguchi, 1996). Interestingly, it has been shown that striatal upstates are synchronous between nearby cells (Stern et al., 1998), suggesting common inputs forming a cellular ensemble. Accordingly, it is thought that cortical inputs cause striatal upstates (Plotkin et al., 2011; Wilson and Kawaguchi, 1996). Therefore, the role of M2 cortical inputs in movement initiation may be to put SPNs into upstates.

These upstates then may need to coincide with another excitatory signal (i.e. from thalamus or other cortical regions) or a disinhibitory signal (i.e. from FSIs via GPe) in order for striatal activation to cause movement initiation. For instance, CS activation may initiate grooming bouts via simultaneous inputs from M2, LOFC, and GPe via FSIs. By summing these excitatory and disinhibitory inputs, enough cells in a relevant ensemble may exceed some threshold of activity such that grooming movements are initiated (Fig. 5.1).

There is some evidence for each of these possibilities. GPe activity would inhibit FSIs and allow SPNs to become more depolarized. GPe activity is also associated with stereotypy (Grabli et al., 2004), as well as locomotion initiation (Anderson and Horak, 1985), suggesting that activity in GPe may play a role in movement initiations. An additional possibility is that signals from LOFC into CS play a role in grooming initiation. Unpublished single photon imaging data show that LOFC also shows an increase in activity at the start of a grooming bout. This suggests that input from LOFC could also be causal to the initiation of grooming movements. Potentially, LOFC input is one of several inputs needed for central striatum to generate “start” activity for a grooming bout in healthy conditions.

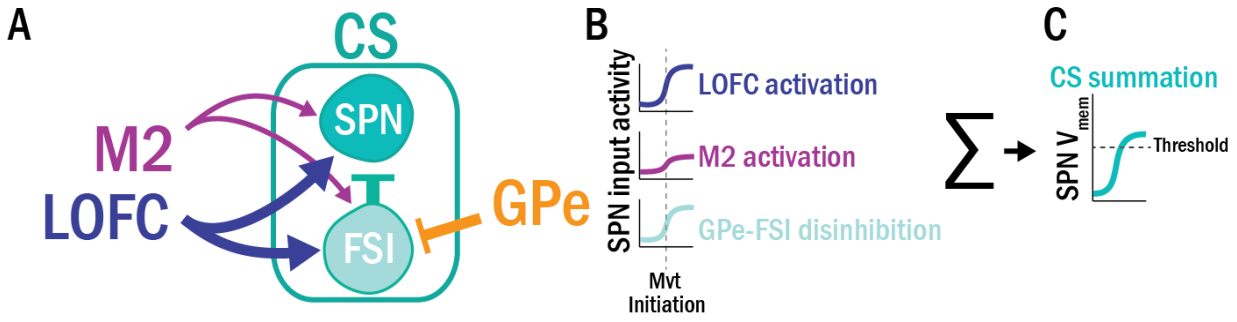

Figure 5.1 Conceptual model of how CS sums several inputs to generate movement initiation signals

(A) CS SPNs and FSIs receive excitatory inputs from M2 (weak) and LOFC (strong). FSIs inhibit SPNs and receive inhibitory input from GPe, resulting in GPe input causing disinhibition in SPNs. (B) Data suggests that M2 and LOFC are both active at the beginning of a grooming bout. GPe has not been studied in ths context but is known to be active at the beginning of a locomotion bout. It is therefore possible that simultaneous activation of these three inputs occurs at the beginning of a grooming bout. (C) CS SPNs would then summate these inputs and, with enough depolarization, exceed a threshold level of activation and theoretically cause a grooming initiation.

5.2.3 Compulsive Behavioral Selection

Behavioral selection in compulsive conditions could stem from two different types of abnormality: 1) an increase in the initiations of behavior and 2) a reduction in the cessations of behavior. We observe both of these abnormalities in the compulsive grooming behavior in the *Sapap3*-KO mice (Appendix B), i.e. we observe increased total grooming amount due to increased bout initiations and/or lengthened grooming bout durations (decreased cessations), depending on the specific group of mice. These two aspects of compulsive behavior may be generated by similar or different mechanisms in cortico-basal ganglia circuits.

First, increased initiations of grooming behavior likely involve an increase in movement initiation signals. The hypothesis that multiple inputs need to be integrated in striatum for

movement initiation signals to be generated predicts that changes in any or all of these inputs could cause increased movement initiations. There are several pieces of evidence that suggest these inputs may play a role in increased grooming initiations in *Sapap3*-KOs.

As Chapter 3 and 4 describe, a post-synaptic strengthening of the M2 synapses in CS in the *Sapap3*-KOs coincides with in an increased activation of CS during grooming behavior. This increased activation could generate greater depolarization of SPNs and therefore put them in a state where spiking activity is more readily evoked. Data from Chapter 4 supports this prediction, showing that stimulation of M2 terminals in CS causes grooming more reliably in KOs relative to WTs (Fig. 4.3D).

In contrast, LOFC input to CS in KOs is reduced specifically onto SPNs and not FSIs (Chapter 3). This suggests that, in response to an input from LOFC, the FSI-SPN microcircuit would exhibit enhanced feed-forward inhibition. However, unpublished in vivo data from our lab shows that LOFC cells have a grooming-related increase in calcium activity, but that this activity is weakened in KOs. Taken together with the disproportionate input to FSIs, this suggests a reduction of LOFC-evoked FSI-mediated inhibition of SPNs. Simultaneous with M2 and GPe inputs, this loss of LOFC activity onto FSIs may contribute to hyperactivity in CS SPNs in KOs. These data can also explain how stimulation of LOFC input to CS reduces grooming behavior in KOs, rather than increases it (Burguiere et al., 2013). Artificial activation of LOFC (Burguiere et al., 2013) would disproportionately activate FSIs relative to SPNs in KOs and cause an overregulation of SPN ensemble activity, and a theoretical reduction in grooming behavior. As LOFC is known to be involved in behavioral flexibility (Ragozzino, 2007), it follows that it may play a role in the ability to stop an ongoing movement (Burguiere et al., 2013).

The role of GPe in compulsive behaviors is less clear. Disinhibition of GPe activity in primates produces stereotypies, suggesting that GPe activity may play a role in abnormal behavioral initiations (Grabli et al., 2004). Traditional models of the direct and indirect pathway predict that increased behavioral initiations, such as could occur in compulsive behaviors, would be due to an imbalance of activity in SPNs, favoring dSPNs. In this model, iSPNs would have proportionately reduced activity, causing reduced activation of GPe. However, data from our lab suggests that iSPNs may actually show increased activity in *Sapap3*-KO mice (data not shown), which would suggest a heightened inhibition of GPe is associated with compulsive grooming behavior. In support of this idea, preliminary evidence shows that ablating a PV-positive sub-population of GPe causes a trend increase in grooming behavior in KO mice (Appendix B). Thus, there is some evidence that GPe may play a role in compulsive behavior, though the exact mechanism of this is unclear.

5.2.4 Behavioral Selection and Akinesia

On the opposite end of the behavioral selection spectrum is akinesia, or the inability to initiate movements, such as in dopamine depletion. Under the conceptual model of behavioral selection presented here, this would predict reduced inputs to striatum from one or several of its sources, or some effects in striatum itself that reduce excitability.

Glutamatergic input, likely from cortex and thalamus, is reduced onto iSPNs in dopamine depletion (Day et al., 2006). Other work has demonstrated a selective reduction of activity in dSPN-projecting cortical neurons, suggesting reduced excitatory drive to dSPNs as well (Mallet et al., 2006). In contrast, GPe input to striatum is not reduced in dopamine depletion (Chapter 2); however, the connectivity from FSIs to SPNs in striatum is known to be heightened in dopamine

depletion (Gittis et al., 2011a). Taken together, these data suggest that SPNs may be over-inhibited and under-excited in depleted conditions, reducing overall SPN activity. Furthermore, GPe activity is more synchronous and bursty in dopamine depleted conditions (Bevan et al., 2002). This means that while GPe connections to FSIs may not be altered in dopamine depletion, the ability of GPe to modulate FSI, and therefore SPN, activity may be strengthened due to increased synchrony in the inputs (Chapter 2). This activity would result in a reduction of information processing in GPe and throughout the basal ganglia, including in striatum.

5.3 Final Remarks

The work presented here highlights an important role for cortico-basal ganglia circuitry in behavioral selection and initiation in mice. Moving forward, it is important to keep in consideration how these findings can be applied to human patients. The ultimate goal of neuroscience is to understand how the brain works in healthy and disease conditions in humans, yet much of the discoveries in the field come from rodents. In the last words of this dissertation, I will highlight some key parallels in humans and non-human primates and briefly discuss how to improve these translations.

While central striatum does not yet have a designated homologue in humans, the caudate head in non-human primates receives input from LOFC and supplementary motor cortical areas (McFarland and Haber, 2000; Selemon and Goldman-Rakic, 1985). It is also worth noting that the anterior region of M2 that I studied may be more similar to prefrontal areas in human than to supplementary motor areas. While this is unclear until systematic in vivo and anatomical tracing studies characterize the extent of M2 in the rodent, my photometry data suggest that there is a

motor-related component to the activity observed in anterior M2. Furthermore, a pallidostriatal projection has been described in a variety of species, including cats and non human primates (Beckstead, 1983; Sato et al., 2000; Spooren et al., 1996), leaving open the possibility that these projections exist in humans as well. Additionally, LOFC and pre-SMA/SMA have both been associated with compulsive behavior via imaging studies (Bohlhalter et al., 2006; Chamberlain et al., 2008; de Wit et al., 2012a; Grützmann et al., 2016; Maltby et al., 2005; Neuner et al., 2014; Saxena et al., 1998; van Velzen et al., 2014; Yücel et al., 2007). These regions have been identified as promising regions for repetitive transcranial magnetic stimulation treatments (Berlim et al., 2013), suggesting that the data presented here showing M2 hyperactivity and LOFC hypoactivity in mice may be able to inform treatment parameter spaces for humans.

In sum, this work demonstrates a potential role for input integration in the striatum in behavioral selection. Specifically, I have shown that GPe projections to FSIs can strongly shape SPN activity, that M2 synapses are post-synaptically strengthened in central striatum in a mouse model of compulsive behavior, and that the M2-CS circuit is involved in grooming behavior. Taken together, these data suggest a model in which the integration of cortical inputs and pallidal inputs is important for the generation of movement initiation signals in striatum. This is a novel perspective on behavioral selection and initiation, proposing that striatum itself is the site of movement initiation. This hypothesis must be further investigated using in vivo physiology and projection-specific inhibition of these inputs to understand how they affects striatal activity and behavioral output.

Appendix A

Supplementary data related to in vivo activity in M2-CS circuit of *Sapap3*-KOs and WTs

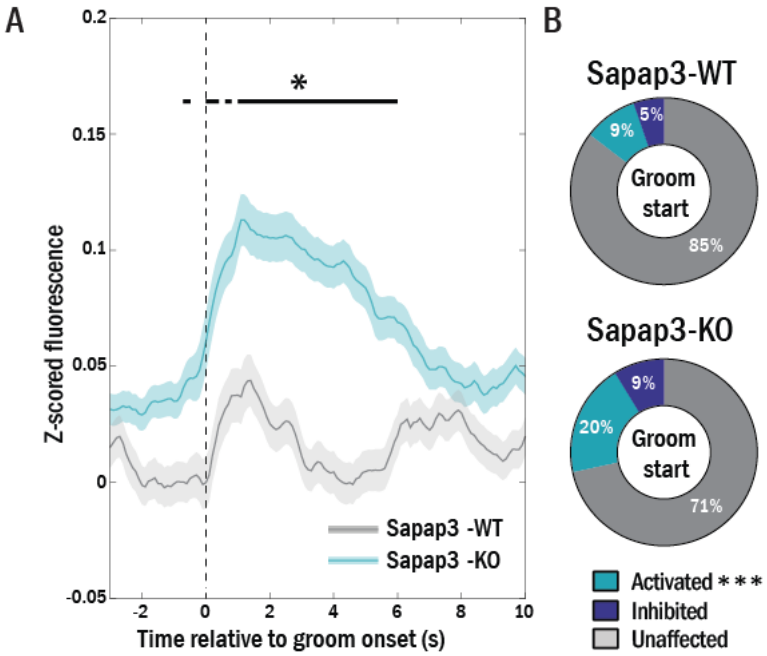

Figure 5.2 *Sapap3*-KOs show heightened CS activity relative to WTs at the onset of grooming. **(A) Averaged single-cell calcium imaging data from WTs and KOs at the onset of grooming. Both genotypes show an increase in activity at grooming onset, but KOs show a significantly greater activity increase relative to WTs. (B) Hyperactivation in CS in KOs is due to greater numbers of grooming-activated cells. Data collected by Dr. Sean Piantadosi, Ahmari Lab.**

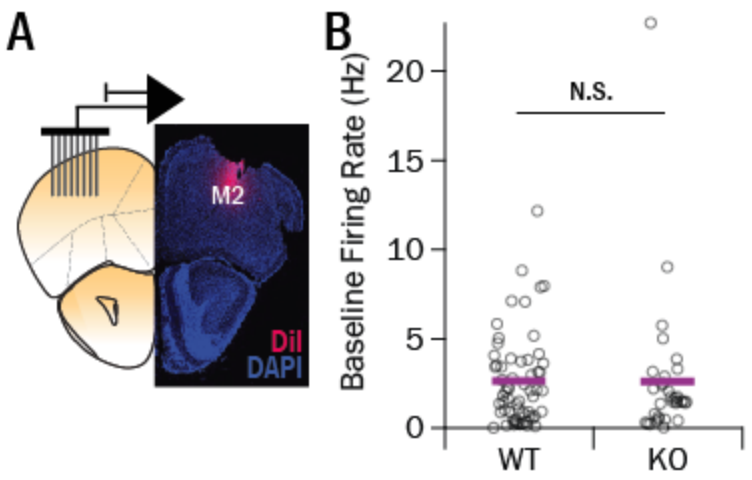

Figure 5.3 M2 in vivo baseline activity is not different in *Sapap3*-KOs and WTs.

(A) Eight tetrodes were implanted unilaterally in M2 of WT (N=5) and KO (N=4) mice. (B) Baseline firing rates observed were not significantly different between genotypes, t(91) = .33, p = .746. Data collected by Dr. Jesse Wood, Ahmari Lab.

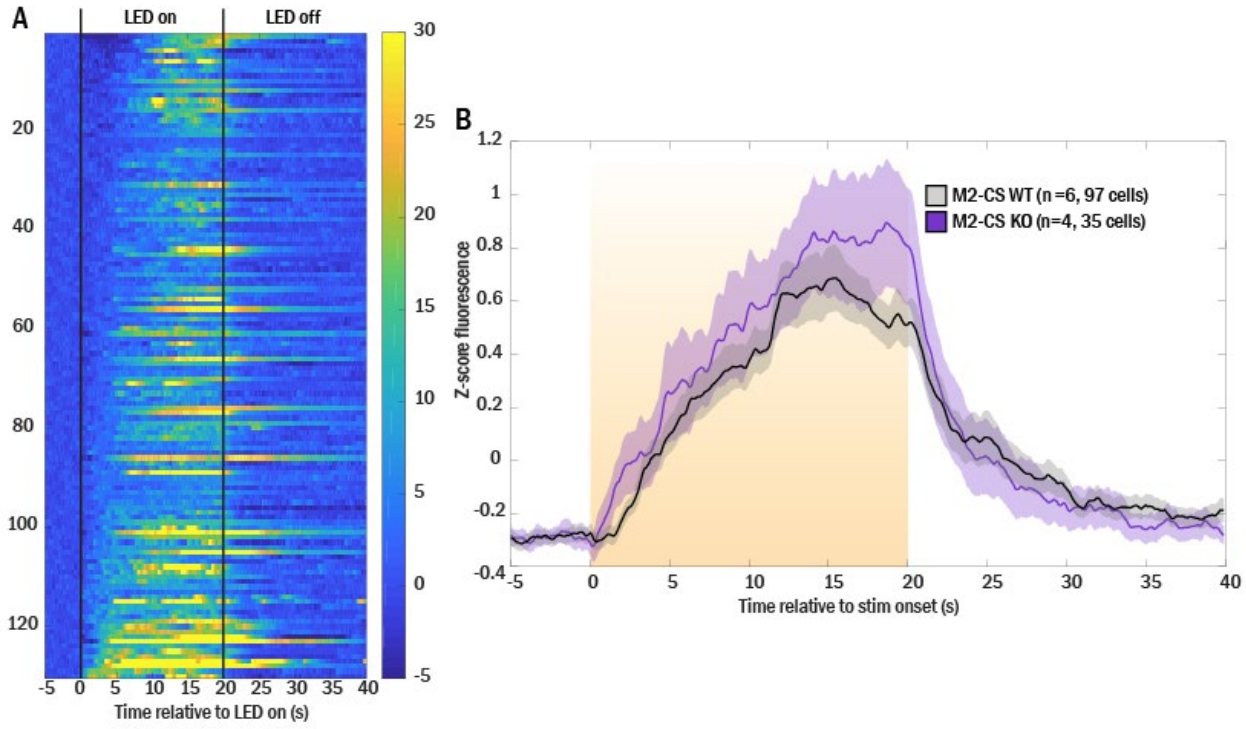

Figure 5.4 M2 stimulation evokes long latency activation in CS cells.

(A) Heat map showing all activated cells' GCaMP6m z-scored fluorescence activity in response to optogenetic activation of M2 terminals. (B) Average amplitude of response in activated cells in WTs and *Sapap3*-KOs, with no significant difference in genotypes. Data collection by Dr. Sean Piantadosi, Ahmari Lab.

Appendix B

Supplementary figures related to discussion of behavioral selection and initiation in striatal microcircuits

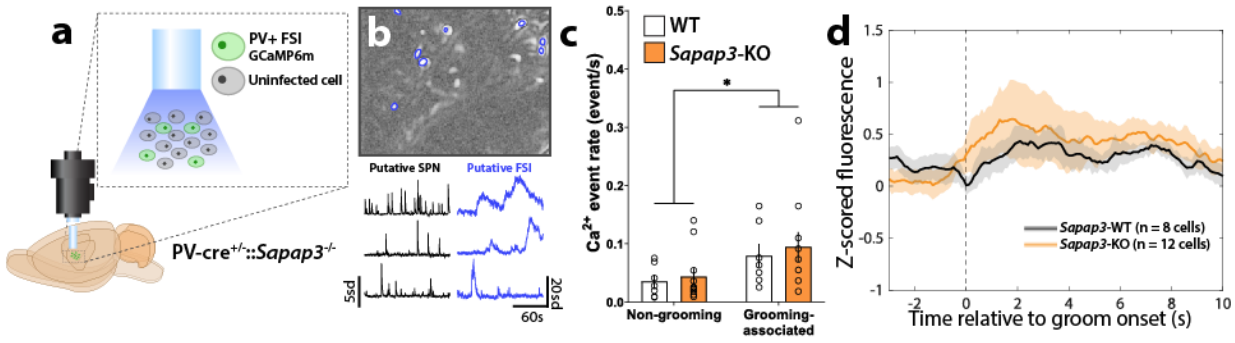

Figure 5.5 PV-positive cells in striatum show increased broad activity at the start of grooming. **(A) Cre-dependent GCamp6m was injected into the double transgenic PV-cre/*Sapap3*-KOs and WTs and a lens was implanted over the injection site. (B) Example field of view and calcium activity traces from a putative PV-positive FSI and a putative SPN (different animal). (C) Calicum event rates in PV-cells were significantly greater during grooming periods relative to non-grooming periods. (D) In both *Sapap3*-KOs and WTs, striatal PV cells show a broad increase in activity at the start of a grooming bout, though this increase is only significant in KOs (t(18) = -5.40, p = 3.9e-5). Data collected by Dr. Sean Piantadosi, Ahmari Lab.**

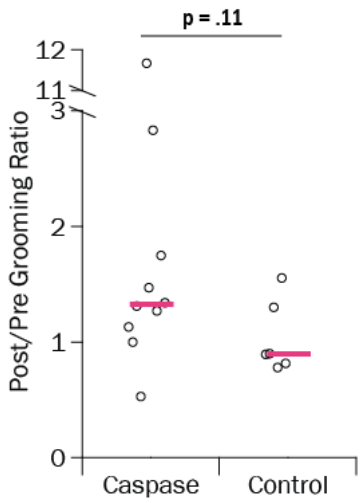

Figure 5.6 Ablating PV-positive cells in GPe increases grooming behavior.

Injection of cre-dependent caspase into the GPe of PV-cre *Sapap3*-KOs ablates PV-positive cells in GPe. This ablation causes a trend increase in grooming behavior when looking at the Post/Pre-sugery grooming ratio.

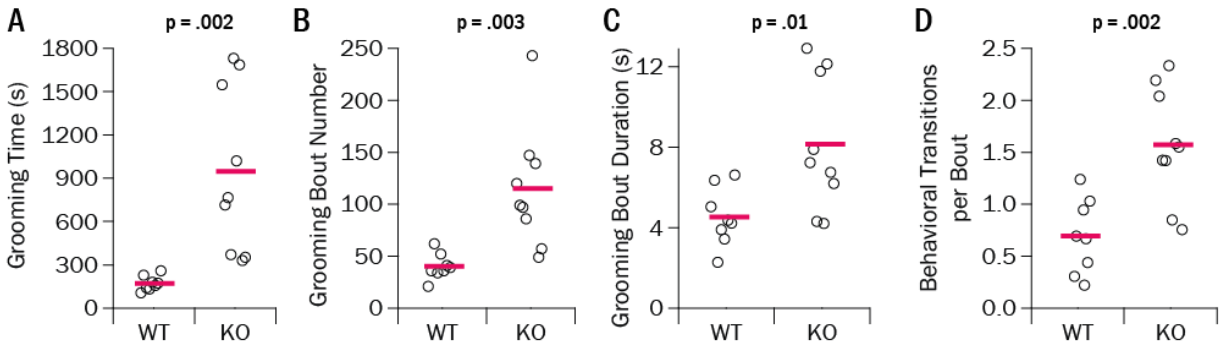

Figure 5.7 Grooming behavior shows increased initiations and bout durations in *Sapap3*-KOs.

***Sapap3*-KO mice show significantly greater total grooming time (A), increased number of bouts initiated (B), and increased bout duration (C). Additionally, KO mice transition more frequently between different types of grooming within a grooming bout, causing a significantly increased transitions per bout ratios.**

Bibliography

Abdi, A., Mallet, N., Mohamed, F.Y., Sharott, A., Dodson, P.D., Nakamura, K.C., Suri, S., Avery, S.V., Larvin, J.T., and Garas, F.N. (2015). Prototypic and arkypallidal neurons in the dopamine-intact external globus pallidus. Journal of Neuroscience *35*, 6667-6688.

Aberman, J., and Salamone, J.D. (1999). Nucleus accumbens dopamine depletions make rats more sensitive to high ratio requirements but do not impair primary food reinforcement. Neuroscience *92*, 545-552.

Ade, K.K., Wan, Y., Hamann, H.C., O'Hare, J.K., Guo, W., Quian, A., Kumar, S., Bhagat, S., Rodriguiz, R.M., and Wetsel, W.C. (2016). Increased metabotropic glutamate receptor 5 signaling underlies obsessive-compulsive disorder-like behavioral and striatal circuit abnormalities in mice. Biological psychiatry *80*, 522-533.

Ahmari, S.E., Spellman, T., Douglass, N.L., Kheirbek, M.A., Simpson, H.B., Deisseroth, K., Gordon, J.A., and Hen, R. (2013). Repeated cortico-striatal stimulation generates persistent OCD-like behavior. Science *340*, 1234-1239.

Akhlaghpour, H., Wiskerke, J., Choi, J.Y., Taliaferro, J.P., Au, J., and Witten, I.B. (2016). Dissociated sequential activity and stimulus encoding in the dorsomedial striatum during spatial working memory. Elife *5*, e19507.

Albin, R., Koeppe, R., Bohnen, N., Nichols, T., Meyer, P., Wernette, K., Minoshima, S., Kilbourn, M., and Frey, K. (2003). Increased ventral striatal monoaminergic innervation in Tourette syndrome. Neurology *61*, 310-315.

Aldridge, J.W., and Berridge, K.C. (1998). Coding of serial order by neostriatal neurons: a "natural action" approach to movement sequence. Journal of Neuroscience *18*, 2777-2787.

Aldridge, J.W., Berridge, K.C., Herman, M., and Zimmer, L. (1993). Neuronal coding of serial order: syntax of grooming in the neostriatum. Psychological Science *4*, 391-395.

Alexander, G.E., and DeLong, M.R. (1985). Microstimulation of the primate neostriatum. II. Somatotopic organization of striatal microexcitable zones and their relation to neuronal response properties. Journal of Neurophysiology *53*, 1417-1430.

Alexander, G.E., DeLong, M.R., and Strick, P.L. (1986). Parallel organization of functionally segregated circuits linking basal ganglia and cortex. Annu Rev Neurosci *9*, 357-381.

Amador, N., and Fried, I. (2004). Single-neuron activity in the human supplementary motor area underlying preparation for action. Journal of neurosurgery *100*, 250-259.

Anderson, M., and Horak, F. (1985). Influence of the globus pallidus on arm movements in monkeys. III. Timing of movement-related information. Journal of neurophysiology *54*, 433-448.

Apicella, P., Ljungberg, T., Scarnati, E., and Schultz, W. (1991). Responses to reward in monkey dorsal and ventral striatum. Experimental brain research *85*, 491-500.

Ashby, F.G., Turner, B.O., and Horvitz, J.C. (2010). Cortical and basal ganglia contributions to habit learning and automaticity. Trends in cognitive sciences *14*, 208-215.

Ayuso-Mateos, J.L. (2006). Global burden of obsessive-compulsive disorder in the year 2000. World Health Organization.

Azdad, K., Chàvez, M., Bischop, P.D., Wetzelaer, P., Marescau, B., De Deyn, P.P., Gall, D., and Schiffmann, S.N. (2009). Homeostatic plasticity of striatal neurons intrinsic excitability following dopamine depletion. PloS one *4*, e6908.

Bakhurin, K.I., Mac, V., Golshani, P., and Masmanidis, S.C. (2016). Temporal correlations among functionally specialized striatal neural ensembles in reward conditioned mice. American Journal of Physiology-Heart and Circulatory Physiology.

Balleine, B.W., Delgado, M.R., and Hikosaka, O. (2007). The role of the dorsal striatum in reward and decision-making. Journal of Neuroscience *27*, 8161-8165.

Bar-Gad, I., Heimer, G., Ritov, Y.a., and Bergman, H. (2003). Functional correlations between neighboring neurons in the primate globus pallidus are weak or nonexistent. Journal of Neuroscience *23*, 4012-4016.

Barbera, G., Liang, B., Zhang, L., Gerfen, C.R., Culurciello, E., Chen, R., Li, Y., and Lin, D.-T. (2016). Spatially compact neural clusters in the dorsal striatum encode locomotion relevant information. Neuron *92*, 202-213.

Barthas, F., and Kwan, A.C. (2017). Secondary motor cortex: where 'sensory'meets 'motor'in the rodent frontal cortex. Trends in neurosciences *40*, 181-193.

Beckstead, R.M. (1983). A pallidostriatal projection in the cat and monkey. Brain research bulletin *11*, 629-632.

Bergman, H. (2004). The basal ganglia pathophysiological model: Contributions and limitations. Paper presented at: MOVEMENT DISORDERS (WILEY-LISS DIV JOHN WILEY & SONS INC, 111 RIVER ST, HOBOKEN, NJ 07030 USA).

Bergman, H., Feingold, A., Nini, A., Raz, A., Slovin, H., Abeles, M., and Vaadia, E. (1998). Physiological aspects of information processing in the basal ganglia of normal and parkinsonian primates. Trends in neurosciences *21*, 32-38.

Bergstrom, H.C., Lipkin, A.M., Lieberman, A.G., Pinard, C.R., Gunduz-Cinar, O., Brockway, E.T., Taylor, W.W., Nonaka, M., Bukalo, O., and Wills, T.A. (2018). Dorsolateral striatum engagement interferes with early discrimination learning. Cell reports *23*, 2264-2272.

Berke, J. (2009). Fast oscillations in cortical-striatal networks switch frequency following rewarding events and stimulant drugs. European Journal of Neuroscience *30*, 848-859.

Berke, J.D. (2008). Uncoordinated firing rate changes of striatal fast-spiking interneurons during behavioral task performance. The Journal of Neuroscience *28*, 10075-10080.

Berke, J.D. (2011). Functional properties of striatal fast-spiking interneurons. Front Syst Neurosci *5*.

Berlim, M.T., Neufeld, N.H., and Van den Eynde, F. (2013). Repetitive transcranial magnetic stimulation (rTMS) for obsessive–compulsive disorder (OCD): An exploratory meta-analysis of randomized and sham-controlled trials. Journal of psychiatric research *47*, 999-1006.

Bevan, M.D., Booth, P.A., Eaton, S.A., and Bolam, J.P. (1998). Selective innervation of neostriatal interneurons by a subclass of neuron in the globus pallidus of the rat. Journal of Neuroscience *18*, 9438-9452.

Bevan, M.D., Magill, P.J., Terman, D., Bolam, J.P., and Wilson, C.J. (2002). Move to the rhythm: oscillations in the subthalamic nucleus–external globus pallidus network. Trends in neurosciences *25*, 525-531.

Bienvenu, O., Wang, Y., Shugart, Y., Welch, J., Grados, M., Fyer, A., Rauch, S., McCracken, J., Rasmussen, S., and Murphy, D. (2009). *Sapap3* and pathological grooming in humans: Results from the OCD collaborative genetics study. American Journal of Medical Genetics Part B: Neuropsychiatric Genetics *150*, 710-720.

Björklund, A., and Dunnett, S.B. (2007). Dopamine neuron systems in the brain: an update. Trends in neurosciences *30*, 194-202.

Bohlhalter, S., Goldfine, A., Matteson, S., Garraux, G., Hanakawa, T., Kansaku, K., Wurzman, R., and Hallett, M. (2006). Neural correlates of tic generation in Tourette syndrome: an event-related functional MRI study. Brain *129*, 2029-2037.

Bohn, I., Giertler, C., and Hauber, W. (2003). Orbital prefrontal cortex and guidance of instrumental behaviour in rats under reversal conditions. Behavioural brain research *143*, 49-56.

Boraud, T., Bezard, E., Bioulac, B., and Gross, C.E. (2001). Dopamine agonist-induced dyskinesias are correlated to both firing pattern and frequency alterations of pallidal neurones in the MPTP-treated monkey. Brain *124*, 546-557.

Brittain, J.S., Sharott, A., and Brown, P. (2014). The highs and lows of beta activity in cortico-basal ganglia loops. European Journal of Neuroscience *39*, 1951-1959.

Bronfeld, M., Yael, D., Belelovsky, K., and Bar-Gad, I. (2013). Motor tics evoked by striatal disinhibition in the rat. Frontiers in systems neuroscience *7*, 50.

Bronte-Stewart, H., Barberini, C., Koop, M.M., Hill, B.C., Henderson, J.M., and Wingeier, B. (2009). The STN beta-band profile in Parkinson's disease is stationary and shows prolonged attenuation after deep brain stimulation. Experimental neurology *215*, 20-28.

Brown, P., Oliviero, A., Mazzone, P., Insola, A., Tonali, P., and Di Lazzaro, V. (2001). Dopamine dependency of oscillations between subthalamic nucleus and pallidum in Parkinson's disease. Journal of Neuroscience *21*, 1033-1038.

Brown, P., and Williams, D. (2005). Basal ganglia local field potential activity: character and functional significance in the human. Clinical neurophysiology *116*, 2510-2519.

Brown, V.J., and Robbins, T.W. (1989). Elementary processes of response selection mediated by distinct regions of the striatum. Journal of Neuroscience *9*, 3760-3765.

Bugaysen, J., Bar-Gad, I., and Korngreen, A. (2013). Continuous modulation of action potential firing by a unitary GABAergic connection in the globus pallidus in vitro. Journal of Neuroscience *33*, 12805-12809.

Burguiere, E., Monteiro, P., Feng, G., and Graybiel, A.M. (2013). Optogenetic stimulation of lateral orbitofronto-striatal pathway suppresses compulsive behaviors. Science *340*, 1243-1246.

Cao, V.Y., Ye, Y., Mastwal, S., Ren, M., Coon, M., Liu, Q., Costa, R.M., and Wang, K.H. (2015). Motor Learning Consolidates Arc-Expressing Neuronal Ensembles in Secondary Motor Cortex. Neuron *86*, 1385-1392.

Cao, X., Cui, Z., Feng, R., Tang, Y.P., Qin, Z., Mei, B., and Tsien, J.Z. (2007). Maintenance of superior learning and memory function in NR2B transgenic mice during ageing. European Journal of Neuroscience *25*, 1815-1822.

Cardin, J.A., Carlén, M., Meletis, K., Knoblich, U., Zhang, F., Deisseroth, K., Tsai, L.-H., and Moore, C.I. (2009). Driving fast-spiking cells induces gamma rhythm and controls sensory responses. Nature *459*, 663.

Cardinal, R.N., Pennicott, D.R., Lakmali, C., Robbins, T.W., and Everitt, B.J. (2001). Impulsive choice induced in rats by lesions of the nucleus accumbens core. Science *292*, 2499-2501.

Carrillo-Reid, L., Tecuapetla, F., Tapia, D., Hernández-Cruz, A., Galarraga, E., Drucker-Colin, R., and Bargas, J. (2008). Encoding network states by striatal cell assemblies. Journal of neurophysiology.

Chamberlain, S.R., Menzies, L., Hampshire, A., Suckling, J., Fineberg, N.A., del Campo, N., Aitken, M., Craig, K., Owen, A.M., and Bullmore, E.T. (2008). Orbitofrontal dysfunction in patients with obsessive-compulsive disorder and their unaffected relatives. Science *321*, 421-422.

Chamberlain, S.R., Odlaug, B.L., Boulougouris, V., Fineberg, N.A., and Grant, J.E. (2009). Trichotillomania: neurobiology and treatment. Neuroscience & Biobehavioral Reviews *33*, 831-842.

Chen, M., Wan, Y., Ade, K., Ting, J., Feng, G., and Calakos, N. (2011). *Sapap3* deletion anomalously activates short-term endocannabinoid-mediated synaptic plasticity. Journal of Neuroscience *31*, 9563-9573.

Cheyne, D., Bells, S., Ferrari, P., Gaetz, W., and Bostan, A.C. (2008). Self-paced movements induce high-frequency gamma oscillations in primary motor cortex. Neuroimage *42*, 332-342.

Chuhma, N., Tanaka, K.F., Hen, R., and Rayport, S. (2011). Functional connectome of the striatal medium spiny neuron. Journal of Neuroscience *31*, 1183-1192.

Clarke, H.F., Robbins, T.W., and Roberts, A.C. (2008). Lesions of the medial striatum in monkeys produce perseverative impairments during reversal learning similar to those produced by lesions of the orbitofrontal cortex. Journal of Neuroscience *28*, 10972-10982.

Coffey, K.R., Nader, M., and West, M.O. (2016). Single body parts are processed by individual neurons in the mouse dorsolateral striatum. Brain research *1636*, 200-207.

Corbit, V.L., Manning, E.E., Gittis, A.H., and Ahmari, S.E. (2019). Strengthened inputs from secondary motor cortex to striatum in a mouse model of compulsive behavior. Journal of Neuroscience *39*, 2965-2975.

Corbit, V.L., Whalen, T.C., Zitelli, K.T., Crilly, S.Y., Rubin, J.E., and Gittis, A.H. (2016). Pallidostriatal Projections Promote beta Oscillations in a Dopamine-Depleted Biophysical Network Model. J Neurosci *36*, 5556-5571.

Courtemanche, R., Fujii, N., and Graybiel, A.M. (2003). Synchronous, focally modulated β-band oscillations characterize local field potential activity in the striatum of awake behaving monkeys. Journal of Neuroscience *23*, 11741-11752.

Crane, J., Fagerness, J., Osiecki, L., Gunnell, B., Stewart, S.E., Pauls, D.L., Scharf, J.M., and Genetics, T.S.I.C.f. (2011). Family-based genetic association study of DLGAP3 in Tourette Syndrome. American Journal of Medical Genetics Part B: Neuropsychiatric Genetics *156*, 108-114.

Cromwell, H.C., and Berridge, K.C. (1996). Implementation of action sequences by a neostriatal site: a lesion mapping study of grooming syntax. Journal of Neuroscience *16*, 3444-3458.

Cui, G., Jun, S.B., Jin, X., Pham, M.D., Vogel, S.S., Lovinger, D.M., and Costa, R.M. (2013). Concurrent activation of striatal direct and indirect pathways during action initiation. Nature *494*, 238.

Curtis, C.E., and Lee, D. (2010). Beyond working memory: the role of persistent activity in decision making. Trends in cognitive sciences *14*, 216-222.

Dalton, G.L., Wang, N.Y., Phillips, A.G., and Floresco, S.B. (2016). Multifaceted contributions by different regions of the orbitofrontal and medial prefrontal cortex to probabilistic reversal learning. Journal of Neuroscience *36*, 1996-2006.

Damodaran, S., Cressman, J.R., Jedrzejewski-Szmek, Z., and Blackwell, K.T. (2015). Desynchronization of fast-spiking interneurons reduces β-band oscillations and imbalance in firing in the dopamine-depleted striatum. Journal of Neuroscience *35*, 1149-1159.

Damodaran, S., Evans, R.C., and Blackwell, K.T. (2013). Synchronized firing of fast-spiking interneurons is critical to maintain balanced firing between direct and indirect pathway neurons of the striatum. American Journal of Physiology-Heart and Circulatory Physiology.

Day, M., Wang, Z., Ding, J., An, X., Ingham, C.A., Shering, A.F., Wokosin, D., Ilijic, E., Sun, Z., and Sampson, A.R. (2006). Selective elimination of glutamatergic synapses on striatopallidal neurons in Parkinson disease models. Nature neuroscience *9*, 251.

De Hemptinne, C., Ryapolova-Webb, E.S., Air, E.L., Garcia, P.A., Miller, K.J., Ojemann, J.G., Ostrem, J.L., Galifianakis, N.B., and Starr, P.A. (2013). Exaggerated phase–amplitude coupling in the primary motor cortex in Parkinson disease. Proceedings of the National Academy of Sciences *110*, 4780-4785.

de Wit, S.J., de Vries, F.E., van der Werf, Y.D., Cath, D.C., Heslenfeld, D.J., Veltman, E.M., van Balkom, A.J., Veltman, D.J., and van den Heuvel, O.A. (2012a). Presupplementary motor area hyperactivity during response inhibition: a candidate endophenotype of obsessive-compulsive disorder. American Journal of Psychiatry *169*, 1100-1108.

de Wit, S.J., de Vries, F.E., van der Werf, Y.D., Cath, D.C., Heslenfeld, D.J., Veltman, E.M., van Balkom, A.J., Veltman, D.J., and van den Heuvel, O.A. (2012b). Presupplementary motor area hyperactivity during response inhibition: a candidate endophenotype of obsessive-compulsive disorder. American journal of psychiatry.

Del Casale, A., Kotzalidis, G., Rapinesi, C., Serata, D., Ambrosi, E., Simonetti, A., Pompili, M., Ferracuti, S., Tatarelli, R., and Girardi, P. (2011). Functional neuroimaging in obsessive-compulsive disorder. Neuropsychobiology *64*, 61-85.

Delgado, M.R. (2007). Reward-related responses in the human striatum. Annals of the New York Academy of Sciences *1104*, 70-88.

Deniau, J., and Chevalier, G. (1985). Disinhibition as a basic process in the expression of striatal functions. II. The striato-nigral influence on thalamocortical cells of the ventromedial thalamic nucleus. Brain research *334*, 227-233.

Denys, D., de Vries, F., Cath, D., Figee, M., Vulink, N., Veltman, D.J., van der Doef, T.F., Boellaard, R., Westenberg, H., and van Balkom, A. (2013). Dopaminergic activity in Tourette syndrome and obsessive-compulsive disorder. European neuropsychopharmacology *23*, 1423-1431.

Dodson, P.D., Larvin, J.T., Duffell, J.M., Garas, F.N., Doig, N.M., Kessaris, N., Duguid, I.C., Bogacz, R., Butt, S.J., and Magill, P.J. (2015). Distinct developmental origins manifest in the specialized encoding of movement by adult neurons of the external globus pallidus. Neuron *86*, 501-513.

Ermentrout, B. (2012). Xppaut. In Computational Systems Neurobiology (Springer), pp. 519-531.

Figee, M., Luigjes, J., Smolders, R., Valencia-Alfonso, C.-E., van Wingen, G., de Kwaasteniet, B., Mantione, M., Ooms, P., de Koning, P., and Vulink, N. (2013). Deep brain stimulation restores frontostriatal network activity in obsessive-compulsive disorder. Nature neuroscience *16*, 386-387.

Fino, E., Glowinski, J., and Venance, L. (2007). Effects of acute dopamine depletion on the electrophysiological properties of striatal neurons. Neuroscience research *58*, 305-316.

Flessner, C.A., Knopik, V.S., and McGeary, J. (2012). Hair pulling disorder (trichotillomania): genes, neurobiology, and a model for understanding impulsivity and compulsivity. Psychiatry research *199*, 151-158.

Freeze, B.S., Kravitz, A.V., Hammack, N., Berke, J.D., and Kreitzer, A.C. (2013). Control of basal ganglia output by direct and indirect pathway projection neurons. Journal of Neuroscience *33*, 18531-18539.

Friedman, A., Homma, D., Gibb, L.G., Amemori, K.-i., Rubin, S.J., Hood, A.S., Riad, M.H., and Graybiel, A.M. (2015). A corticostriatal path targeting striosomes controls decision-making under conflict. Cell *161*, 1320-1333.

Fujita, T., Fukai, T., and Kitano, K. (2012). Influences of membrane properties on phase response curve and synchronization stability in a model globus pallidus neuron. Journal of computational neuroscience *32*, 539-553.

Fujiyama, F., Nakano, T., Matsuda, W., Furuta, T., Udagawa, J., and Kaneko, T. (2016). A single-neuron tracing study of arkypallidal and prototypic neurons in healthy rats. Brain Structure and Function *221*, 4733-4740.

Gage, G.J., Stoetzner, C.R., Wiltschko, A.B., and Berke, J.D. (2010). Selective activation of striatal fast-spiking interneurons during choice execution. Neuron *67*, 466-479.

Gatev, P., Darbin, O., and Wichmann, T. (2006). Oscillations in the basal ganglia under normal conditions and in movement disorders. Movement disorders *21*, 1566-1577.

Gerfen, C.R. (1988). Synaptic organization of the striatum. Journal of electron microscopy technique *10*, 265-281.

Gerfen, C.R., and Young III, W.S. (1988). Distribution of striatonigral and striatopallidal peptidergic neurons in both patch and matrix compartments: an in situ hybridization histochemistry and fluorescent retrograde tracing study. Brain research *460*, 161-167.

Gertler, T.S., Chan, C.S., and Surmeier, D.J. (2008). Dichotomous anatomical properties of adult striatal medium spiny neurons. Journal of Neuroscience *28*, 10814-10824.

Gillan, C.M., and Robbins, T.W. (2014). Goal-directed learning and obsessive–compulsive disorder. Phil Trans R Soc B *369*, 20130475.

Gittis, A.H., Hang, G.B., LaDow, E.S., Shoenfeld, L.R., Atallah, B.V., Finkbeiner, S., and Kreitzer, A.C. (2011a). Rapid target-specific remodeling of fast-spiking inhibitory circuits after loss of dopamine. Neuron *71*, 858-868.

Gittis, A.H., Leventhal, D.K., Fensterheim, B.A., Pettibone, J.R., Berke, J.D., and Kreitzer, A.C. (2011b). Selective inhibition of striatal fast-spiking interneurons causes dyskinesias. The Journal of neuroscience *31*, 15727-15731.

Gittis, A.H., Nelson, A.B., Thwin, M.T., Palop, J.J., and Kreitzer, A.C. (2010). Distinct roles of GABAergic interneurons in the regulation of striatal output pathways. The Journal of Neuroscience *30*, 2223-2234.

Golomb, D., Donner, K., Shacham, L., Shlosberg, D., Amitai, Y., and Hansel, D. (2007). Mechanisms of firing patterns in fast-spiking cortical interneurons. PLoS Computational Biology *3*, e156.

Grabli, D., McCairn, K., Hirsch, E.C., Agid, Y., Féger, J., François, C., and Tremblay, L. (2004). Behavioural disorders induced by external globus pallidus dysfunction in primates: I. Behavioural study. Brain *127*, 2039-2054.

Greenberg, B., Gabriels, L., Malone Jr, D., Rezai, A., Friehs, G., Okun, M., Shapira, N., Foote, K., Cosyns, P., and Kubu, C. (2010). Deep brain stimulation of the ventral internal capsule/ventral striatum for obsessive-compulsive disorder: worldwide experience. Molecular psychiatry *15*, 64.

Gremel, C., and Costa, R. (2013a). Premotor cortex is critical for goal-directed actions. Frontiers in computational neuroscience *7*, 110.

Gremel, C.M., Chancey, J.H., Atwood, B.K., Luo, G., Neve, R., Ramakrishnan, C., Deisseroth, K., Lovinger, D.M., and Costa, R.M. (2016). Endocannabinoid modulation of orbitostriatal circuits gates habit formation. Neuron *90*, 1312-1324.

Gremel, C.M., and Costa, R.M. (2013b). Orbitofrontal and striatal circuits dynamically encode the shift between goal-directed and habitual actions. Nature communications *4*, 2264.

Gritton, H.J., Howe, W.M., Romano, M.F., DiFeliceantonio, A.G., Kramer, M.A., Saligrama, V., Bucklin, M.E., Zemel, D., and Han, X. (2019). Unique contributions of parvalbumin and cholinergic interneurons in organizing striatal networks during movement. Nature Neuroscience, 1.

Grützmann, R., Endrass, T., Kaufmann, C., Allen, E., Eichele, T., and Kathmann, N. (2016). Presupplementary motor area contributes to altered error monitoring in obsessive-compulsive disorder. Biological psychiatry *80*, 562-571.

Guo, Z.V., Li, N., Huber, D., Ophir, E., Gutnisky, D., Ting, J.T., Feng, G., and Svoboda, K. (2014). Flow of cortical activity underlying a tactile decision in mice. Neuron *81*, 179-194.

Guzmán, J.N., Hernández, A., Galarraga, E., Tapia, D., Laville, A., Vergara, R., Aceves, J., and Bargas, J. (2003). Dopaminergic modulation of axon collaterals interconnecting spiny neurons of the rat striatum. The Journal of neuroscience *23*, 8931-8940.

Haber, S.N. (2003). The primate basal ganglia: parallel and integrative networks. Journal of chemical neuroanatomy *26*, 317-330.

Haber, S.N., Fudge, J.L., and McFarland, N.R. (2000). Striatonigrostriatal pathways in primates form an ascending spiral from the shell to the dorsolateral striatum. Journal of Neuroscience *20*, 2369-2382.

Haber, S.N., Kim, K.-S., Mailly, P., and Calzavara, R. (2006). Reward-related cortical inputs define a large striatal region in primates that interface with associative cortical connections, providing a substrate for incentive-based learning. The Journal of Neuroscience *26*, 8368-8376.

Hammond, C., Bergman, H., and Brown, P. (2007). Pathological synchronization in Parkinson's disease: networks, models and treatments. Trends in neurosciences *30*, 357-364.

Harrison, B.J., Soriano-Mas, C., Pujol, J., Ortiz, H., López-Solà, M., Hernández-Ribas, R., Deus, J., Alonso, P., Yücel, M., and Pantelis, C. (2009). Altered corticostriatal functional connectivity in obsessive-compulsive disorder. Archives of general psychiatry *66*, 1189-1200.

Heimer, G., Rivlin, M., Israel, Z., and Bergman, H. (2006). Synchronizing activity of basal ganglia and pathophysiology of Parkinson's disease. In Parkinson's Disease and Related Disorders (Springer), pp. 17-20.

Hernandez, L.F., Kubota, Y., Hu, D., Howe, M.W., Lemaire, N., and Graybiel, A.M. (2013). Selective effects of dopamine depletion and L-DOPA therapy on learning-related firing dynamics of striatal neurons. Journal of Neuroscience *33*, 4782-4795.

Hernández, V.M., Hegeman, D.J., Cui, Q., Kelver, D.A., Fiske, M.P., Glajch, K.E., Pitt, J.E., Huang, T.Y., Justice, N.J., and Chan, C.S. (2015). Parvalbumin+ neurons and Npas1+ neurons are distinct neuron classes in the mouse external globus pallidus. Journal of Neuroscience *35*, 11830-11847.

Hirschmann, J., Özkurt, T.E., Butz, M., Homburger, M., Elben, S., Hartmann, C., Vesper, J., Wojtecki, L., and Schnitzler, A. (2011). Distinct oscillatory STN-cortical loops revealed by simultaneous MEG and local field potential recordings in patients with Parkinson's disease. Neuroimage *55*, 1159-1168.

Holgado, A.J.N., Terry, J.R., and Bogacz, R. (2010). Conditions for the generation of beta oscillations in the subthalamic nucleus–globus pallidus network. Journal of Neuroscience *30*, 12340-12352.

Humphries, M.D., and Prescott, T.J. (2010). The ventral basal ganglia, a selection mechanism at the crossroads of space, strategy, and reward. Progress in neurobiology *90*, 385-417.

Hutchison, W.D., Dostrovsky, J.O., Walters, J.R., Courtemanche, R., Boraud, T., Goldberg, J., and Brown, P. (2004). Neuronal oscillations in the basal ganglia and movement disorders: evidence from whole animal and human recordings. Journal of Neuroscience *24*, 9240-9243.

Isoda, M., and Hikosaka, O. (2007). Switching from automatic to controlled action by monkey medial frontal cortex. Nature neuroscience *10*, 240.

Jenkinson, N., and Brown, P. (2011). New insights into the relationship between dopamine, beta oscillations and motor function. Trends in neurosciences *34*, 611-618.

Jenkinson, N., Kühn, A.A., and Brown, P. (2013). Gamma oscillations in the human basal ganglia. Experimental neurology *245*, 72-76.

Jiang, Z., and North, R. (1991). Membrane properties and synaptic responses of rat striatal neurones in vitro. The Journal of Physiology *443*, 533-553.

Jin, X., Tecuapetla, F., and Costa, R.M. (2014). Basal ganglia subcircuits distinctively encode the parsing and concatenation of action sequences. Nature neuroscience *17*, 423.

Johnston, R.E., Schallert, T., and Becker, J.B. (1999). Akinesia and postural abnormality after unilateral dopamine depletion. Behavioural brain research *104*, 189-196.

Karno, M., Golding, J.M., Sorenson, S.B., and Burnam, M.A. (1988). The epidemiology of obsessive-compulsive disorder in five US communities. Archives of general psychiatry *45*, 1094-1099.

Kataoka, Y., Kalanithi, P.S., Grantz, H., Schwartz, M.L., Saper, C., Leckman, J.F., and Vaccarino, F.M. (2010). Decreased number of parvalbumin and cholinergic interneurons in the striatum of individuals with Tourette syndrome. Journal of Comparative Neurology *518*, 277-291.

Kemp, J.M., and Powell, T.P.S. (1971). The structure of the caudate nucleus of the cat: light and electron microscopy. Philosophical Transactions of the Royal Society of London B, Biological Sciences *262*, 383-401.

Kimchi, E.Y., and Laubach, M. (2009). Dynamic encoding of action selection by the medial striatum. Journal of Neuroscience *29*, 3148-3159.

Kita, H., Chiken, S., Tachibana, Y., and Nambu, A. (2007). Serotonin modulates pallidal neuronal activity in the awake monkey. Journal of Neuroscience *27*, 75-83.

Kita, H., and Kita, T. (2011). Cortical stimulation evokes abnormal responses in the dopamine-depleted rat basal ganglia. Journal of Neuroscience *31*, 10311-10322.

Kita, H., and Kitai, S. (1991). Intracellular study of rat globus pallidus neurons: membrane properties and responses to neostriatal, subthalamic and nigral stimulation. Brain research *564*, 296-305.

Kita, H., Kosaka, T., and Heizmann, C. (1990). Parvalbumin-immunoreactive neurons in the rat neostriatum: a light and electron microscopic study. Brain research *536*, 1-15.

Klaus, A., Martins, G.J., Paixao, V.B., Zhou, P., Paninski, L., and Costa, R.M. (2017). The spatiotemporal organization of the striatum encodes action space. Neuron *95*, 1171-1180. e1177.

Kravitz, A.V., Freeze, B.S., Parker, P.R., Kay, K., Thwin, M.T., Deisseroth, K., and Kreitzer, A.C. (2010). Regulation of parkinsonian motor behaviours by optogenetic control of basal ganglia circuitry. Nature *466*, 622.

Kravitz, A.V., Tye, L.D., and Kreitzer, A.C. (2012). Distinct roles for direct and indirect pathway striatal neurons in reinforcement. Nature neuroscience *15*, 816-818.

Kühn, A.A., Kupsch, A., Schneider, G.H., and Brown, P. (2006). Reduction in subthalamic 8–35 Hz oscillatory activity correlates with clinical improvement in Parkinson's disease. European Journal of Neuroscience *23*, 1956-1960.

Kühn, A.A., Tsui, A., Aziz, T., Ray, N., Brücke, C., Kupsch, A., Schneider, G.-H., and Brown, P. (2009). Pathological synchronisation in the subthalamic nucleus of patients with Parkinson's disease relates to both bradykinesia and rigidity. Experimental neurology *215*, 380-387.

Kumar, A., Cardanobile, S., Rotter, S., and Aertsen, A. (2011). The role of inhibition in generating and controlling Parkinson's disease oscillations in the basal ganglia. Frontiers in systems neuroscience *5*, 86.

Kunishio, K., and Haber, S.N. (1994). Primate cingulostriatal projection: limbic striatal versus sensorimotor striatal input. Journal of Comparative Neurology *350*, 337-356.

Kupferschmidt, D.A., Juczewski, K., Cui, G., Johnson, K.A., and Lovinger, D.M. (2017). Parallel, but dissociable, processing in discrete corticostriatal inputs encodes skill learning. Neuron *96*, 476-489. e475.

Leblois, A., Meissner, W., Bioulac, B., Gross, C.E., Hansel, D., and Boraud, T. (2007). Late emergence of synchronized oscillatory activity in the pallidum during progressive Parkinsonism. European Journal of Neuroscience *26*, 1701-1713.

Leckman, J.F., Bloch, M.H., Smith, M.E., Larabi, D., and Hampson, M. (2010). Neurobiological substrates of Tourette's disorder. Journal of child and adolescent psychopharmacology *20*, 237-247.

Lee, K.-M., Chang, K.-H., and Roh, J.-K. (1999). Subregions within the supplementary motor area activated at different stages of movement preparation and execution. Neuroimage *9*, 117-123.

Lee, K., Holley, S.M., Shobe, J.L., Chong, N.C., Cepeda, C., Levine, M.S., and Masmanidis, S.C. (2017). Parvalbumin interneurons modulate striatal output and enhance performance during associative learning. Neuron *93*, 1451-1463. e1454.

Leventhal, D.K., Gage, G.J., Schmidt, R., Pettibone, J.R., Case, A.C., and Berke, J.D. (2012). Basal ganglia beta oscillations accompany cue utilization. Neuron *73*, 523-536.

Lévesque, M., Charara, A., Gagnon, S., Parent, A., and Deschênes, M. (1996). Corticostriatal projections from layer V cells in rat are collaterals of long-range corticofugal axons. Brain research *709*, 311-315.

Levy, R., Ashby, P., Hutchison, W.D., Lang, A.E., Lozano, A.M., and Dostrovsky, J.O. (2002). Dependence of subthalamic nucleus oscillations on movement and dopamine in Parkinson's disease. Brain *125*, 1196-1209.

Li, N., Chen, T.-W., Guo, Z.V., Gerfen, C.R., and Svoboda, K. (2015). A motor cortex circuit for motor planning and movement. Nature *519*, 51-56.

Little, S., and Brown, P. (2012). What brain signals are suitable for feedback control of deep brain stimulation in Parkinson's disease? Annals of the New York Academy of Sciences *1265*, 9-24.

Little, S., and Brown, P. (2014). The functional role of beta oscillations in Parkinson's disease. Parkinsonism & related disorders *20*, S44-S48.

Lynd-Balta, E., and Haber, S. (1994). The organization of midbrain projections to the striatum in the primate: sensorimotor-related striatum versus ventral striatum. Neuroscience *59*, 625-640.

Magill, P.J., Bolam, J.P., and Bevan, M.D. (2001). Dopamine regulates the impact of the cerebral cortex on the subthalamic nucleus-globus pallidus network. Neuroscience *106*, 313-330.

Mahon, S., Deniau, J.-M., Charpier, S., and Delord, B. (2000). Role of a striatal slowly inactivating potassium current in short-term facilitation of corticostriatal inputs: a computer simulation study. Learning & Memory *7*, 357-362.

Maia, T.V., Cooney, R.E., and Peterson, B.S. (2008). The neural bases of obsessive–compulsive disorder in children and adults. Development and psychopathology *20*, 1251-1283.

Mallet, N., Ballion, B., Le Moine, C., and Gonon, F. (2006). Cortical inputs and GABA interneurons imbalance projection neurons in the striatum of parkinsonian rats. Journal of Neuroscience *26*, 3875-3884.

Mallet, N., Le Moine, C., Charpier, S., and Gonon, F. (2005). Feedforward inhibition of projection neurons by fast-spiking GABA interneurons in the rat striatum in vivo. The Journal of neuroscience *25*, 3857-3869.

Mallet, N., Micklem, B.R., Henny, P., Brown, M.T., Williams, C., Bolam, J.P., Nakamura, K.C., and Magill, P.J. (2012). Dichotomous organization of the external globus pallidus. Neuron *74*, 1075-1086.

Mallet, N., Pogosyan, A., Márton, L.F., Bolam, J.P., Brown, P., and Magill, P.J. (2008a). Parkinsonian beta oscillations in the external globus pallidus and their relationship with subthalamic nucleus activity. Journal of neuroscience *28*, 14245-14258.

Mallet, N., Pogosyan, A., Sharott, A., Csicsvari, J., Bolam, J.P., Brown, P., and Magill, P.J. (2008b). Disrupted dopamine transmission and the emergence of exaggerated beta oscillations in subthalamic nucleus and cerebral cortex. Journal of Neuroscience *28*, 4795-4806.

Maltby, N., Tolin, D.F., Worhunsky, P., O'keefe, T.M., and Kiehl, K.A. (2005). Dysfunctional action monitoring hyperactivates frontal–striatal circuits in obsessive–compulsive disorder: an event-related fMRI study. Neuroimage *24*, 495-503.

Mantovani, A., Simpson, H.B., Fallon, B.A., Rossi, S., and Lisanby, S.H. (2010). Randomized sham-controlled trial of repetitive transcranial magnetic stimulation in treatment-resistant obsessive–compulsive disorder. International Journal of Neuropsychopharmacology *13*, 217-227.

Marche, K., and Apicella, P. (2016). Changes in activity of fast-spiking interneurons of the monkey striatum during reaching at a visual target. American Journal of Physiology-Heart and Circulatory Physiology.

Markowitz, J.E., Gillis, W.F., Beron, C.C., Neufeld, S.Q., Robertson, K., Bhagat, N.D., Peterson, R.E., Peterson, E., Hyun, M., and Linderman, S.W. (2018). The striatum organizes 3D behavior via moment-to-moment action selection. Cell *174*, 44-58. e17.

Marquand, A.F., Haak, K.V., and Beckmann, C.F. (2017). Functional corticostriatal connection topographies predict goal-directed behaviour in humans. Nature human behaviour *1*, 0146.

Martiros, N., Burgess, A.A., and Graybiel, A.M. (2018). Inversely active striatal projection neurons and interneurons selectively delimit useful behavioral sequences. Current Biology *28*, 560-573. e565.

Mastro, K.J., Bouchard, R.S., Holt, H.A., and Gittis, A.H. (2014). Transgenic mouse lines subdivide external segment of the globus pallidus (GPe) neurons and reveal distinct GPe output pathways. J Neurosci *34*, 2087-2099.

Matamales, M., Bertran-Gonzalez, J., Salomon, L., Degos, B., Deniau, J.-M., Valjent, E., Hervé, D., and Girault, J.-A. (2009). Striatal medium-sized spiny neurons: identification by nuclear staining and study of neuronal subpopulations in BAC transgenic mice. PloS one *4*, e4770.

McCarthy, M., Moore-Kochlacs, C., Gu, X., Boyden, E., Han, X., and Kopell, N. (2011). Striatal origin of the pathologic beta oscillations in Parkinson's disease. Proceedings of the National Academy of Sciences *108*, 11620-11625.

McFarland, N.R., and Haber, S.N. (2000). Convergent inputs from thalamic motor nuclei and frontal cortical areas to the dorsal striatum in the primate. Journal of Neuroscience *20*, 3798-3813.

McGeorge, A., and Faull, R. (1989). The organization of the projection from the cerebral cortex to the striatum in the rat. Neuroscience *29*, 503-537.

Meng, C., Zhou, J., Papaneri, A., Peddada, T., Xu, K., and Cui, G. (2018). Spectrally resolved fiber photometry for multi-component analysis of brain circuits. Neuron *98*, 707-717. e704.

Menzies, L., Chamberlain, S.R., Laird, A.R., Thelen, S.M., Sahakian, B.J., and Bullmore, E.T. (2008). Integrating evidence from neuroimaging and neuropsychological studies of obsessive-compulsive disorder: the orbitofronto-striatal model revisited. Neuroscience & Biobehavioral Reviews *32*, 525-549.

Miguelez, C., Morin, S., Martinez, A., Goillandeau, M., Bezard, E., Bioulac, B., and Baufreton, J. (2012). Altered pallido-pallidal synaptic transmission leads to aberrant firing of globus pallidus neurons in a rat model of Parkinson's disease. The Journal of physiology *590*, 5861-5875.

Mittler, T., Cho, J., People, L., and West, M. (1994). Representation of the body in the lateral striatum of the freely moving rat: single neurons related to licking. Experimental brain research *98*, 163-167.

Montgomery Jr, E.B., and Buchholz, S.R. (1991). The striatum and motor cortex in motor initiation and execution. Brain research *549*, 222-229.

Muthukumaraswamy, S.D. (2010). Functional properties of human primary motor cortex gamma oscillations. Journal of neurophysiology *104*, 2873-2885.

Nachev, P., Kennard, C., and Husain, M. (2008). Functional role of the supplementary and pre-supplementary motor areas. Nature Reviews Neuroscience *9*, 856.

Naito, A., and Kita, H. (1994). The cortico-pallidal projection in the rat: an anterograde tracing study with biotinylated dextran amine. Brain research *653*, 251-257.

Nakamae, T., Sakai, Y., Abe, Y., Nishida, S., Fukui, K., Yamada, K., Kubota, M., Denys, D., and Narumoto, J. (2014). Altered fronto-striatal fiber topography and connectivity in obsessive-compulsive disorder. PloS one *9*, e112075.

Nakayama, Y., Yamagata, T., Tanji, J., and Hoshi, E. (2008). Transformation of a virtual action plan into a motor plan in the premotor cortex. Journal of Neuroscience *28*, 10287-10297.

Neuner, I., Werner, C.J., Arrubla, J., Stöcker, T., Ehlen, C., Wegener, H.P., Schneider, F., and Shah, N.J. (2014). Imaging the where and when of tic generation and resting state networks in adult Tourette patients. Frontiers in human neuroscience *8*, 362.

Nevado-Holgado, A.J., Mallet, N., Magill, P.J., and Bogacz, R. (2014). Effective connectivity of the subthalamic nucleus–globus pallidus network during Parkinsonian oscillations. The Journal of physiology *592*, 1429-1455.

Nini, A., Feingold, A., Slovin, H., and Bergman, H. (1995). Neurons in the globus pallidus do not show correlated activity in the normal monkey, but phase-locked oscillations appear in the MPTP model of parkinsonism. Journal of neurophysiology *74*, 1800-1805.

Nisenbaum, E.S., Wilson, C.J., Foehring, R.C., and Surmeier, D.J. (1996). Isolation and characterization of a persistent potassium current in neostriatal neurons. Journal of neurophysiology *76*, 1180-1194.

O'Hare, J.K., Li, H., Kim, N., Gaidis, E., Ade, K., Beck, J., Yin, H., and Calakos, N. (2017). Striatal fast-spiking interneurons selectively modulate circuit output and are required for habitual behavior. Elife *6*.

Oh, S.W., Harris, J.A., Ng, L., Winslow, B., Cain, N., Mihalas, S., Wang, Q., Lau, C., Kuan, L., and Henry, A.M. (2014). A mesoscale connectome of the mouse brain. Nature *508*, 207-214.

Oorschot, D.E. (1996). Total number of neurons in the neostriatal, pallidal, subthalamic, and substantia nigral nuclei of the rat basal ganglia: a stereological study using the cavalieri and optical disector methods. Journal of Comparative Neurology *366*, 580-599.

Owen, S.F., Berke, J.D., and Kreitzer, A.C. (2018). Fast-spiking interneurons supply feedforward control of bursting, calcium, and plasticity for efficient learning. Cell *172*, 683-695. e615.

Panigrahi, B., Martin, K.A., Li, Y., Graves, A.R., Vollmer, A., Olson, L., Mensh, B.D., Karpova, A.Y., and Dudman, J.T. (2015). Dopamine is required for the neural representation and control of movement vigor. Cell *162*, 1418-1430.

Parker, J.G., Marshall, J.D., Ahanonu, B., Wu, Y.-W., Kim, T.H., Grewe, B.F., Zhang, Y., Li, J.Z., Ding, J.B., and Ehlers, M.D. (2018). Diametric neural ensemble dynamics in parkinsonian and dyskinetic states. Nature *557*, 177.

Parthasarathy, H., and Graybiel, A. (1997). Cortically driven immediate-early gene expression reflects modular influence of sensorimotor cortex on identified striatal neurons in the squirrel monkey. The Journal of neuroscience *17*, 2477-2491.

Pasupathy, A., and Miller, E.K. (2005). Different time courses of learning-related activity in the prefrontal cortex and striatum. Nature *433*, 873.

Pavlides, A., Hogan, S.J., and Bogacz, R. (2015). Computational models describing possible mechanisms for generation of excessive beta oscillations in Parkinson's disease. PLoS computational biology *11*, e1004609.

Pisa, M. (1988). Motor functions of the striatum in the rat: critical role of the lateral region in tongue and forelimb reaching. Neuroscience *24*, 453-463.

Pisansky, M.T., Lefevre, E.M., Retzlaff, C.L., Trieu, B.H., and Rothwell, P.E. (2019). Nucleus Accumbens Fast-Spiking Interneurons Constrain Impulsive Action. bioRxiv, 516609.

Plenz, D., and Kitai, S.T. (1998). Up and down states in striatal medium spiny neurons simultaneously recorded with spontaneous activity in fast-spiking interneurons studied in cortex–striatum–substantia nigra organotypic cultures. Journal of Neuroscience *18*, 266-283.

Plenz, D., and Kital, S.T. (1999). A basal ganglia pacemaker formed by the subthalamic nucleus and external globus pallidus. Nature *400*, 677.

Plotkin, J.L., Day, M., and Surmeier, D.J. (2011). Synaptically driven state transitions in distal dendrites of striatal spiny neurons. Nature neuroscience *14*, 881.

Pogorelov, V., Xu, M., Smith, H.R., Buchanan, G.F., and Pittenger, C. (2015). Corticostriatal interactions in the generation of tic-like behaviors after local striatal disinhibition. Experimental neurology *265*, 122-128.

Ragozzino, M.E. (2007). The contribution of the medial prefrontal cortex, orbitofrontal cortex, and dorsomedial striatum to behavioral flexibility. Annals of the New York academy of sciences *1121*, 355-375.

Rajakumar, N., Elisevich, K., and Flumerfelt, B. (1994). The pallidostriatal projection in the rat: a recurrent inhibitory loop? Brain research *651*, 332-336.

Ramanathan, S., Hanley, J.J., Deniau, J.-M., and Bolam, J.P. (2002). Synaptic convergence of motor and somatosensory cortical afferents onto GABAergic interneurons in the rat striatum. The Journal of neuroscience *22*, 8158-8169.

Rauch, S.L., Jenike, M.A., Alpert, N.M., Baer, L., Breiter, H.C., Savage, C.R., and Fischman, A.J. (1994). Regional cerebral blood flow measured during symptom provocation in obsessive-compulsive disorder using oxygen 15—labeled carbon dioxide and positron emission tomography. Archives of general psychiatry *51*, 62-70.

Rauch, S.L., Savage, C.R., Alpert, N.M., Dougherty, D., Kendrick, A., Curran, T., Brown, H.D., Manzo, P., Fischman, A.J., and Jenike, M.A. (1997). Probing striatal function in obsessive-compulsive disorder: a PET study of implicit sequence learning. Journal of Neuropsychiatry and Clinical Neurosciences *9*, 568-573.

Raz, A., Vaadia, E., and Bergman, H. (2000). Firing patterns and correlations of spontaneous discharge of pallidal neurons in the normal and the tremulous 1-methyl-4-phenyl-1, 2, 3, 6-tetrahydropyridine vervet model of parkinsonism. Journal of Neuroscience *20*, 8559-8571.

Riehle, A., Grün, S., Diesmann, M., and Aertsen, A. (1997). Spike synchronization and rate modulation differentially involved in motor cortical function. Science *278*, 1950-1953.

Rothwell, P.E., Hayton, S.J., Sun, G.L., Fuccillo, M.V., Lim, B.K., and Malenka, R.C. (2015). Input-and output-specific regulation of serial order performance by corticostriatal circuits. Neuron *88*, 345-356.

Rubin, J.E., and Terman, D. (2004). High frequency stimulation of the subthalamic nucleus eliminates pathological thalamic rhythmicity in a computational model. Journal of computational neuroscience *16*, 211-235.

Saka, E., Goodrich, C., Harlan, P., Madras, B.K., and Graybiel, A.M. (2004). Repetitive behaviors in monkeys are linked to specific striatal activation patterns. Journal of Neuroscience *24*, 7557-7565.

Saka, E., and Graybiel, A.M. (2003). Pathophysiology of Tourette's Syndrome: striatal pathways revisited. Brain and Development *25*, 5.

Sarnthein, J., and Jeanmonod, D. (2007). High thalamocortical theta coherence in patients with Parkinson's disease. Journal of Neuroscience *27*, 124-131.

Sato, F., Lavallée, P., Lévesque, M., and Parent, A. (2000). Single-axon tracing study of neurons of the external segment of the globus pallidus in primate. Journal of Comparative Neurology *417*, 17-31.

Saxena, S., Brody, A.L., Schwartz, J.M., and Baxter, L.R. (1998). Neuroimaging and frontal-subcortical circuitry in obsessive-compulsive disorder. The British Journal of Psychiatry.

Schoenbaum, G., Nugent, S.L., Saddoris, M.P., and Setlow, B. (2002). Orbitofrontal lesions in rats impair reversal but not acquisition of go, no-go odor discriminations. Neuroreport *13*, 885-890.

Schultz, W., Apicella, P., Scarnati, E., and Ljungberg, T. (1992). Neuronal activity in monkey ventral striatum related to the expectation of reward. Journal of neuroscience *12*, 4595-4610.

Schultz, W., Dayan, P., and Montague, P.R. (1997). A neural substrate of prediction and reward. Science *275*, 1593-1599.

Selemon, L., and Goldman-Rakic, P. (1985). Longitudinal topography and interdigitation of corticostriatal projections in the rhesus monkey. Journal of Neuroscience *5*, 776-794.

Seo, M., Lee, E., and Averbeck, B.B. (2012). Action selection and action value in frontal-striatal circuits. Neuron *74*, 947-960.

Sharott, A., Magill, P.J., Harnack, D., Kupsch, A., Meissner, W., and Brown, P. (2005). Dopamine depletion increases the power and coherence of β-oscillations in the cerebral cortex and subthalamic nucleus of the awake rat. European Journal of Neuroscience *21*, 1413-1422.

Shima, K., Mushiake, H., Saito, N., and Tanji, J. (1996). Role for cells in the presupplementary motor area in updating motor plans. Proceedings of the National Academy of Sciences *93*, 8694-8698.

Shink, E., and Smith, Y. (1995). Differential synaptic innervation of neurons in the internal and external segments of the globus pallidus by the GABA-and glutamate-containing terminals in the squirrel monkey. Journal of Comparative Neurology *358*, 119-141.

Singer, H.S., Hahn, I.H., and Moran, T.H. (1991). Abnormal dopamine uptake sites in postmortem striatum from patients with Tourette's syndrome. Annals of Neurology: Official Journal of the American Neurological Association and the Child Neurology Society *30*, 558-562.

Smith, K.S., and Graybiel, A.M. (2013). A dual operator view of habitual behavior reflecting cortical and striatal dynamics. Neuron *79*, 361-374.

Smith, Y., and Wichmann, T. (2015). The cortico-pallidal projection: an additional route for cortical regulation of the basal ganglia circuitry. Movement disorders: official journal of the Movement Disorder Society *30*, 293.

Sohal, V.S., Zhang, F., Yizhar, O., and Deisseroth, K. (2009). Parvalbumin neurons and gamma rhythms enhance cortical circuit performance. Nature *459*, 698.

Spooren, W., Lynd-Balta, E., Mitchell, S., and Haber, S. (1996). Ventral pallidostriatal pathway in the monkey: evidence for modulation of basal ganglia circuits. Journal of Comparative Neurology *370*, 295-312.

Staines, W., and Fibiger, H. (1984). Collateral projections of neurons of the rat globus pallidus to the striatum and substantia nigra. Experimental brain research *56*, 217-220.

Staines, W.A., Atmadja, S., and Fibiger, H. (1981). Demonstration of a pallidostriatal pathway by retrograde transport of HRP-labeled lectin. Brain research *206*, 446-450.

Stein, E., and Bar-Gad, I. (2013). Beta oscillations in the cortico-basal ganglia loop during parkinsonism. Experimental Neurology *245*, 52-59.

Stern, E.A., Jaeger, D., and Wilson, C.J. (1998). Membrane potential synchrony of simultaneously recorded striatal spiny neurons in vivo. Nature *394*, 475.

Sul, J.H., Jo, S., Lee, D., and Jung, M.W. (2011). Role of rodent secondary motor cortex in value-based action selection. Nature neuroscience *14*, 1202.

Sul, J.H., Kim, H., Huh, N., Lee, D., and Jung, M.W. (2010). Distinct roles of rodent orbitofrontal and medial prefrontal cortex in decision making. Neuron *66*, 449-460.

Surmeier, D.J., Stefani, A., Foehring, R.C., and Kitai, S. (1991). Developmental regulation of a slowly-inactivating potassium conductance in rat neostriatal neurons. Neuroscience letters *122*, 41-46.

Tachibana, Y., Kita, H., Chiken, S., Takada, M., and Nambu, A. (2008). Motor cortical control of internal pallidal activity through glutamatergic and GABAergic inputs in awake monkeys. Eur J Neurosci *27*, 238-253.

Takahashi, Y.K., Langdon, A.J., Niv, Y., and Schoenbaum, G. (2016). Temporal specificity of reward prediction errors signaled by putative dopamine neurons in rat VTA depends on ventral striatum. Neuron *91*, 182-193.

Takahashi, Y.K., Roesch, M.R., Stalnaker, T.A., Haney, R.Z., Calu, D.J., Taylor, A.R., Burke, K.A., and Schoenbaum, G. (2009). The orbitofrontal cortex and ventral tegmental area are necessary for learning from unexpected outcomes. Neuron *62*, 269-280.

Tanji, J., and Mushiake, H. (1996). Comparison of neuronal activity in the supplementary motor area and primary motor cortex. Cognitive Brain Research *3*, 143-150.

Tanji, J., and Shima, K. (1994). Role for supplementary motor area cells in planning several movements ahead. Nature *371*, 413.

Tass, P., Smirnov, D., Karavaev, A., Barnikol, U., Barnikol, T., Adamchic, I., Hauptmann, C., Pawelcyzk, N., Maarouf, M., and Sturm, V. (2010). The causal relationship between subcortical local field potential oscillations and Parkinsonian resting tremor. Journal of neural Engineering *7*, 016009.

Taverna, S., Ilijic, E., and Surmeier, D.J. (2008). Recurrent collateral connections of striatal medium spiny neurons are disrupted in models of Parkinson's disease. Journal of Neuroscience *28*, 5504-5512.

Tecuapetla, F., Jin, X., Lima, S.Q., and Costa, R.M. (2016). Complementary contributions of striatal projection pathways to action initiation and execution. Cell *166*, 703-715.

Terman, D., Rubin, J.E., Yew, A., and Wilson, C. (2002). Activity patterns in a model for the subthalamopallidal network of the basal ganglia. Journal of Neuroscience *22*, 2963-2976.

Thorn, C.A., Atallah, H., Howe, M., and Graybiel, A.M. (2010). Differential dynamics of activity changes in dorsolateral and dorsomedial striatal loops during learning. Neuron *66*, 781-795.

Tunstall, M.J., Oorschot, D.E., Kean, A., and Wickens, J.R. (2002). Inhibitory interactions between spiny projection neurons in the rat striatum. Journal of neurophysiology *88*, 1263-1269.

Turner, R.S., and Anderson, M.E. (2005). Context-dependent modulation of movement-related discharge in the primate globus pallidus. Journal of Neuroscience *25*, 2965-2976.

Van Der Meer, M.A., and Redish, A.D. (2009). Low and high gamma oscillations in rat ventral striatum have distinct relationships to behavior, reward, and spiking activity on a learned spatial decision task. Frontiers in integrative neuroscience *3*, 9.

van Velzen, L.S., Vriend, C., de Wit, S.J., and van den Heuvel, O.A. (2014). Response inhibition and interference control in obsessive–compulsive spectrum disorders. Frontiers in human neuroscience *8*, 419.

Vitek, J.L., Hashimoto, T., Peoples, J., DeLong, M.R., and Bakay, R.A. (2004). Acute stimulation in the external segment of the globus pallidus improves parkinsonian motor signs. Movement disorders: official journal of the Movement Disorder Society *19*, 907-915.

Vitek, J.L., Zhang, J., Hashimoto, T., Russo, G.S., and Baker, K.B. (2012). External pallidal stimulation improves parkinsonian motor signs and modulates neuronal activity throughout the basal ganglia thalamic network. Experimental neurology *233*, 581-586.

Voorn, P., Vanderschuren, L.J., Groenewegen, H.J., Robbins, T.W., and Pennartz, C.M. (2004). Putting a spin on the dorsal–ventral divide of the striatum. Trends in neurosciences *27*, 468-474.

Walters, J.R., Hu, D., Itoga, C.A., Parr-Brownlie, L.C., and Bergstrom, D.A. (2007). Phase relationships support a role for coordinated activity in the indirect pathway in organizing slow oscillations in basal ganglia output after loss of dopamine. Neuroscience *144*, 762-776.

Wan, Y., Ade, K.K., Caffall, Z., Ozlu, M.I., Eroglu, C., Feng, G., and Calakos, N. (2014). Circuit-selective striatal synaptic dysfunction in the *Sapap3* knockout mouse model of obsessive-compulsive disorder. Biological psychiatry *75*, 623-630.

Wan, Y., Feng, G., and Calakos, N. (2011). *Sapap3* deletion causes mGluR5-dependent silencing of AMPAR synapses. The Journal of Neuroscience *31*, 16685-16691.

Weinberger, M., Hutchison, W.D., and Dostrovsky, J.O. (2009). Pathological subthalamic nucleus oscillations in PD: can they be the cause of bradykinesia and akinesia? Experimental neurology *219*, 58-61.

Weinberger, M., Mahant, N., Hutchison, W.D., Lozano, A.M., Moro, E., Hodaie, M., Lang, A.E., and Dostrovsky, J.O. (2006). Beta oscillatory activity in the subthalamic nucleus and its relation to dopaminergic response in Parkinson's disease. Journal of neurophysiology *96*, 3248-3256.

Welch, J.M., Lu, J., Rodriguiz, R.M., Trotta, N.C., Peca, J., Ding, J.-D., Feliciano, C., Chen, M., Adams, J.P., and Luo, J. (2007). Cortico-striatal synaptic defects and OCD-like behaviours in *Sapap3*-mutant mice. Nature *448*, 894-900.

Whittington, M.A., Traub, R., Kopell, N., Ermentrout, B., and Buhl, E. (2000). Inhibition-based rhythms: experimental and mathematical observations on network dynamics. International journal of psychophysiology *38*, 315-336.

Wiesendanger, E., Clarke, S., Kraftsik, R., and Tardif, E. (2004). Topography of cortico-striatal connections in man: anatomical evidence for parallel organization. European Journal of Neuroscience *20*, 1915-1922.

Wilson, C.J. (2009). What controls the timing of striatal spiny cell action potentials in the up state? In The Basal Ganglia IX (Springer), pp. 49-61.

Wilson, C.J., and Kawaguchi, Y. (1996). The origins of two-state spontaneous membrane potential fluctuations of neostriatal spiny neurons. Journal of neuroscience *16*, 2397-2410.

Wood, J., Simon, N.W., Koerner, F.S., Kass, R.E., and Moghaddam, B. (2017). Networks of VTA neurons encode real-time information about uncertain numbers of actions executed to earn a reward. Frontiers in behavioral neuroscience *11*, 140.

Worbe, Y., Malherbe, C., Hartmann, A., Pélégrini-Issac, M., Messé, A., Vidailhet, M., Lehéricy, S., and Benali, H. (2012). Functional immaturity of cortico-basal ganglia networks in Gilles de la Tourette syndrome. Brain *135*, 1937-1946.

Xu, M., Li, L., and Pittenger, C. (2016). Ablation of fast-spiking interneurons in the dorsal striatum, recapitulating abnormalities seen post-mortem in Tourette syndrome, produces anxiety and elevated grooming. Neuroscience *324*, 321-329.

Xu, Z., Chen, R.-Q., Gu, Q.-H., Yan, J.-Z., Wang, S.-H., Liu, S.-Y., and Lu, W. (2009). Metaplastic regulation of long-term potentiation/long-term depression threshold by activity-dependent changes of NR2A/NR2B ratio. Journal of Neuroscience *29*, 8764-8773.

Yin, H.H., Knowlton, B.J., and Balleine, B.W. (2004). Lesions of dorsolateral striatum preserve outcome expectancy but disrupt habit formation in instrumental learning. European journal of neuroscience *19*, 181-189.

Yin, H.H., Knowlton, B.J., and Balleine, B.W. (2006). Inactivation of dorsolateral striatum enhances sensitivity to changes in the action–outcome contingency in instrumental conditioning. Behavioural brain research *166*, 189-196.

Yin, H.H., Mulcare, S.P., Hilário, M.R., Clouse, E., Holloway, T., Davis, M.I., Hansson, A.C., Lovinger, D.M., and Costa, R.M. (2009). Dynamic reorganization of striatal circuits during the acquisition and consolidation of a skill. Nature neuroscience *12*, 333-341.

Yin, H.H., Ostlund, S.B., Knowlton, B.J., and Balleine, B.W. (2005). The role of the dorsomedial striatum in instrumental conditioning. European Journal of Neuroscience *22*, 513-523.

Yttri, E.A., and Dudman, J.T. (2016). Opponent and bidirectional control of movement velocity in the basal ganglia. Nature *533*, 402.

Yücel, M., Harrison, B.J., Wood, S.J., Fornito, A., Wellard, R.M., Pujol, J., Clarke, K., Phillips, M.L., Kyrios, M., and Velakoulis, D. (2007). Functional and biochemical alterations of the medial frontal cortex in obsessive-compulsive disorder. Archives of General Psychiatry *64*, 946-955.

Züchner, S., Wendland, J., Ashley-Koch, A., Collins, A., Tran-Viet, K., Quinn, K., Timpano, K., Cuccaro, M., Pericak-Vance, M.A., and Steffens, D. (2009). Multiple rare *SAPAP3* missense variants in trichotillomania and OCD. Molecular psychiatry *14*, 6.